Cryogen Free Measurement System (12 18 Tesla)

Papers

Bulk Superconductivity in Bismuth oxy-sulfide $Bi_4O_4S_3$

Giant Magnetoelastic Coupling in a Metallic Helical Metamagnet

Thermomagnetic irreversibility in $Ni_2Mn_{1.36}Sn_{0.64}$ shape-memory alloy

Influence of the strong magnetocrystalline anisotropy on the magnetocaloric properties of MnP single crystal

Metastability and magnetic memory effect in $Ni_2Mn_{1.4}Sn_{0.6}$

High-field magnetic phase transitions and spin excitations in magnetoelectric $LiNiPO_4$

Bulk Superconductivity in Bismuth oxy-sulfide $Bi_4O_4S_3$

Shiva Kumar Singh[#], Anuj Kumar[#], Bhasker Gahtori[#], Shruti[$], G. Sharma[$], S. Patnaik[$] and V.P.S. Awana[#,*]

[#]*Quantum Phenomena and Applications Division, National Physical Laboratory (CSIR) Dr. K. S. Krishnan Road, New Delhi-110012, India*

[$]*School of Physical Sciences, Jawaharlal Nehru University, New Delhi-110067, India*

Supporting Information Placeholder

ABSTRACT: Very recent report[1] on observation of superconductivity in $Bi_4O_4S_3$ could potentially reignite the search for superconductivity in a broad range of layered sulfides. We report here synthesis of $Bi_4O_4S_3$ at 500^0C by vacuum encapsulation technique and basic characterizations. $Bi_4O_4S_3$ is contaminated by small amounts of Bi_2S_3 and Bi impurities. The majority phase is tetragonal *I4/mmm* space group with lattice parameters a = 3.9697(2)Å, c = 41.3520(1)Å. Both *AC* and *DC* magnetization measurements confirmed that $Bi_4O_4S_3$ is a bulk superconductor with superconducting transition temperature (T_c) of 4.4K. Isothermal magnetization (*MH*) measurements indicated closed loops with clear signatures of flux pinning and irreversible behavior. The lower critical field (H_{c1}) at 2K, of the new superconductor is found to be ~15 Oe. The magneto-transport $R(T, H)$ measurements showed a resistive broadening and decrease in T_c (R=0) to lower temperatures with increasing magnetic field. The extrapolated upper critical field $H_{c2}(0)$ is ~ 31kOe with a corresponding Ginzburg-Landau coherence length of ~100Å . In the normal state the $\rho \sim T^2$ is not indicated. Hall resistivity data are suggestive of multiband electronic transport. Our magnetization and electrical transport measurements substantiate the appearance of bulk superconductivity in as synthesized $Bi_4O_4S_3$. On the other hand same temperature heat treated Bi is not superconducting, thus excluding possibility of impurity driven superconductivity in the newly discovered $Bi_4O_4S_3$ superconductor.

The discovery of superconductivity at 26K in $LaO_{1-x}F_xFeAs$[2] ignited a gold rush for search of new superconductors. Besides popular Fe based pnictides[2,3] and chalcogenides[4], some splinter new interesting systems have also appeared. To name some, they are $CeNi_{0.8}Bi_2$[5], BiOCuS[6] and doped $LaCo_2B_2$[7] with their superconducting transition temperature at around 4K. These compounds are layered with relatively large unit cells and mimic the superconducting characteristics of CuO_2 based HTSc cuprates and FeAs based pnictides. The comprehensive theoretical understanding of the mechanisms of CuO_2 and FeAs based high temperature superconductivity is still awaited. The hybridization of Cu-O and Fe-As in these strongly correlated systems along with their multiband character has been of prime interest to the scientific community[8,9]. After the recent observations of superconductivity in BiOCuS[6] and doped $LaCo_2B_2$[7], it is a pertinent question to ask if CuS and CoB could also play the same role as of CuO_2 and FeAs. In this regards, it is worth mentioning that although superconductivity of BiOCuS could not be reproduced[10], the $CeNi_{0.8}Bi_2$ and doped $LaCo_2B_2$ still lack independent confirmation. For example the volume fraction of superconductivity in $CeNi_{0.8}Bi_2$ is very small[11]. In this sense, the observation of superconductivity at around 4K in $Bi_4O_4S_3$[1] has once again started the debate; whether this newest series of superconductivity is intrinsic or not. It is suggested that superconductivity of $Bi_4O_4S_3$ is BiS_2 based and doping mechanism is similar to that of cuprates and pnictides[12,13]. Thus the central question is whether the observed superconductivity in $Bi_4O_4S_3$ is intrinsic or it is being triggered by Bi impurity in the matrix.

Bismuth has been a part of various superconducting compounds, such as Bi based High Temperature cuprates (BSSCO)[14], Bi_3Ni[15,16] and $CeNi_{0.8}Bi_2$[5] compounds. On the other hand, pure Bismuth is found in several phases, out of which ordinary rhombohedral Bi phase is non-superconducting[17,18], while some other phases are found to be superconducting[19-23]. Various crystallographic phases of pure Bi, which are superconducting in the bulk phase, are Bi II, III and V (high-pressure phases of Bi) with T_c = 3.9K, 7.2K, and 8.5 K[19-21] respectively. The *fcc* Bi phase superconducts with $T_c \sim 4$K[22]; and amorphous Bi with $T_c = 6$K[23].

In current communication, we report the extensive characterization of the newly discovered[1] $Bi_4O_4S_3$ superconductor. The synthesized $Bi_4O_4S_3$ is crystallized in tetragonal structure with space group *I*4/*mmm*. The main phase of the sample is contaminated with small impurities of Bi and Bi_2S_3. $Bi_4O_4S_3$ compound is found to be bulk superconducting at around 4.4K, both from magnetization and transport measurements. Interestingly same route heat treated pure Bi is non-superconducting. Bi is in rhombohedral phase and hence is non-superconducting. Our results conclude that superconductivity of $Bi_4O_4S_3$ is intrinsic and not driven by Bi impurity phase.

$Bi_4O_4S_3$ was synthesized by solid state reaction route via vacuum encapsulation. High purity Bi, Bi_2O_3 and S were weighed in right stoichiometric ratio and ground thoroughly in the glove box under high purity argon atmosphere. The powders were subsequently palletized and vacuum-sealed (10^{-4} Torr) in separate quartz tubes. Sealed quartz ampoules were placed in box furnace and heat treated at 500^0C for 18h followed by cooling to room temperature naturally. The process was repeated twice. The *X*-ray diffraction (*XRD*) patterns of the compounds were recorded on Rigaku diffractometer. Rietveld refinement of *XRD* pattern is carried out through *FullProf*. The magnetization and transport measurements were carried out using 14 Tesla *Cryogenic PPMS* (Physical Property Measurement System).

The synthesized $Bi_4O_4S_3$ sample is gray in color. On the other hand, Bi sample is of shiny silver color. The room temperature *X*-ray diffraction (*XRD*) pattern for synthesized Bi and $Bi_4O_4S_3$ samples are shown in Figure l.

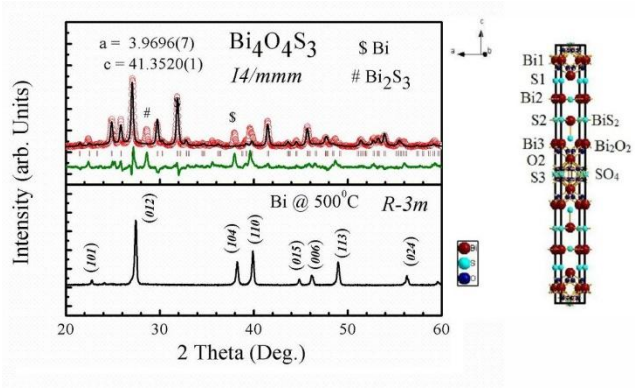

Figure 1. Rietveld refined Room temperature *X*-ray diffraction (*XRD*) patterns of $Bi_4O_4S_3$ and heat treated Bi, the unit cell of the compound is shown along side. .

The $Bi_4O_4S_3$ sample is crystallized in tetragonal structure with space group *I*4/*mmm*. Rietveld refinement of *XRD* patterns are carried out using reported[1] Wyckoff positions. The positions and lattice parameters are further refined and the lattice parameters are a = 3.9697(2)Å, c = 41.3520(1)Å. The Wyckoff positions of the synthesized $Bi_4O_4S_3$ compound are given in table 1. The *XRD* of Bi heat treated at same temperature is also depicted in Figure 1, which is crystallized in clean rhombohedral phase. It can be concluded from *XRD* results that the synthesized $Bi_4O_4S_3$ sample is nearly single phase with some impurities of rhombohedral Bi. Rhombohederal Bi is reported non superconducting[17,18]. However, the structure of the compound is still under debate with the space group of *I*4/*mmm* or *I* -42*m*[1]. The representative unit cell of the compound in *I*4/*mmm* space group crystallization is shown along side in Figure 1. The layered structure includes Bi_2S_4 (rock-salt type), Bi_2O_2 (fluorite type) and SO_4 layers. Superconductivity is induced in BiS_2 layer due to Bi-6*p* and S-3*p* orbitals hybridization. The theoretical calculations[13] show that, bands are derived from Bi-6*p* and in-plane S-3*p* orbitals. These are dominating bands for electron conduction and superconductivity.

Various atoms with their respective positions are cited in the figure. Bismuth (Bi1, Bi2 and Bi3) and Sulfur (S1 and S2) atoms occupied the *4e* (0, 0, *z*) site. S3 atom is at *2b* (0, 0, ½) site. O1 is situated at *8g* (0, ½, *z*) and the O2 atom positioned at *16n* (0, *y*, *z*) site. The structural refinement indicates that the molecular composition is $Bi_3O_3S_{2.25}$. It is the normalization of $Bi_4O_4S_3$ composition by ¾. The superconducting phase is SO_4 deficient phase of $Bi_3O_4S_{2.5}$ ($Bi_6O_8S_5$) phase[1].

DC magnetic susceptibility of $Bi_4O_4S_3$ sample is shown Figure 2. The magnetization is done in both *FC* (Field cooled) and *ZFC* (Zero-field-cooled) protocol under applied magnetic field of 20Oe. The compound shows sharp superconducting onset from 4.4K. This is clear from the zoomed inset of Figure 2. There is evidence for substantial flux trapping too. The bifurcation of *FC* and *ZFC* below T_c marks the irreversible region. Also the shielding fraction as evidenced from *ZFC* diamagnetic susceptibility is quite appreciable. Both *FC* and *ZFC* magnetization data confirm the appearance of bulk superconductivity in $Bi_4O_4S_3$. In order to exclude the role of Bi impurity in superconductivity of $Bi_4O_4S_3$, we also measured the magnetization of same temperature (500^{0}C) heat treated Bi and found the same to be non superconducting (plot not shown). As shown in Figure 1, the 500^{0}C heat treated Bi is crystallized in rhombohedral phase, which is reported to be non-superconducting[17,18]. This excludes the possibility of unreacted Bi driven superconductivity in $Bi_4O_4S_3$. In fact the sufficient superconducting volume fraction and large shielding of our studied sample, itself discards the possibility of the minor impurity phase driven superconductivity.

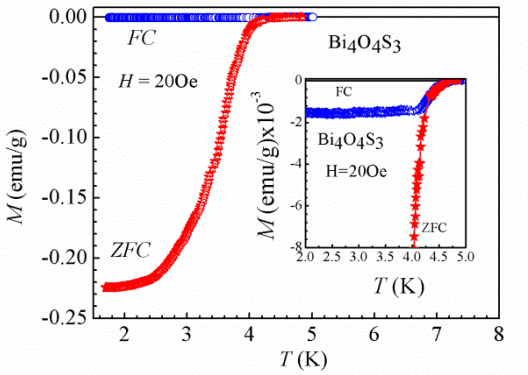

Figure 2. Temperature variation of D*C* Magnetization in *ZFC* and *FC* mode for $Bi_4O_4S_3$ compound at 20Oe. Onset T_c is identified at 4.4K. Inset shows the expanded part of the same plot indicating irreversible behavior.

AC susceptibility versus temperature $\chi(T)$ behavior of the $Bi_4O_4S_3$ sample is exhibited in Figure 3 (a). *AC* susceptibility is done at 1kHz and 10Oe *AC* drive field. *DC* applied field is kept zero to check the superconducting transition temperature and is increased to 5kOe and 10kOe to further check the *AC* loses in the mixed state. Both the real (χ') and imaginary (χ'') part of AC susceptibility were measured. Real part (χ') susceptibility shows sharp transition to diamagnetism at around 4.4K, confirming bulk superconductivity. The imaginary part on the other hand exhibits a single sharp peak in positive susceptibility at around the same temperature. Presence of single sharp peak in χ'' is reminiscent of better superconducting grains coupling in studied $Bi_4O_4S_3$ superconductor. Under applied *DC* field of 5kOe the χ' diamagnetic transition is shifted to lower temperature of 2.6K and the corresponding χ'' peak is broadened and also shifted to same lower temperature. This is usual for a type-II superconductor. At 10kOe *DC* field neither χ' nor χ'' show any transitions, indicative of rapid suppression of superconductivity.

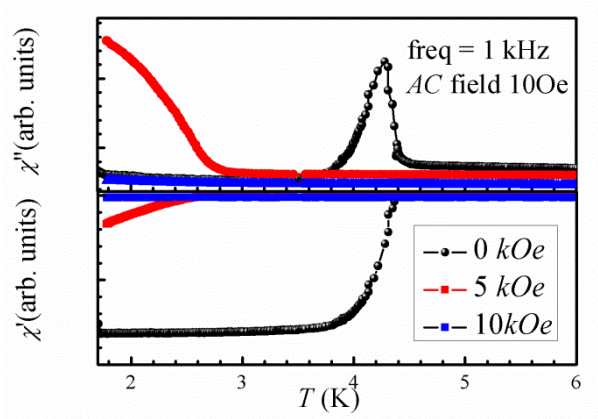

Figure 3. *AC* susceptibility $\chi(T)$ behavior of the $Bi_4O_4S_3$ sample at frequency 1 kHz and *AC* drive amplitude 10Oe under various (0, 5, 10kOe) *DC* applied fields.

Figure 4 shows the isothermal *MH* curve of the sample at 2K up in an applied field of 3kOe. Upper inset of the figure shows the same up to 1kOe. The *MH* curve (lower inset) shows that the ini-

tial flux penetration and the deviation from linearity marks lower critical field (H_{c1}) of this compound ~15 Oe (at 2K). Wide open *MH* loop of the studied $Bi_4O_4S_3$ compound demonstrates bulk superconductivity.

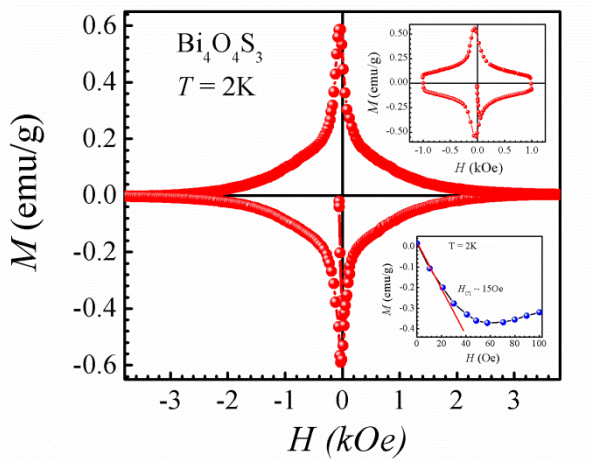

Figure 4. Isothermal magnetization with field (*MH*) at 2K in an applied field up to 3kOe. Insets of the figure show the same in smaller field ranges. H_{c1} (2K) is estimated to be 15Oe.

Figure 5 depicts the resistivity versus temperature (ρ-T) measurement with and without applied magnetic field. The resistance of the sample decreases with temperature and confirms superconductivity with onset T_c ~4.4 K. The normal state conduction is of metallic type and a T^2 fitting is found to be inappropriate implying non-Fermi liquid behavior. With applied field of 1, 2 and 5kOe, the T_c (ρ = 0) decreases to 3.2, 2.7 and 2K. With further higher fields of 10 and 20kOe, the T_c (ρ = 0) state is not observed and only T_c (onset) is seen. As sketched in Figure 5, we have estimated upper critical field H_{c2} (T) by using the conservative procedure of intersection point between linear slope lines of normal state resistivity and superconducting transition line. While the applicability of *WHH* (Werthamer-Helfand-Hohenberg) approximation can be debated in this new superconductor, a simplistic single band extrapolation leads to $H_{c2}(0)$ (= - 0.69 T_c $dH_{c2}/dT|_{Tc}$) value of 31kOe. From this the Ginzburg-Landau coherence length ξ (= $(2.07\text{x}10^{-7}/2\,\pi\,H_{c2})^{1/2}$) is estimated to be ~100 Å.

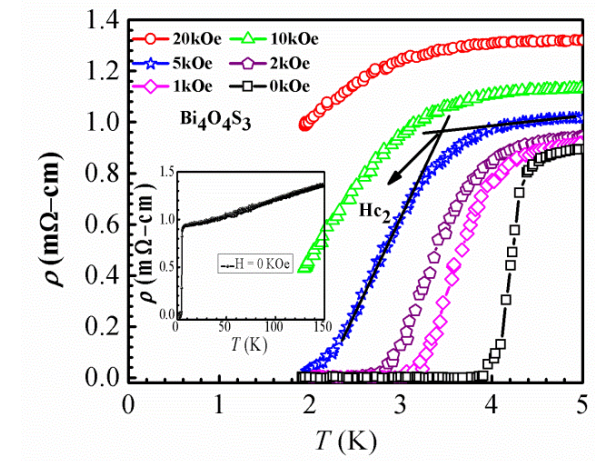

Figure 5. Resistivity vs. temperature (ρ-T) behavior of $Bi_4O_4S_3$ in various applied fields of 0, 1, 2, 5, 10 and 20kOe in superconducting region; inset shows the zero field ρ-T in extended temperature range of 2-150K.

A strong magneto-resistance in the normal state is also seen that can possibly be ascribed to reasons similar to extra Mg impurity in MgB_2 i.e. due to Bi impurity in the matrix or due to multi-band nature of this superconductor. It is predicted by the theoretical calculations that superconductivity in BiS_2 layers is of multi-band type[13]. In Figure 6 we plot the Hall resistivity as a function of magnetic field at 10K. The dominance of electronic charge carrier in normal state conduction mechanism is confirmed. Strong non-linearity is observed with increasing magnetic field that is suggestive of the relevance of multiband analysis.

The Hall coefficient [Figure 6 Inset (a)] is field dependent and the carrier concentration at low field is estimated to be ~1.53×10^{19} per cm^3 at 10K that increases to ~2.4×10^{19} per cm^3 at 300K. An appreciable magneto-resistance in the normal state is also seen. This can simply can be ascribed to Bi impurity in the matrix. But more exotic theories based on multi-band features can also be invoked[24].

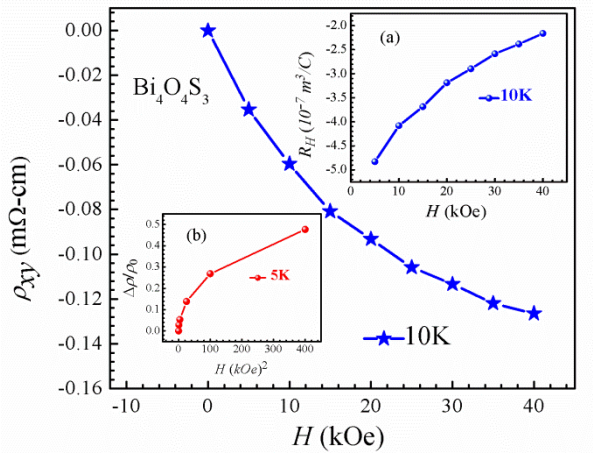

Figure 6. Hall resistivity is plotted as a function of magnetic field at T = 10K. Inset (a) shows variation of Hall coefficient as a function of field. Inset (b) shows normalized magneto-resistance at 5K, implying non- H^2 dependence.

In the inset (b) of Figure 6, we show $\Delta\rho\,(H)/\rho(0)$ versus H^2 at 5K for fields up to 20kOe. One of the established features of multiband superconductivity is the dependence $\Delta\rho\,(H) \propto H^2$ in low field range. Evidently, in this regime, this dependence is not seen. Taken in totality, we can conclude that while our Hall resistivity data demand incorporation of multiband analysis, the magneto-resistance aspects in $Bi_4O_4S_3$ could be due to Bi impurity.

In conclusion we have synthesized the new layered sulfide $Bi_4O_4S_3$ superconductor and established its bulk superconductivity by magnetization and transport measurements. Detailed Reitveld analysis determines the molecular composition as $Bi_3O_3S_{2.25}$. The coherence length is estimated to be ~100Å. A departure from strong electron-electron correlation in the normal state is indicated. The Hall resistivity yields non-linear magnetic field dependence that is suggestive of multiband superconductivity.

AUTHOR INFORMATION

*Corresponding Author

Dr. V. P. S. Awana, Senior Scientist
E-mail: awana@mail.npindia.org
Ph. +91-11-45609357, Fax-+91-11-45609310
Homepage www.fteewebs.com/vpsawana/

Author Contributions

Shiva Kumar, Anuj Kumar and V.P.S. Awana synthesized the compound, Bhasker Gahtori helped in structural analysis, Shruti,

G. Sharma and S. Patnaik performed various physical property measurements. V.P.S. Awana and S. Patnaik prepared the manuscript with help of all authors. V.P.S. Awana planned and executed the present work as a whole with help of all the co-authors.

ACKNOWLEDGMENT

Authors from NPL would like to thank their Director Prof. R.C. Budhani for his keen interest in the present work. Shiva Kumar and Anuj Kumar are thankful to CSIR-India for providing the financial support during their research. Shruti and G. Sharma acknowledge UGC for research fellowships. S. Patnaik thanks AIRF, JNU for the PPMS facility.

REFERENCES

1. Mizuguchi, Y.; Fujihisa, H; Gotoh, Y.; Suzuki, K.; Usui, H.; Kuroki, K.; Demura, S.; Takano, Y.; Izawa, H.; Miura, O. arXiv:1207.3145.
2. Kamihara, Y.; Watanabe, T.; Hirano M.; Hosono, H. J. Am. Chem. Soc. **2008** *130* 3296.
3. Ren, Z. A.; Lu, W.; Yang, J.; Yi, W.; Shen, X. L.; Li, Z. C.; Che, G. C.; Dong, X. L.; Sun, L. L.; Zhou F.; Zhao, Z. X. Chin. Phys. Lett. **2008** *25* 2215.
4. Hsu, F. C.; Luo, J. Y.; Yeh, K. W.; Chen, T. K.; Huang, T. W.; Wu, P. M.; Lee, Y. C.; Huang, Y. L.; Chu, Y. Y.; Yan D. C.; Wu, M. K. Proc. Natl. Acad. Sci. U.S.A. **2008** *105* 14262.
5. Mizuguchi, H.; Matsuishi, S.; Hirano, M.; Tachibana, M.; -Muromachi, E. T.; Kawaji H.; Hosono, H. Phys. Rev. Lett. **2011** *106* 057002.
6. Ubaldini, A.; Giannini, E.; Senatore, C.; van de Marel, D. Physica C **2010** *470* S356.
7. Mizuguchi, H.; Kuroda, T.; Kamiya, T.; Hosono, H. Phys. Rev. Lett. **2011** *106* 0277001.
8. Pickett, W. E. Rev. Mod. Phys **1989** *61* 433.
9. Mazin I. I.; Singh, D. J.; Johannes M. D.; Du, M. H. Phys. Rev. Lett. **2008** *101* 057003.
10. Pal, A.; Kishan, H.; Awana, V. P. S. J. Supercond. & Novel Magn. **2010** *23* 301.
11. Kumar, A.; Kumar, S.; Jha, R.; Awana, V. P. S. J. Supercond. & Novel Magn. **2012** *25* 723.
12. Mizuguchi, Y.; Demura, S.; Deguchi, K.; Takano, Yoshihiko.; Fujihisa, H.; Gotoh, Y.; Izawa, H.; Miura, O. arXiv:1207.3558.
13. Usui, H.; Suzuki, K.; Kuroki, K. arXiv:1207.3888.
14. Maeda, H.; Tanaka, Y.; Fukutumi, M.; Asano T. Jpn. J. Appl. Phys. **1988** *27* L209.
15. Alekseevskii, N. E.; Brandt N. B.; Kostina, T. I. J. Exp. Theor. Phys. **1951** *21* 951.
16. Kumar, J.; Kumar, A.; Vajpayee, A.; Gahtori, B.; Sharma, D.; Ahluwalia, P. K.; Auluck, S.; Awana, V. P. S. Sup. Sci. and Tech. **2011** *24* 085002.
17. Muntyanu, F. M.; Gilewski, A.; Nenkov, K.; Warchulska, J.; Zaleski, A. J. Phys. Rev. B **2006** *73* 132507.
18. Wetzel B.; Micklitz H., Phys. Rev. Lett. **1991** *66* 385.
19. Chester P. F.; Jones, G. O. Philos. Mag. **1953** *44* 1281.
20. Brandt N. B.; Ginzburg, N. J.; Zh. Eksp. Teor. Fiz. **1961** *39* 1554.
21. Wittig, J. Z. Phys. **1966** *195* 228.
22. Moodera, J. S.; Meservey, R. Phys. Rev. B **1990** *42* 179.
23. Buckel W.; Hilsch, R. Z. Phys. **1954** *138* 109.
24. Yang S. L.; Tao J.; Ding X.; Wen H. H. arXiv:1207.4955

.

Table 1. Reitveld refined Wyckoff positions and fractional occupancies of the atoms in $Bi_4O_4S_3$

Atom	*x*	*y*	*z*	*site*	*Fractional occupancy*
Bi1	*0.0000*	*0.0000*	*0.0583 (4)*	*4e*	*1*
Bi2	*0.0000*	*0.0000*	*0.2074 (2)*	*4e*	*1*
Bi3	*0.0000*	*0.0000*	*0.3821 (2)*	*4e*	*1*
S1	*0.0000*	*0.0000*	*0.1383 (1)*	*4e*	*1*
S2	*0.0000*	*0.0000*	*0.2890(1)*	*4e*	*1*
S3	*0.0000*	*0.0000*	*0.5000*	*2b*	*1/2*
O1	*0.0000*	*0.5000*	*0.0884(1)*	*8g*	*1*
O1	*0.0000*	*0.3053(1)*	*0.4793(2)*	*16n*	*1/4*

Giant Magnetoelastic Coupling in a Metallic Helical Metamagnet

A. Barcza,[1] Z. Gercsi,[1,2] K. S. Knight,[3] and K. G. Sandeman[2]

[1]*Department of Materials Science and Metallurgy, University of Cambridge, New Museums Site, Pembroke Street, Cambridge, CB2 3QZ, United Kingdom*

[2]*Department of Physics, Blackett Laboratory, Imperial College London, London SW7 2AZ, United Kingdom*

[3]*ISIS, Rutherford Appleton Laboratory, Oxon OX11 0QX, United Kingdom*

(Received 5 March 2010; published 14 June 2010)

Using high resolution neutron diffraction and capacitance dilatometry we show that the thermal evolution of the helimagnetic state in CoMnSi is accompanied by a change in interatomic distances of up to 2%, the largest ever found in a metallic magnet. Our results and the picture of competing exchange and strongly anisotropic thermal expansion that we use to understand them sheds light on a new mechanism for large magnetoelastic effects that does not require large spin-orbit coupling.

DOI: 10.1103/PhysRevLett.104.247202 PACS numbers: 75.80.+q, 46.25.Hf, 61.05.fm, 65.40.De

Most materials change shape in a magnetic field. Usually the effect, and the so-called magnetoelastic interaction from which it derives are small, especially away from a phase transition. However, large magnetoelastic interactions are crucial to a range of new, technological materials in which multiple order parameters exist simultaneously and are coupled. These include ferromagnetic shape memory materials [1], multiferroics [2], and magnetic refrigerant materials [3]. Despite their relevance, atomically resolved observations of large magnetoelastic effects within a given crystal structure are very rare.

Giant magnetoelastic coupling was recently observed in multiferroic hexagonal manganites [2], where it is 2 orders of magnitude larger than in any other magnetic material. In those compounds it is believed to be central to magnetoelectric coupling and multiferroicity and is thought to arise, unusually, from strongly varying exchange interactions where the coordination of Mn atoms in MnO_5 trigonal bipyramids removes the orbital degeneracy and Jahn-Teller mechanism typically found in MnO_6-derived structures. Here we show that exchange-derived giant magnetoelastic interactions are not limited to multiferroic oxides, but may be much more general, if one examines materials that possess competing exchange interactions relieved by temperature or applied field. The system we study is CoMnSi, a metallic antiferromagnet.

We previously observed a large magnetocaloric effect (MCE) in CoMnSi, a metamagnet that has a field- and temperature-induced transition from a low temperature, noncollinear incommensurate helical antiferromagnetic (AFM) state to a high magnetization state [4]. CoMnSi is structurally similar to MnP, a system in which the field dependence of noncollinear magnetic states has been well studied [5] and in which a rare Lifshitz tricritical point is seen [6]. However, the similarity of the magnetic structures in MnP and in CoMnSi is not so well known, due to a lack of single crystals and of temperature-dependent neutron diffraction data. Here we focus on the isostructural evolution of the crystal lattice within the helical ground state of CoMnSi. We show that, within the AFM state and well below the zero-field Néel temperature there is a giant, and opposing, change in the two shortest Mn-Mn distances, of around 2%. This change has two consequences. First, it brings about an Invar-like effect in sample volume in zero magnetic field. Second, it couples strongly to the suppression of helimagnetism in finite magnetic fields and brings about a tricritical point, with enhanced magnetocaloric and magnetostrictive effects.

The samples that we study here were formed by comelting appropriate amounts of high purity elements under argon in an induction furnace, followed by postannealing and slow cooling. Details are given elsewhere [4]. Magnetic measurements in fields of up to 9 Tesla were performed on polycrystalline samples with a Cryogenic Ltd. vibrating sample magnetometer (VSM). Structural characterization was carried out in up to three ways. First, we conducted a Rietveld refinement of data from room temperature x-ray diffraction using Cu-$K\alpha$ radiation. Second, thermal expansion and magnetostriction were measured with a miniature capacitance dilatometer [7] using polycrystalline pieces cut to have at least one flat face. The Cryogenic Ltd. superconducting magnet and cryostat were used in this experiment. Third, on two samples neutron diffraction was carried out at the time-of-flight high resolution powder diffractometer (HRPD) at ISIS, U.K. This instrument has a resolution of $\Delta d/d \sim 1 \times 10^{-4}$ and was used at temperatures between 4.2 and 500 K. X-ray diffraction at room temperature showed that all samples were single phase to within experimental resolution. Structural refinements of these data agreed well with neutron diffraction data results close to room temperature. We therefore only discuss unit cell refinements where obtained by high resolution neutron diffraction.

In Fig. 1 we show a measure of the zero-field thermal expansion of the two samples involved in this study, CoMnSi and $Co_{0.95}Ni_{0.05}MnSi$, obtained using the HRPD neutron diffractometer. For CoMnSi, the sample was cooled down to 4.2 K and diffraction patterns were col-

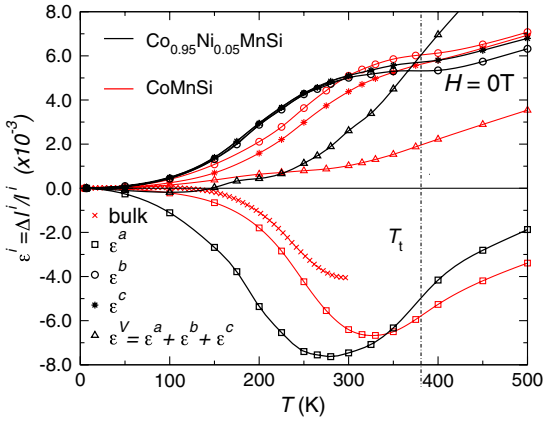

FIG. 1 (color online). Thermal expansion ϵ^i of CoMnSi and $Co_{0.95}Ni_{0.05}MnSi$ along each crystal axis measured on powders using HRPD. Lines are a guide to the eye. The largest change in cell parameters, including an a axis NTE, occurs well below the metamagnetic transition temperature T_t. Bulk thermal expansion of $Co_{0.95}Ni_{0.05}MnSi$ measured using a dilatometer indicates that our as-prepared ingots are textured along the a axis.

lected at 4.2 K, 50 K and then at 50 K intervals up to 500 K. Then the sample was cooled down to 225 K and additional patterns were collected at 225, 275, 315, 330, and 375 K, resulting in 15 diffraction patterns. At each step the temperature was equilibrated for 20 min and a total neutron current of 75 μA was collected for each frame. Neutron diffraction by $Co_{0.95}Ni_{0.05}MnSi$ was conducted as follows: at 4.2 K, 100 K and then each 50 K up to 300 K with a total neutron current of 75 μA and in a second experiment at other temperatures up to 500 K with 60 μA total neutron current. We used the GSAS code [8] to perform a Rietveld refinement of the crystal structure. From the resulting lattice parameters thermal expansion ϵ^i, defined as $[l(T) - l(T_0)/l(T_0)]$ was calculated, with $l(T)$ being one lattice parameter at temperature T and $T_0 = 5$ K.

The Néel transition in zero magnetic field is second order, as evidenced by a broad peak in heat capacity measurements occurs at $T_t \sim 380$ K [4]. For CoMnSi we see that below T_t there is a clear change in thermal expansion, with the most distinctive feature being a large negative thermal expansion (NTE) along the a direction, as seen from the negative values of $\epsilon^a(T)$. This NTE occurs between 4.2 and around 330 K and amounts to a shrinkage of the a axis of almost 0.7%. Weaker features of opposite sign were detected in the same temperature range along the b and c axis yielding anisotropic, positive thermal expansion of enhanced magnitude compared to a phonon-governed process. It should be noted that the crystal symmetry does not change over the whole measured temperature range. The volume thermal expansion of a polycrystal can be estimated by $\epsilon^a + \epsilon^b + \epsilon^c$ and is also indicated in Fig. 1. At around 250 K compensation of negative and positive thermal expansion leads to near-Invar-like temperature-independent behavior of the calculated volume expansion. Above T_t the expansion of CoMnSi is more Debye-like.

The second alloy that we examined with the HRPD, $Co_{0.95}Ni_{0.05}MnSi$, also had a zero-field $T_t \sim 380$ K and showed anisotropic thermal expansion similar to that of CoMnSi, but with the main features shifted to lower temperatures by about 70 K. We may therefore infer some robustness to the anisotropic thermal expansion and a-axis NTE of CoMnSi-based helimagnets.

We may also use the neutron diffraction data to track the temperature dependence of all interatomic separations. The separation of localized Mn moments and the amount of intrinsic strain is believed to be very important to the observed magnetic properties of CoMnSi-based systems: for CoMnSi either a Néel transition or (in quenched materials) a spontaneous transition to a high magnetization state has previously been observed, with zero-field literature transition values varying by up to 200 K. We previously demonstrated a correlation between these values of T_t and the value of the a parameter found at 4.2 K, indicating the presence of a critical a parameter for metamagnetism [4]. In this Letter we are able to demonstrate that the origin of such sensitive metamagnetism is in fact a giant magnetoelastic coupling, the largest yet seen in a metallic magnet. In CoMnSi-based metamagnets, Mn carries the majority of the magnetic moment [9] and plays the most important role in determining magnetic properties. In both CoMnSi and $Co_{0.95}Ni_{0.05}MnSi$ we observe a crossover of the two nearest-neighbor Mn-Mn separations, labeled d_1 and d_2 [see Fig. 2(c)] which occur in the same temperature range as the pronounced a direction NTE, well below T_t. Both separations change, in opposite senses, by between 1% and 2%. We may reasonably assume that such a drastic change in the local Mn environment acts as a precursor to the metamagnetic phase transition and that the critical a parameter we found previously was a signature of this phys-

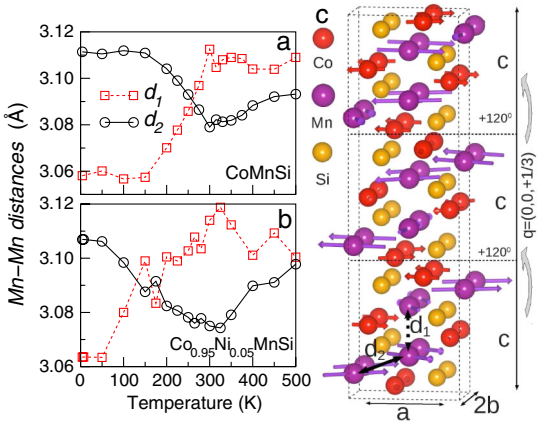

FIG. 2 (color online). Temperature variation of Mn-Mn nearest-neighbor distances d_1 and d_2 in CoMnSi (a) and $Co_{0.95}Ni_{0.05}MnSi$, (b) from HRPD. As with $a(T)$, the fastest variation of d_1 and d_2 occurs well below T_t. The crystallographic positions of d_1 and d_2 are shown in (c), together with the closest commensurate version (for clarity, as modeled later) of the helical spin structure adopted by Co and Mn [9]. Three unit cells are shown in the c direction, drawn using VESTA [10].

ics. We leave the temperature dependence of the magnetic propagation vector to future studies as it lies outside the low-angle limit of HRPD.

We previously observed that in a magnetic field the Néel transition becomes a metamagnetic one to a high magnetization state at temperature T_t. As the applied field is increased T_t decreases sharply before going through a tricritical point where the onset of a finite latent heat and enhanced magnetocaloric effects are observed [11]. We can observe the change in a during this field-induced transition by measuring the forced magnetostriction of $Co_{0.95}Ni_{0.05}MnSi$ samples. We chose samples that were given an a-direction texture by the rf field during formation. Such texturing is seen from a comparison of bulk thermal expansion data taken with the dilatometer with that from HRPD on powder (see Fig. 1). In Fig. 3 we show both the magnetization and the magnetostriction of $Co_{0.95}Ni_{0.05}MnSi$ as a function of applied field at different temperatures. Magnetostriction is defined here for a polycrystal as $\lambda^{\parallel,(\perp)} = [l(H) - l(H=0)/l(H=0)]$, where $\lambda^{\parallel}$ means the strain measured parallel to the applied magnetic field and $\lambda^{\perp}$ perpendicular to it. We see the same tricritical point in both signals, as given by the onset of hysteresis. Given the correlation between a-axis NTE and the giant change in d_1 and d_2 we would expect that the field-induced change in d_1 and d_2 also becomes first order at this point. Tricriticality occurs at a critical field of $\sim$2 Tesla, or at around 200 K and this temperature is relatively close to completion of the crossover in d_1 and d_2 shown in Fig. 2. We may thus assume that tricriticality occurs when the applied field drives T_t low enough to couple to the giant underlying change in d_1 and d_2. Neutron studies are planned to explore this hypothesis.

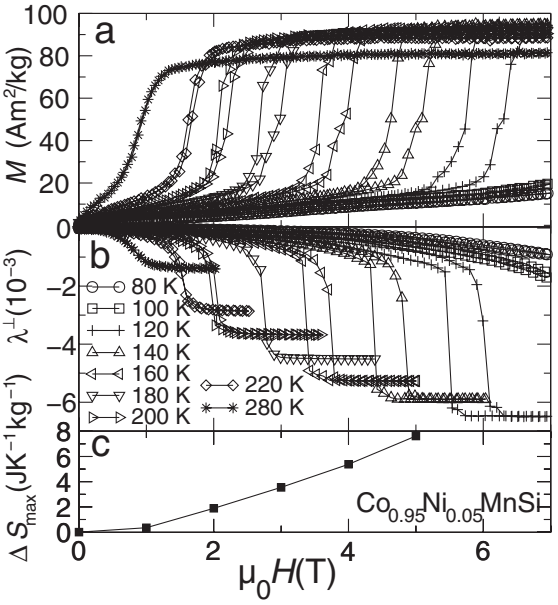

FIG. 3. (a) Isothermal magnetization of bulk $Co_{0.95}Ni_{0.05}MnSi$. (b) Transverse magnetostriction of a textured polycrystal of the same material. Magnetostriction is dominated by the a-axis texture of the sample (see Fig. 1). The onset of tricriticality is marked by an increase in both magnetostriction and the peak MCE (c).

Further evidence for such a conjecture is provided by using the above magnetization measurements to calculate the MCE in both CoMnSi and $Co_{0.95}Ni_{0.05}MnSi$ shown in Fig. 3(c). We see an enhancement of peak isothermal entropy change associated with the metamagnetic transition once the system goes through its tricritical point. This feature again coincides with the temperature of maximal zero-field variation of $a(T)$. Entropy changes here are calculated from isothermal magnetization curves using a Maxwell relation as in [4] after confirming the reversibility of the metamagnetic phase transition.

We may explain our findings and their relevance by examining structural and magnetic data on other CoMnX materials in the same space group (X = P, Ge). The detailed temperature variation of Mn-Mn separations is missing from previous studies, but for our purpose we may examine trends that link materials characterized at room temperature. In Fig. 4 we show the values of d_1, d_2 and the unit cell parameters found in literature studies of CoMnP, CoMn(Si,Ge), and CoMnGe [4,12–14]. On increasing the size of the p-block element, both the b and c parameter increase while the a parameter decreases. More notably we see a crossover in d_1 and d_2 that occurs near to the lattice dimension of CoMnSi, where the collinear ferromagnetism found in CoMnP and CoMnGe gives way to noncollinear antiferromagnetism. We note that d_1 has the stronger variation and may be the more important parameter. The plot shows that other materials in the space group, if engineered to give similar values of d_1 and d_2, may possess the same competing exchange, giant magnetoelastic coupling, and tricritical metamagnetism as found in CoMnSi.

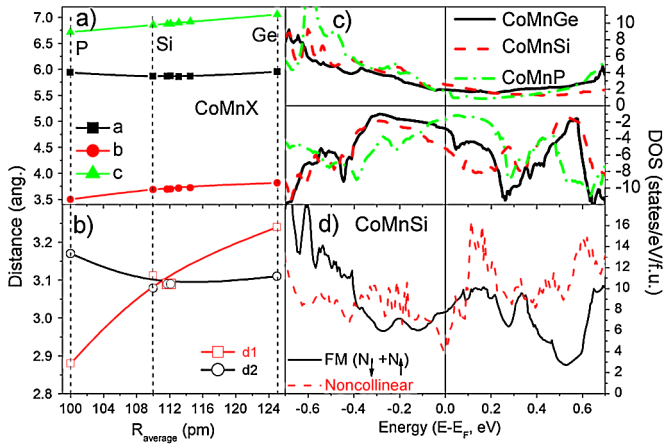

FIG. 4 (color online). A comparison of CoMnX (X = P, Si, Ge). (a) and (b) show literature-derived lattice parameters and d_1, d_2 at 300 K as a function of average p atom size [4,12–14]. In (c) we show the electronic densities of states (DOS) majority (upper figure) and minority (lower figure) spins near the Fermi energy, E_F calculated for a ferromagnetic (FM) ground state. In (d) we see that the calculated DOS at E_F of noncollinear AFM CoMnSi is lower than that of a fictitious FM ground state.

The fact that exchange competition drives large magnetoelastic coupling is unusual. We believe that the large magnetoelastic coupling found here is the result of a close competition between the relevant Mn-Mn and Mn-Co exchange interactions, and the energetic proximity of ferromagnetic, or low-q spin configurations that correspond to quite different Mn-Mn separations. To demonstrate the origin of the noncollinear AFM state and its energetic relation to ferromagnetic (FM) spin arrangements we have undertaken electronic structure calculations with the VASP code, based on density-functional theory (DFT) [15]. Details of the calculation are given elsewhere [16]. For a collinear FM state, we find that the calculated site-projected magnetic moments, together with the total magnetic moment per formula unit are fairly independent of the nature of the p-block atoms and are in accordance with the experimental findings by neutron diffraction in the cases of ferromagnetic CoMnP and CoMnGe [17,18]. On the other hand, for CoMnSi a FM ground state gives $M_{\mathrm{Mn}} = 2.88\mu_B$ which overestimates the magnetic moment of the true noncollinear state ($M_{\mathrm{Mn}} \sim 2.2\mu_B$ [9]). Importantly we find no orbital contribution to the magnetic moment, and this confirms the simple picture of Mn being in a d^5 (Mn^{2+}) state giving rise to zero orbital angular momentum, if Hund's rule of maximum multiplicity is applied and each d level is singly occupied. We therefore believe the spin-orbit contribution to magnetoelastic coupling is much weaker than that due to exchange competition.

The calculated density of states (DOS) near the Fermi level of a collinear FM state are shown in Fig. 4 for CoMnX. A valley with an energy minimum at the Fermi level is observed for CoMnP in both minority and majority spins. The calculated total density of states [$N_{\mathrm{tot}}(E_F) = N_\uparrow + N_\downarrow$] for CoMnP (1.7 states/eV/f.u.) and for CoMnGe (5 states/eV/f.u.) is considerably lower than 9 states/eV/f.u. found for CoMnSi when forced to be ferromagnetic. In the latter case, the high number of states makes ferromagnetism unstable and promotes a noncollinear AFM arrangement as was reported earlier in similar Mn-based orthorhombic systems [19,20]. This stability argument may be understood from either a Stoner viewpoint, whereby a magnetically ordered state is favored by the reduction of DOS at the Fermi energy, or as an extension of the picture in covalently bonded materials, where stability is found by maximally occupying the electronic bonding states. We find direct evidence for such a lowering of $N_{\mathrm{tot}}(E_F)$ in the AFM case by also calculating the DOS of a commensurate [$\mathbf{q} = (0, 0, 1/3)$] version of the helical magnetic structure found in CoMnSi (See Fig. 2 and Ref. [9]). The Mn states are less split by exchange in the noncollinear AFM state, as indicated by the partial density of states plots (PDOS, not shown here). The reduced exchange in this state shifts the steep valley seen in N_{tot} at $\sim$0.5 eV to the Fermi level, stabilizing noncollinear AFM, as seen in Fig. 4. A change in temperature or applied field is sufficient, however, to bring about a change in magnetic structure and hence atomic separations.

In summary, we have shown that in materials with a composition close to CoMnSi there is giant magnetoelastic coupling evidenced by a crossover in nearest Mn-Mn separations. In particular, the nearest neighbor separation can change by up to 2%, away from the helimagnetic Néel temperature. We have shown that this coupling is the precursor to a metamagnetic tricritical point with enhanced magnetostrictive and magnetocaloric effects. While this is the largest magnetoelastic coupling seen in a metallic magnet, it should be possible to engineer materials of different compositions that have the same structural instability due to highly sensitive noncollinear AFM ordering. Future experiments will examine the magnetic field dependence of Mn-Mn separations and the magnetic structure.

We thank M. Avdeev, R. Bali, L. Cohen, and K. Morrison for useful discussions, K. Roberts for help with sample preparation, and G. G. Lonzarich for use of sample synthesis facilities. A. B. would like to thank EPSRC and Camfridge Ltd. for financial support. K. G. S. acknowledges financial support from The Royal Society. The research leading to these results has received funding from the European Community's 7th Framework Programme under grant agreement No. 214864, as well as The Newton Trust and The Leverhulme Trust. Computing resources provided by Darwin HPC and Camgrid facilities at The University of Cambridge and the HPC Service at Imperial College London are gratefully acknowledged.

[1] A. N. Vasil'ev *et al.*, Phys. Rev. B **59**, 1113 (1999).
[2] S. Lee *et al.*, Nature (London) **451**, 805 (2008).
[3] O. Tegus *et al.*, Nature (London) **415**, 150 (2002).
[4] K. G. Sandeman *et al.*, Phys. Rev. B **74**, 224436 (2006).
[5] M. S. Reis *et al.*, Phys. Rev. B **77**, 104439 (2008).
[6] C. Becerra *et al.*, Phys. Rev. Lett. **44**, 1692 (1980).
[7] M. Rotter *et al.*, Rev. Sci. Instrum. **69**, 2742 (1998).
[8] A. C. Larson *et al.*, Los Alamos National Laboratory LAUR Report No. 86-748, 1994.
[9] S. Nizioł *et al.*, Phys. Status Solidi A **45**, 591 (1978).
[10] K. Momma and F. Izumi, J. Appl. Crystallogr. **41**, 653 (2008).
[11] K. Morrison *et al.*, Phys. Rev. B **79**, 134408 (2009).
[12] D. Fruchart, M. Bacmann, and Paul Chadouet, Acta Crystallogr. Sect. B **36**, 2759 (1980).
[13] S. Nizioł, R. Fruchart, and J. P. Senateur, J. Magn. Magn. Mater. **15–18**, 481 (1980).
[14] S. Nizioł *et al.*, J. Magn. Magn. Mater. **27**, 281 (1982).
[15] G. Kresse and J. Furthmüller, Phys. Rev. B **54**, 11 169 (1996).
[16] Z. Gercsi and K. G. Sandeman, arXiv:1003.5193.
[17] S. Fujii *et al.*, J. Phys. F **18**, 971 (1988).
[18] S. Kaprzyk and S. Nizioł, J. Magn. Magn. Mater. **87**, 267 (1990).
[19] B. Sredniawa *et al.*, J. Alloys Compd. **317–318**, 266 (2001).
[20] R. Zach *et al.*, J. Phys. Condens. Matter **19**, 376201 (2007).

Thermomagnetic irreversibility in $Ni_2Mn_{1.36}Sn_{0.64}$ shape-memory alloy

S. Chatterjee, S. Giri, and S. Majumdar*
Department of Solid State Physics, Indian Association for the Cultivation of Science, 2A & B Raja S. C. Mullick Road, Jadavpur, Kolkata 700 032, India

S. K. De
Department of Materials Science, Indian Association for the Cultivation of Science, 2A & B Raja S. C. Mullick Road, Jadavpur, Kolkata 700 032, India

(Received 11 April 2008; revised manuscript received 12 May 2008; published 27 June 2008)

The ferromagnetic shape-memory alloy of nominal composition $Ni_2Mn_{1.36}Sn_{0.64}$ has been investigated by electronic transport and magnetic studies. The thermoelastic martensitic transition is strongly influenced by the applied magnetic field as observed in our resistivity and magnetization measurements. The field-cooled and the zero-field-cooled resistivities show large divergence below the transition temperature. It is evident that the field cooling through the martensitic transition produces a fraction of arrested austenitic phase, which persists even down to the lowest temperature of measurement. The field-cooled resistivity shows large relaxation signifying the nonequilibrium character of the state. The close interplay between magnetization and the structural phase of the sample plays important role toward the formation of this undercooled arrested state. A parallelism is drawn between the field-induced anomalies observed in the present shape-memory alloy and some manganites showing insulator-metal transition.

DOI: 10.1103/PhysRevB.77.224440 PACS number(s): 75.60.Nt, 81.30.Kf, 75.30.Kz

I. INTRODUCTION

The coupling between magnetic and structural degrees of freedom in a solid can lead to intriguing physical properties, which have immense importance both from fundamental and technological point of views. In case of many intermetallic alloys and compounds, magnetic field-induced structural transition is responsible for various functional behaviors such as giant magnetocaloric effect,[1] colossal magnetostriction,[2] magnetic superelasticity,[3,4] giant magnetoresistance[5–7] etc. Some striking properties of the perovskite based manganese oxides also originate from magnetostructural instabilities.[8] As a result of the first-order nature of the transition, metastable states are formed,[9] and the system can show fascinating dynamics resulting from the competition between thermal and magnetic energies. Considering the growing interests in various systems showing magnetostructural instabilities, it is pertinent to understand the thermomagnetic behavior of systems with such competing interactions.

Heusler based ferromagnetic shape-memory alloys (FSMAs)[10] are interesting *biferroic* materials showing both ferroelasticity (development of spontaneous strain) and ferromagnetism (development of spontaneous magnetization). Recently, $Ni_2Mn_{1+x}Sn_{1-x}$ based FSMAs have attracted considerable attention due to their remarkable magnetofunctional properties such as shape-memory effect, inverse magneto caloric effect, and giant magnetoresistance around the martensitic transition (MT).[11–14] These are primarily related to the field-induced structural transition, which has been confirmed by x-ray diffraction experiment.[14] Application of magnetic field near MT induces a reverse transition, where the martensitic fraction transforms into austenite. This transition was found to be highly irreversible in most of the $Ni_2Mn_{1+x}Sn_{1-x}$ alloys i.e., one cannot recover the transformed fraction by simply withdrawing the field. Recently, we observed interesting *return point memory effect* in $Ni_2Mn_{1.4}Sn_{0.6}$ arising from the field arrested austenite state.[13] Formation of a field-induced low-temperature glassy magnetic state has been reported for the isostructural indium alloy.[15] Evidently, these materials are an ideal system for studying the effect of H and T variation across the MT. The present investigation was performed on the polycrystalline sample of nominal composition $Ni_2Mn_{1.36}Sn_{0.64}$ and it is mainly based upon the detailed magnetotransport studies on the alloy. $Ni_2Mn_{1.36}Sn_{0.64}$ contains less manganese than our previously studied sample $Ni_2Mn_{1.4}Sn_{0.6}$ and it has much lower value of the martensitic transition temperature. We observe intriguing history dependence with respect to the parameters, H and T, manifesting magnetically arrested states, which posses a remarkable resemblance with some manganites showing first-order insulator-metal transition.

II. EXPERIMENTAL DETAILS

The polycrystalline sample of composition $Ni_2Mn_{1.36}Sn_{0.64}$ was prepared by argon arc melting and subsequent annealing. The room-temperature powder x-ray diffraction pattern confirms that the material is a single-phase alloy with $L2_1$ cubic structure having lattice parameter, $a = 5.99$ Å. The magnetization (M) was measured by Quantum Design SQUID magnetometer (MPMS 6, Ever-cool model). The resistivity (ρ) was measured using a commercial cryogen free high magnetic-field system from Cryogenic Ltd., U.K. in the temperature (T) range 5–300 K and in presence of magnetic field 0–90 kOe. The sample space of the system is always filled up with He exchange gas for good thermal stability and the temperature fluctuation was less than 20 mK during the isothermal measurements.

III. RESULTS

Figure 1 shows the ρ versus T data recorded at 0 and 50 kOe of field with different protocols. In the zero-field data

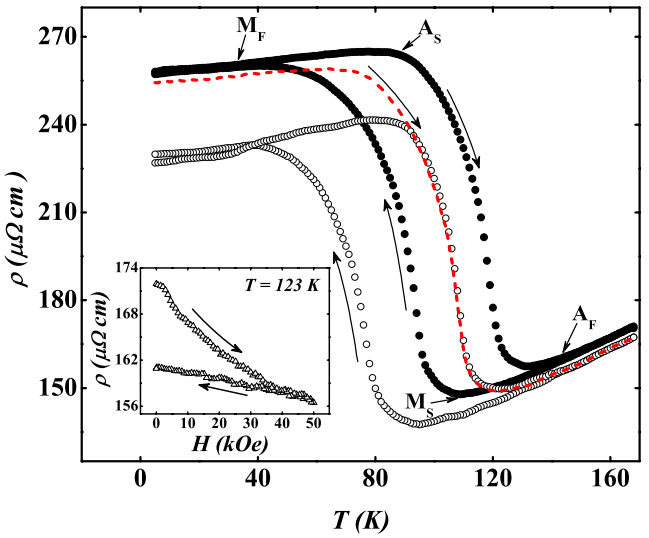

FIG. 1. (Color online) Resistivity as a function of temperature at zero field (filled circles) and 50 kOe field (open circles) for both cooling and subsequent heating sequences. The dashed line indicates resistivity measured by heating the sample at 50 kOe of field after the sample being zero-field-cooled down to 5 K. The inset shows the resistivity at 123 K for both field increasing and decreasing branches.

(filled circles), clear thermal hysteresis is observed between the heating and cooling measurements in the range 35–155 K, signifying the first-order MT in the alloy. For an applied magnetic field (H) of 50 kOe, the field cooling and subsequent field-heating data (open circles) show similar thermal hysteresis, however, now the high-T end point of the loop is shifted to lower temperatures along with the lowering of the magnitude of ρ. This is related to the field-induced transition near the magnetostructural instability and gives rise to magnetoresistance (MR) as large as −30%. Notably, $\rho(T)$ (open circles) measured in $H=50$ kOe during field cooling and field heating do not approach the zero-field data (filled circles) below the MT, rather they remain *well below* in magnitude and run parallel to the zero-field data and considerable MR (−12%) is observed down to the lowest temperature of measurement. The MR arising from the magnetostructural transition is likely to be observed in the vicinity of the MT. However, for the present sample, it appears that the reduced value of ρ in presence of H is carried over well below the region of thermal hysteresis. This is a magnetothermal arrest of the low-ρ phase, which remains arrested even when the sample is cooled below the MT and subsequently heated back in field. Now let us look at the zero-field-cooled but field-heating data (dashed line), where the sample was heated from 5 to 300 K in $H=50$ kOe after being zero-field-cooled to 5 K. Here, $\rho(T)$ is almost same to that of the zero-field run below the MT, decreases considerably as it enters into the region of thermal hysteresis and then above the MT, it again approaches the zero-field data. We therefore observe a large deviation between the field-cooled field-heating (open circles) and zero-field-cooled field-heating (dashed line) data measured at $H=50$ kOe. The deviation starts to emerge from 90 K, which is well inside the region of thermal hysteresis.

We have recorded isothermal ρ versus H data at 123 K (inset of Fig. 1), where a clear irreversibility is observed

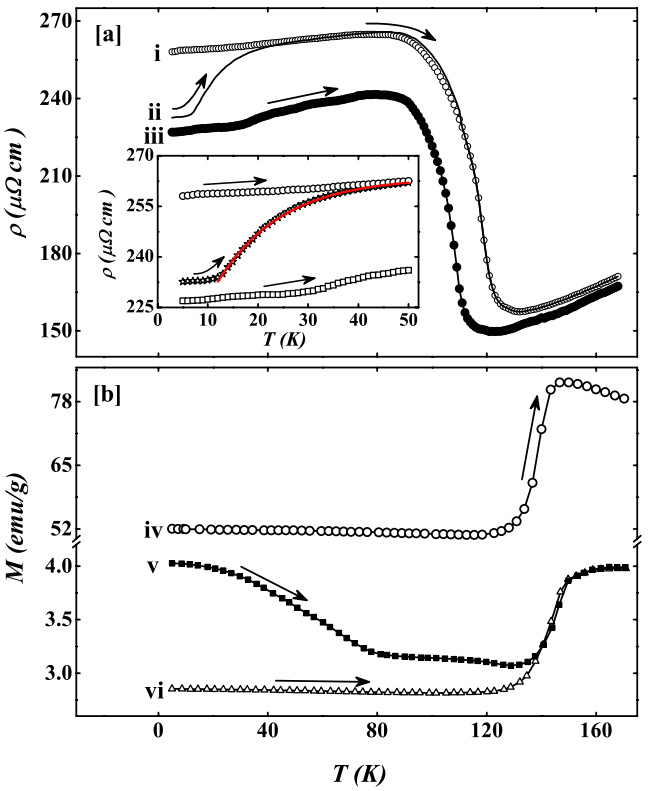

FIG. 2. (Color online) (a) Resistivity recorded while heating in (i) zero field after being zero-field cooled, (ii) zero field after being field cooled in $H=50$ kOe and (iii) 50 kOe after being field-cooled in $H=50$ kOe. (b) Magnetization recorded while heating in (iv) 50 kOe after being field cooled in 50 kOe, (v) 100 Oe of field after being field cooled in $H=50$ kOe (vi) 100 Oe of field after being field cooled in 100 Oe.

between the field increasing and decreasing branches. The application of field brings down ρ, however, when the field is ramped down to zero, ρ remains arrested in its *low value* state. The irreversibility in $\rho(H)$ is actually the manifestation of irreversibility of the magnetostructural transition of the sample. The observed anomaly in the field-cooled ρ versus T emerges out of this field induced arrest of the low-ρ state, which remains arrested even when the sample is cooled down to 5 K.

In order to shed more light on this interesting thermomagnetic behavior, we collected heating $\rho(T)$ and $M(T)$ data with different protocols as depicted in Fig. 2. $\rho(T)$ was recorded in varied conditions, such as (i) zero-field-cooled (ZFC) and then zero-field heating, (ii) field-cooled (FC) in $H=50$ kOe and zero-field heating, (iii) cooled in $H=50$ kOe and heating in 50 kOe. Starting from the lowest T, curve (iii) remains well separated from curve (i), which is the effect of field cooling across the magnetostructural transition. If we look at curve (ii), it also remains well below curve (i) [rather close to curve (iii)] at the lowest temperature. However, above about 10 K (see the inset for a zoomed view), it starts to approach curve (i) and eventually joins up with it above 50 K. It depicts that the field cooling produces a *nonequilibrium* state which persists even when the field is removed at the lowest temperature, nevertheless it tends to the *equilibrium* ZFC

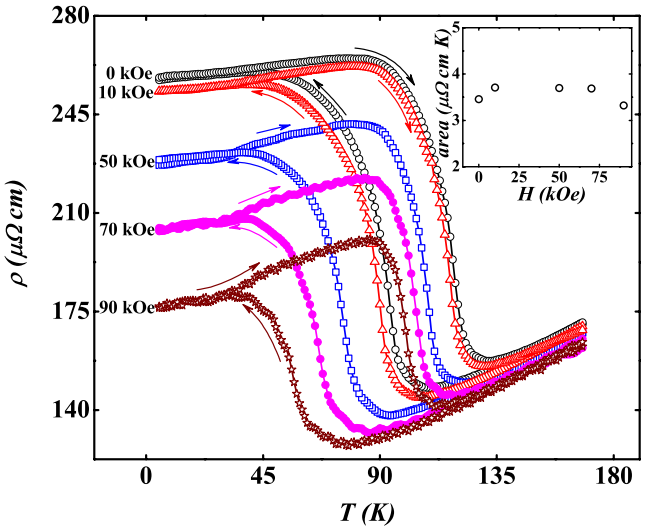

FIG. 3. (Color online) Field cooling and field-cooled heating resistivity data measured at different applied fields. The inset shows the area of the thermal hysteresis loops as a function of H.

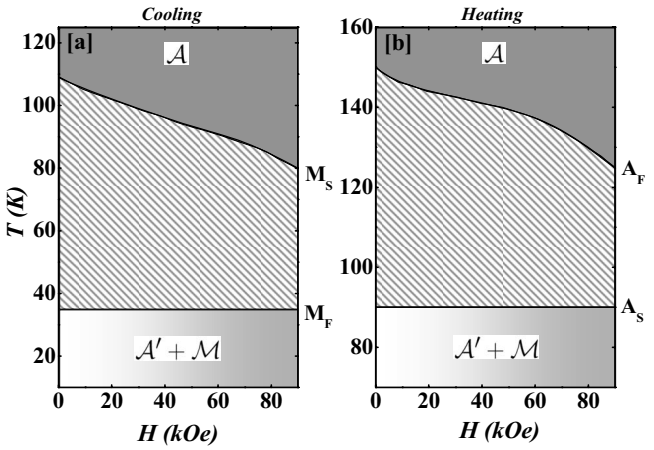

FIG. 4. The H-T phase diagram of the sample for cooling and heating in a field H. Here, $\mathcal{A}$ denotes the high-temperature phase, $\mathcal{M}$ is the martensite phase, and $\mathcal{A}'$ is the field arrested undercooled austenite phase. The stripes (between M_S and M_F in case of cooling and between A_F and A_S in heating) denote the region of thermoelastic martensitic transition.

state once we increase the temperature. Interestingly, curve (ii) shows an exponential behavior as it approaches curve (i) [a fitted line is shown in the inset of Fig. 2(a)], with an empirical law of temperature dependence: $\rho(T)=A-B\exp(-T/T_0)$, here A, B, and T_0 are fitting parameters. Our fitting to the data gives T_0 to be 12 K, which is very close to the temperature from where curve (ii) starts to rise. This shows that field cooling in 50 kOe produces a metastable state which is separated from the equilibrium state by a barrier of height of about 12 K.

The magnetization data also show similar field-cooling effect. In Fig. 2(b), curves (iv) and (v) are measured while heating in $H=50$ kOe and 100 Oe, respectively, after both being field-cooled in 50 kOe. In case of curve (vi), the sample was field cooled in 100 Oe and $M(T)$ was measured in 100 Oe during heating. Therefore, the magnetization curves (iv), (v), (vi) are equivalent to the resistivity curves (iii), (ii), (i), respectively, except only the fact that instead of zero field, M was measured in a low field of 100 Oe. We find strong effect of field cooling, as the curves (v) and (vi) differ from each other. The difference is maximum at the lowest temperature, but as the sample is warmed up, curve (v) approaches curve (vi), signifying the unblocking of the field arrested state under heating in low field (100 Oe).

Figure 3 shows $\rho(T)$ measured at different fields with hysteresis loops consisting of field-cooling and field-heating branches. Our $\rho(T)$ measurement up to the field strength of 90 kOe indicates that thermally driven MT survives till such a high field, but it is strongly modified by the metamagnetic transition. Grossly, the loop shifts to lower T with increasing H. MT is characterized by four temperatures, namely M_S, M_F while cooling, and A_S and A_F while heating. Martensite starts to develops from M_S and the transition completes at M_F. Similarly, A_S and A_F signify austenite start and finish temperatures, respectively, while heating. Roughly, M_F and A_F are low-T and high-T end points of the hysteresis loop, while M_S is the minimum point and A_S is the maximum point in the T-decreasing and T-increasing branches (marked in Fig. 1) of the ρ versus T data. With the application of H, M_S shifts to lower T and for 0 to 90 kOe of field change, $\Delta M_S=33$ K. Similarly, we observe $\Delta A_F=30$ K. M_F and A_S remain almost constant under an applied magnetic field. The magnitude of ρ gets suppressed below A_F under H and the hysteresis loop becomes fatter but shorter with increasing H. Interestingly, the area under the thermal hysteresis loops remain almost constant for different applied fields (see inset of Fig. 3).

It is clear from the previous data that the field cooling produces a state with lower ρ and higher M than the ZFC state. The sample has been reported to show martensite to austenite transformation under H. Considering the fact that austenite is electrically less resistive and having higher magnetic moment than martensite, the field cooling through MT actually produces some austenite fraction, which survives even when the sample is cooled below the martensite finish temperature, M_F. As a result, the FC resistivity decreases with increasing field, signifying the development of more and more arrested austenite fraction with increasing H. Figure 4 shows the H-T phase diagram of the sample for cooling and subsequent heating in a field H. In the cooling data, the line M_S separates the pure austenite and the low-temperature mixed phase occurring due to the thermoelastic MT. The line M_F, which indicates the end of thermoelastic transition, is found to be insensitive to the cooling field. Below this line, the arrested austenite ($\mathcal{A}'$) is indicated by shades, which increases with increasing H. On the heating H-T diagram [Fig. 4(b)], the existence of the arrested austenite, $\mathcal{A}'$ is indicated below the starting point of the thermoelastic transition, A_S. We observe that unlike M_S and A_F, the characteristic temperatures A_S and M_F hardly change with changing field. This is possibly due to the fact that the effect of H is to create arrested austenite out of metastable martensite only, and the martensite phase is metastable between the temperatures M_S and A_F.

A metastable state is defined as a state corresponding to the local minimum in the free-energy configuration separated

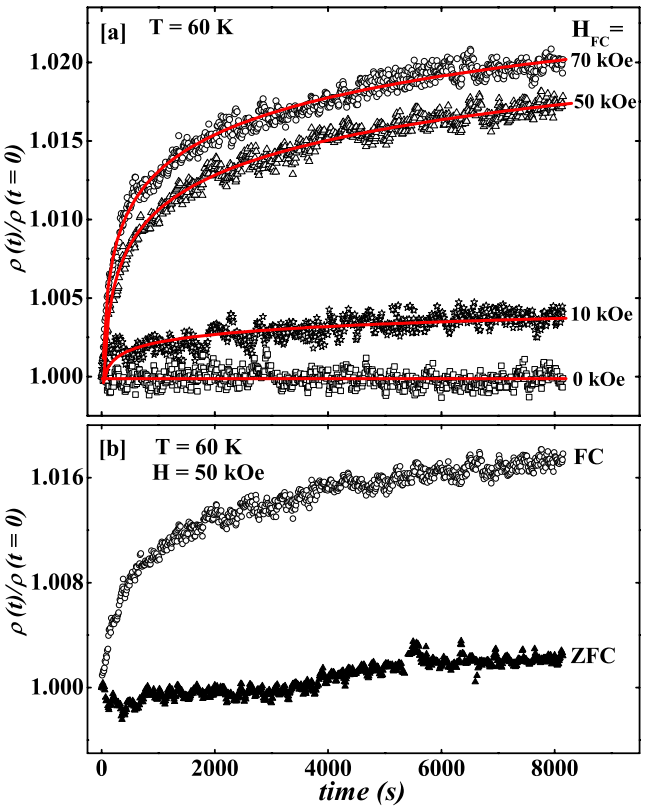

FIG. 5. (Color online) (a) The upper panel depicts normalized resistivity as a function of time at 60 K. The relaxation measurements were performed after the sample was field cooled in a particular field H_{FC} down to 5 K, heated back to 60 K, and then removing the field H_{FC}. The solid lines are the logarithmic fit to the data. (b) Relaxation of resistivity at 60 K for two different protocols, namely FC, where the sample was field cooled in $H=50$ kOe down to 5 K, heated back to 60 K and relaxation was measured by removing the field, and ZFC, where the sample was zero-field-cooled down to 5 K and at this temperature 50 kOe of field was applied and the sample was allowed to heat up to 60 K, and then the relaxation was measured by removing the field.

by an energy barrier from the equilibrium state. For $T \neq 0$, the thermal energy can assist the system to evolve into the equilibrium configuration. It is therefore interesting to see how the resistivity in the arrested FC state relaxes with time (t). Figure 5(a) depicts the relaxation of ρ as a function of time at 60 K. The sample was field cooled to 5 K in $H=H_{FC}$, heated back to 60 K in the same field and then ρ was measured as a function of time after the removal of the field H_{FC}. Once the field is removed, ρ quickly attains a value close to the zero-field resistivity, $\rho_{H=0}$ [curve (i) of Fig. 2]. On the heating branch, 60 K is a temperature that is too high to keep the austenite arrested completely. After that it sluggishly increases toward $\rho_{H=0}$ with t. We measured $\rho(t)$ for about 8000 s, and a reasonably large relaxation in ρ was observed (about 2.1% for $H_{FC}=70$ kOe). In our measurement, $t=0$ denotes the time when the field is completely removed. In all cases ρ increases with t and it asymptotically approaches the zero-field value. The sluggish rise of ρ for $t>0$ depends strongly upon H_{FC}, and it is clearly seen that the relaxation is more prominent for higher H_{FC}. This is not surprising because a higher value of H_{FC} will create a higher fraction of arrested metastable state. At zero applied field, the sample does not show any relaxation due to the absence of field-induced metastability. We observe a logarithmic evolution of ρ with time: $\rho(t)/\rho(t=0)=1+S_\rho \ln(t/t_0)$, where t_0 and S_ρ are the fitting parameters [solid lines in Fig. 5(a)]. A logarithmic relaxation of physical parameters is well established and it can happen due to the thermal excitation of the system across the distribution of energy barriers.[16] The coefficient of the logarithmic term, S_ρ, increases sharply with increasing H_{FC}.

One can argue that the observed relaxation is simply due to the finite reaction time of a ferromagnetic sample such as $Ni_2Mn_{1.36}Sn_{0.64}$ to the removal of a magnetic field. In order to rule out the possibility, we measured the relaxation of ρ at 60 K after removing the field (50 kOe) for both FC and ZFC protocols [see Fig. 5(b)]. In case of FC, the sample was field-cooled in 50 kOe down to 5 K and heated back to 60 K in field, while in ZFC case, the sample was zero-field-cooled down to 5 K, 50 kOe field was applied and then heated back in field to 60 K. Clear signature of relaxation is observed in case of FC state, while for the ZFC case, the relaxation is insignificant. It signifies that the field cooling through the MT has distinctive effect on the electronic state of the system. A mere application of field below 60 K on the ZFC state cannot produce the nonequilibrium state, which can relax with time.

IV. DISCUSSION

The present system is an interesting example where we observe a mutual coexistence of thermally driven MT and the field driven reverse transition, both first order in nature, which together give rise to a complex H-T behavior. Similar interplay between two orderings are observed in other systems such as multiferroic materials (ferromagnetic and ferroelectric)[17] and intermetallic alloy such as $ZrZn_2$,[18] where superconductivity and ferromagnetism coexist. However, as far as the magnetothermal properties are concerned, $Ni_2Mn_{1.36}Sn_{0.64}$ shows remarkable similarities with the manganite compounds, $(Nd,Sm)_{0.5}Sr_{0.5}MnO_3$.[8,19] Here, the temperature driven first-order ferromagnetic (FM) to charge-order (CO) transition gets shifted to lower temperature with the applied magnetic field, which signify a field-induced reverse CO to FM transition. Consequently, H tries to stabilize the FM phase and a field-cooling through the first-order CO-FM transition (which is also associated with a insulator-metal transition) gives rise to metastable metallic FM fraction below the region of thermal hysteresis (see Fig. 1 of Ref. 19) that persists down to the lowest temperature. The development of this FM phase due to the field cooling in case of $(Nd,Sm)_{0.5}Sr_{0.5}MnO_3$ is very similar to the development of FC austenite phase in the present sample. The fraction of metastable FM phase at low temperature increases with increasing H and it was observed that beyond a certain value of H (above 60 kOe for $Nd_{0.5}Sr_{0.5}MnO_3$), the CO state gets completely molten. These manganite samples also show similar thermomagnetic irreversibility between the FC and ZFC measurements.[20,21]

The irreversibility between temperature dependence of FC and ZFC magnetization is quite common in case of glassy magnetic materials. This is attributed to the random freezing of the spins during the zero-field-cooling. The ZFC state is a nonequilibrium state and it approaches the FC state with time $[M_{ZFC}(t\rightarrow\infty)\approx M_{FC}]$.[22] In contrary to this, the FC state is found to be more metastable in case of $Ni_2Mn_{1.36}Sn_{0.64}$ than the ZFC one. As observed in Fig. 2, the FC ρ approaches the ZFC ρ on the heating branch once the field is removed. This is an example of *reentrant transition*, where by virtue of the zero-field heating of the field-cooled state up to above MT, a transition such as "arrested austenite" $(\mathcal{A}')\rightarrow$ "martensite" $(\mathcal{M})\rightarrow$ "austenite" $(\mathcal{A})$ occurs. The equivalent re-entrant transition in $(Nd,Sm)_{0.5}Sr_{0.5}MnO_3$ is the collapse of the arrested FM state into CO state on heating.

We observe strong time dependent effect of ρ in the FC state, which is practically absent in the ZFC state. This evidence of metastability of the FC state can be due to some arrested austenite fraction, which gradually converts to martensite with time. Another likely source of this metastability is the preferential nucleation of martensite under an applied magnetic field. Recently, Aksoy *et al.*[23] have reported the result of their T-dependent strain measurements in presence of H in several Ni-Mn-X (X=In,Sn,Sb,Ga) based FSMAs. It is observed that during cooling through M_S in presence of H, the martensite variants are grown with their easy axis of magnetization directed along the direction of applied field. However, growth is random when the sample is cooled in zero field. The observed relaxation in the FC state of the present sample can be related to this preferential nature of the variant growth. When the field is removed below M_S, the oriented variants tend to get randomized by the thermal energy with time. The randomized variants would offer more resistance due to the enhanced scattering of electrons from the interfaces and as a result a time dependent increase of resistance is expected.

The thermal hysteresis observed in the present sample around the MT is inherently related to the supercooling and superheating of high-T and low-T phases, respectively. In the standard notation of first-order phase transition, the extent of metastability is bound between the temperatures, T^{**} and T^{*}.[24] In case of MT, the temperatures M_F and A_F are equivalent to T^{*} and T^{**}, respectively. Below T^{*}, the supercooled state becomes unstable, and the system completely transform into low-T phase. Similarly, above T^{**}, the superheated state cannot survive. In real system, the presence of disorder and/or impurity can locally reduce the free-energy barrier, causing the low-T (or high-T) phase to nucleate even above T^{*} while cooling (or below T^{**}while heating).[25] Therefore, one can have phase coexistence in the region of hysteresis.[9] Polycrystalline sample such as $Ni_2Mn_{1.36}Sn_{0.64}$ is expected to possesses disorder/defects, and it will have both high-T austenitic and low-T martensitic phases in the region around MT where the thermal hysteresis is observed. With increasing H, ρ decreases (and simultaneously M increases) gradually, signaling monotonic increase of austenitic fraction at the expense of martensite. This is quite different from the sharp field-induced transition at a critical field in case of Gd_5Ge_4,[26] RCo_2 (R=rare earth) Laves phase compounds,[27] or B-site doped Perovskite oxides.[28] Possibly, in case of Mn-based Heusler alloys, the application of H in the region of transition, causes the free-energy barrier to decrease. The higher the magnetic field, the effect on the free-energy barrier is stronger, causing the development of more austenite by thermal activation. In other words, the austenite does not equilibrate with the sudden collapse of the barrier at a critical field. In addition, disorder gives a spatial variation of the free-energy profile, as a result, the threshold field for the martensite to austenite transition will vary over the sample. In effect, this will cause a gradual melting of the martensite with increasing H.

However, the above picture of first-order phase transition is inadequate to account for the complex H-T phase diagram in $Ni_2Mn_{1.36}Sn_{0.64}$. Considering the fact that T^{*} (or M_F) denotes the end point of metastability in the low-T side, one would not expect the formation of arrested state well below M_F. In addition, the Zeeman energy term ($-MH$) is too weak to play a significant role for a large change in M_S under H. We need to remember that in the present case the elastic strain and magnetization are closely interconnected. Landau free energy (F_L) with biquadratically coupled order parameters has been used for magnetostructural transition in manganites such as $La_{1-x}Sr_xMnO_3$ and $Nd_{0.5}Sr_{0.5}MnO_3$.[8,19,20] A similar model can be appropriate in the present case, where

$$F_L = f_0 + \alpha(T-T_C)M^2 + \beta M^4 - MH + \alpha'(T-T_0)\sigma^2 + \beta'\sigma^4 + \gamma'\sigma^6 + \lambda M^2\sigma^2. \quad (1)$$

Here, M and σ (strain) are two order parameters corresponding to second-order ferromagnetic transition and first-order MT, respectively. The term $\lambda M^2\sigma^2$ denotes the coupling between magnetic and elastic energies and $-MH$ is the Zeeman energy term. This free energy can bear the high-temperature ferromagnetic ordering (at T_C) and austenite to martensite transition (at T_0). However, for suitable values of the coefficients, it can give rise to a first-order transition line, where the free-energy minimum for the martensite is low enough for structural ordering, and a metastable austenite (a metallic ferromagnetic state in case of manganite) prevails down to low temperatures.[29] In the present case, this undercooled austenite phase might be primarily responsible for the lower ρ and higher M in the field-cooled state of the sample.

In this connection, we would like to mention that the martensitic transition temperatures of $Ni_2Mn_{1+x}Sn_{1-x}$ alloys depend strongly on Mn concentration. It is believed that the excess Mn (denoted by x) gives rise to some short-range antiferromagnetic (AFM) correlations in the system and it plays an important role for the structural instability.[30] M_S shifts to higher T by 80 K for x changing from 0.36 (present sample) to 0.4. The x=0.4 sample also shows irreversibility in the ρ (and also M) versus H behavior in the region of MT due to field-induced transition, however, the presence of undercooled austenite phase in the FC data down to lowest temperature is absent here.[13] For x=0.4, the FC ρ approaches to the ZFC ρ as the temperature is lowered below the M_F of the sample. The MT occurs at much higher temperature in case of x=0.4, and possibly in presence of thermal fluctuations at relatively high T, the undercooled austenite cannot be stabilized here.

V. SUMMARY AND CONCLUSION

We have investigated the metastability associated with the structural transition in $Ni_2Mn_{1.36}Sn_{0.64}$ by carefully controlling the parameters such as magnetic field and temperature. The thermally driven martensitic transition is strongly influenced by the applied magnetic field. We observe a remarkable *H-T* phase diagram, where an undercooled austenite phase exists down to the lowest temperature. We have mooted the concept of coupled order parameter for the present sample, which predicts an undercooled state in certain situations. A notable similarity is seen between the present phenomenon with some manganites such as, $Nd_{0.5}Sr_{0.5}MnO_3$, showing first-order transition from ferromagnetic to charge-order state. The microscopic origin of the magnetic and structural aspects in Heusler alloys and manganites are quite different. The commonality in their bulk properties possibly lies to the fact that a generic statistical model for magnetostructural transition with two competing order parameters is obeyed by both the systems. It should be borne in mind that both manganites and the present FSMA are phase separated systems and AFM correlations play an important role toward the structural instability in both the systems.

The paramagnetic to FM and FM to CO transitions in $Nd_{0.5}Sr_{0.5}MnO_3$-derived compositions show strong hydrostatic pressure (P) effect. It can be equally interesting to investigate the effect of P on the sample and construct the *P-T* phase diagram, which will bring out correctness of the coupled model and will through more light on the fate of the metastable state under pressure.

ACKNOWLEDGMENT

We acknowledge the financial support from CSIR, India for the present work.

*sspsm2@iacs.res.in

[1] K. A. Gschneidner, Jr., V. K. Pecharsky, and A. O. Tsokol, Rep. Prog. Phys. **68**, 1479 (2005).
[2] L. Morellon, P. A. Algarabel, M. R. Ibarra, J. Blasco, B. García-Landa, Z. Arnold, and F. Albertini, Phys. Rev. B **58**, R14721 (1998).
[3] R. Kainuma, Y. Imano, Y. Sutou, H. Morito, S. Okaoto, O. Kitakam, K. Oikawa, A. Fujita, T. Kanomata, and K. Ishta, Nature (London) **439**, 957 (2006).
[4] T. Krenke, E. Duman, M. Acet, E. F. Wassermann, X. Moya, L. Mañosa, A. Planes, E. Suard, and B. Ouladdiaf, Phys. Rev. B **75**, 104414 (2007).
[5] L. Morellon, J. Stankiewicz, B. García-Landa, P. A. Algarabel, and M. R. Ibarra, Appl. Phys. Lett. **73**, 3462 (1998).
[6] P. A. Algarabel, M. R. Ibarra, C. Marquina, and A. del Moral, Appl. Phys. Lett. **66**, 3061 (1995).
[7] V. Sechovsky, L. Havela, K. Prokes, H. Nakotte, F. R. de Boer, and E. Brúck, J. Appl. Phys. **76**, 6913 (1994).
[8] A. Asamitsu, Y. Moritomo, R. Kumai, Y. Tomioka, and Y. Tokura, Phys. Rev. B **54**, 1716 (1996).
[9] For a review, see S. B. Roy and P. Chaddah, Phase Transitions **77**, 767 (2004).
[10] J. Enkovaara, A. Ayuela, A. T. Zayak, P. Entel, L. Nordstrom, M. Dubee, J. Jalkanen, J. Impola, and R. M. Nieminen, Mater. Sci. Eng., A **378**, 52 (2004).
[11] Y. Sutou, Y. Imano, N. Koeda, T. Omori, R. Kainuma, K. Ishida, and K. Oikawa, Appl. Phys. Lett. **85**, 4358 (2004).
[12] T. Krenke, M. Acet, E. F. Wassermann, X. Moya, L. Mañosa, and A. Planes, Nat. Mater. **4**, 450 (2005).
[13] S. Chatterjee, S. Giri, S. Majumdar, and S. K. De, Phys. Rev. B **77**, 012404 (2008).
[14] K. Koyama, K. Watanabe, T. Kanomata, R. Kainuma, K. Oikawa, and K. Ishida, Appl. Phys. Lett. **88**, 132505 (2006).
[15] V. K. Sharma, M. K. Chattopadhyay, and S. B. Roy, Phys. Rev. B **76**, 140401(R) (2007).
[16] R. Street and S. D. Brown, J. Appl. Phys. **76**, 6386 (1994).
[17] W. Eerenstein, N. D. Mathur, and J. F. Scott, Nature (London) **442**, 759 (2006).
[18] C. Pfleiderer, M. Uhlarz, S. M. Hayden, R. Vollmer, H. v. Löhneysen, N. R. Bernhoeft, and G. G. Lonzarich, Nature (London) **412**, 58 (2001).
[19] Y. Tokura, H. Kuwahara, Y. Moritomo, Y. Tomioka, and A. Asamitsu, Phys. Rev. Lett. **76**, 3184 (1996).
[20] H. Kuwahara, Y. Moritomo, Y. Tomioka, A. Asamitsu, M. Kasai, R. Kumai, and Y. Tokura, Phys. Rev. B **56**, 9386 (1997).
[21] R. Rawat, K. Mukherjee, Kranti Kumar, A. Banerjee, and P. Chaddah, J. Phys.: Condens. Matter **19**, 256211 (2007).
[22] J. A. Mydosh, *Spin Glasses: An Experimental Introduction* (Taylor & Francis, London, 1993), p. 69.
[23] S. Aksoy, T. Krenke, M. Acet, and E. F. Wassermann, Appl. Phys. Lett. **91**, 251915 (2007).
[24] P. Chaikin and T. Lubensky, *Principles of Condensed Matter Physics* (Cambridge University Press, Cambridge, 1995).
[25] S. Chatterjee, S. Giri, S. Majumdar, A. K. Deb, S. K. De, and V. Hardy, J. Phys.: Condens. Matter **19**, 346213 (2007).
[26] E. M. Levin, K. A. Gschneidner, Jr., and V. K. Pecharsky, Phys. Rev. B **65**, 214427 (2002).
[27] E. Gratz and A. S. Markosyan, J. Phys.: Condens. Matter **13**, R385 (2001).
[28] R. Mahendiran, A. Maignan, S. Hébert, C. Martin, M. Hervieu, B. Raveau, J. F. Mitchell, and P. Schiffer, Phys. Rev. Lett. **89**, 286602 (2002).
[29] Y. Imry, J. Phys. C **8**, 567 (1975).
[30] P. J. Brown, A. P. Gandy, K. Ishida, R. Kainuma, T. Kanomata, K. U. Neumann, K. Oikawa, B. Ouladdiaf, and K. R. A. Ziebeck, J. Phys.: Condens. Matter **18**, 2249 (2006).

Influence of the strong magnetocrystalline anisotropy on the magnetocaloric properties of MnP single crystal

M. S. Reis*
CICECO, Universidade de Aveiro, 3810-193 Aveiro, Portugal

R. M. Rubinger
Departamento de Física and I3N, Universidade de Aveiro, 3810-193 Aveiro, Portugal and DFQ-UNIFEI, 37500-000 Itajubá, Brazil

N. A. Sobolev and M. A. Valente
Departamento de Física and I3N, Universidade de Aveiro, 3810-193 Aveiro, Portugal

K. Yamada
Institute for Materials Research, Tohoku University, 980-8577 Sendai, Japan

K. Sato
Institute of Symbiotic Science and Technology, TUAT, 184-8588 Tokyo, Japan

Y. Todate
Physics Department, Faculty of Science, Ochanomizu University, 2-1-1 Ohtsuka, Bunkyo-ku, Tokyo 112-8610, Japan

A. Bouravleuv
Institute of Symbiotic Science and Technology, TUAT, 184-8588 Tokyo, Japan and A.F. Ioffe Physico-Technical Institute, 194021 St. Petersburg, Russia

P. J. von Ranke
Instituto de Física, Universidade do Estado do Rio de Janeiro-UERJ, Rua Sao Francisco Xavier, 524, 20550-013, Rio de Janeiro, Brazil

S. Gama
Instituto de Física "Gleb Wataghin," Universidade Estadual de Campinas (UNICAMP), Caixa Postal 6165, Campinas 13, 083-970 São Paulo-SP, Brazil

(Received 8 November 2007; published 27 March 2008)

Manganese monophosphate MnP single crystal deserves attention due to its rich magnetic phase diagram, which is quite different depending on the direction of the applied magnetic field. Generally speaking, it has a Curie temperature around 291 K and several other magnetic arrangements at low temperatures (cone-, screw-, fan-, and ferromagnetic-type structures). This richness is due to the strong magnetocrystalline anisotropy. In this sense, the present paper makes a thorough description of the influence of this anisotropy on the magnetocaloric properties of this material. From a fundamental view we could point out, among those several magnetic arrangements, the most stable one. On the other hand, from an applied view, we could show that the magnetic entropy change around room temperature ranges from −4.7 to −3.2 J/kg K, when the magnetic field (5 T) is applied along the easy and hard magnetization directions, respectively. In addition, we have shown that it is also possible to take advantage of the magnetic anisotropy for magnetocaloric applications, i.e., we have found a quite flat magnetic entropy change (with a huge relative cooling power), at a fixed value of magnetic field, only rotating the crystal by 90°.

DOI: 10.1103/PhysRevB.77.104439 PACS number(s): 75.30.Sg, 75.30.Gw

I. INTRODUCTION

Magnetic refrigeration is a promising technology and therefore the attention of researchers to this subject is increasing in a fast pace. This technology, based on the magnetocaloric effect (discovered in 1881 by Warburg[1]), is of easy understanding: application of a magnetic field to a magnetic material, under adiabatic conditions, makes the temperature of such material to increase. On the other hand, under isothermal conditions (when the magnetic material is in thermal contact with a thermal reservoir), application of a magnetic field induces a heat exchange between the material and the reservoir. From these two processes it is possible to create a thermomagnetic cycle and thus a magnetocaloric device, such as air-conditioners, refrigerators, and more.

The physical quantities that measure the magnetocaloric potential are the magnetic entropy change ΔS and adiabatic temperature change ΔT. The magnetic entropy change is more common to be found in the literature, since we only need to know the magnetization map, i.e., $M(H,T)$, around the Curie temperature of the material. In addition to the quite

often use of the magnetic entropy change to characterize the magnetocaloric potential of materials, it is also used to understand the fundamental physical properties of the material.[2]

From the applied view, a lot of families of materials have been studied by the scientific community, which makes a great effort to find a good material for magnetocaloric application, i.e., a material of low cost, good thermal conductivity, low electrical resistivity, strong magnetocaloric effect (MCE), etc. We can cite some families: La-Fe-Si,[3,4] Gd-Si-Ge,[5–7] intermetallics,[8–11] and, mainly, the Mn-based materials, such as manganites,[2,12,13] shape memory alloys Ni_2MnGa,[14,15] MnFe(P,As),[16] and MnAs (Refs. 17–20) (it is also interesting to cite the 1950s pioneer work of Fakidov and Krasovskii[21] on the MCE of MnP polycrystal around room temperature). Concerning the MnAs compound, recently, some Brazilian groups published a series of papers presenting the colossal magnetic entropy change of this material.[17–20] At ambient pressure this material has 40 J/kg K at 318 K at 5 T, increasing up to 267 J/kg K at 280 K at 5 T at 2.2 kbar.[19] Small iron substitution on the Mn site, i.e., $Mn_{1-x}Fe_xAs$, induced a chemical pressure and therefore 320 J/kg K was obtained at 310 K, 5 T and ambient external pressure.[18] On the other hand, anisotropic magnetocaloric effect has also been extensively studied by several groups,[22–26] being a quite actual issue within the magnetocaloric research, since it fits applied and fundamental aspects.

In this sense, the MnP single crystal deserves attention due to two features: it belongs to the parent MnAs family and also has a strong magnetocrystalline anisotropy. Thus, the present paper has two branched ideas: from one side, we propose to take advantage of the strong magnetocrystalline anisotropy for magnetocaloric applications; and from the other side, we have used the magnetic entropy change to understand the fundamentals of the rich magnetic phase diagram that arises for this single crystal, also due to the magnetocrystalline anisotropy.

II. MnP PHASE DIAGRAM

MnP has an orthorhombic structure (a=5.92 Å, b=5.26 Å, c=3.17 Å),[27] belongs to the *Pnam* space group (62) and, in this paper, we define $a>b>c$. The phase diagram of MnP single crystal was already described in some papers.[27–32] The character of the magnetic phases, both in zero and nonzero magnetic fields, is influenced by the orthorhombic magnetocrystalline anisotropy. Below, we make a complete description of the phase diagram, drawn in Fig. 1, with the magnetic field applied to the three main directions of the crystal.

Magnetic field parallel to c axis (⟨001⟩)-easy axis. For low values of magnetic field, decreasing temperature, MnP becomes ferromagnetic (FM) at T_C=291 K, with its magnetic moment along this c (easy) axis. Further cooling leads to a first order transition at T_s=47 K, from FM to a screw (SCR) structure. In this SCR phase, the Mn magnetic moments are confined within the bc plane, perpendicular to the a axis. At 4 K a full rotation is completed roughly each 9a.[30]

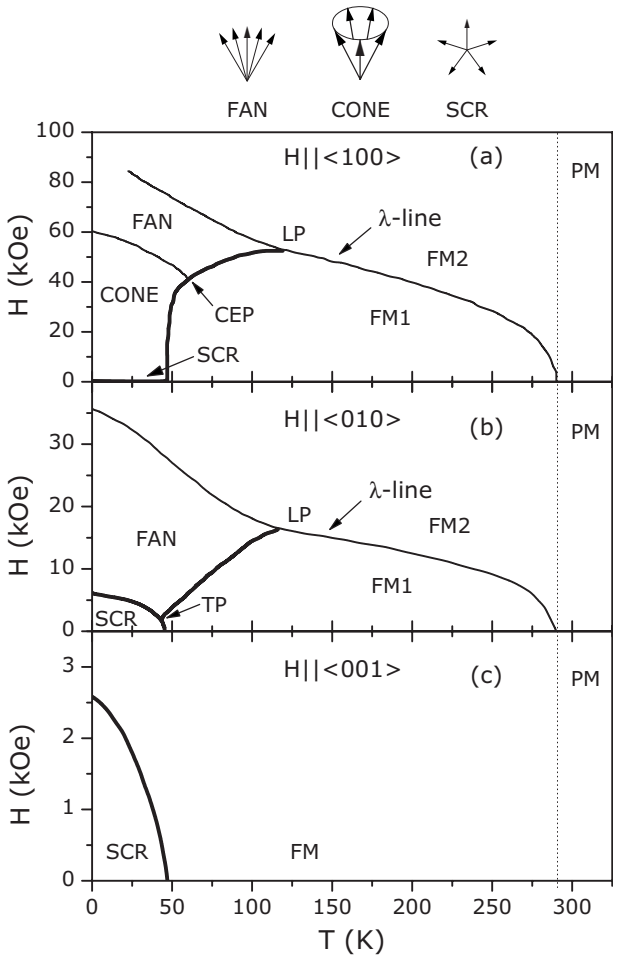

FIG. 1. Magnetic phase diagram of the MnP single crystal [after Zieba *et al.* (Ref. 32)]. These three panels correspond to the magnetic field applied along the three main directions of the crystal (⟨100⟩, ⟨010⟩, and ⟨001⟩). These labels have the following meaning: PM—paramagnetic phase, SCR—screw phase, FM1—magnetic moment along the ⟨001⟩ easy direction, FM2—magnetic moment along the applied magnetic field, CEP—critical end point, TP—triple point, and LP—Lifshitz point. The thick and thin lines represent, respectively, first and second order transitions.

At low temperatures (<47 K), increasing magnetic field, SCR phase changes back to the FM phase. This change in arrangement has a first order character. Figure 1(c) illustrates this phase diagram.

Magnetic field parallel to b axis (⟨010⟩)-intermediate axis. For low values of magnetic field, decreasing temperature, MnP also becomes ferromagnetic (FM1) at T_C=291 K, with its magnetic moment aligned along the c (easy) axis. Further cooling leads to a first order transition at T_s=47 K, from FM1 to the SCR structure. At low temperatures (<47 K), increasing magnetic field, SCR phase changes to FAN structure (first order transition). The difference with the SCR phase is that here (FAN), the magnetic moment does not perform a full rotation in the bc plane as we move along the a direction, but instead it oscillates about the b axis like a *fan*. Let us remember that in this case the magnetic field is applied along the ⟨010⟩ direction (b axis). Further increase of the magnetic field leads the system to a fully polarized ar-

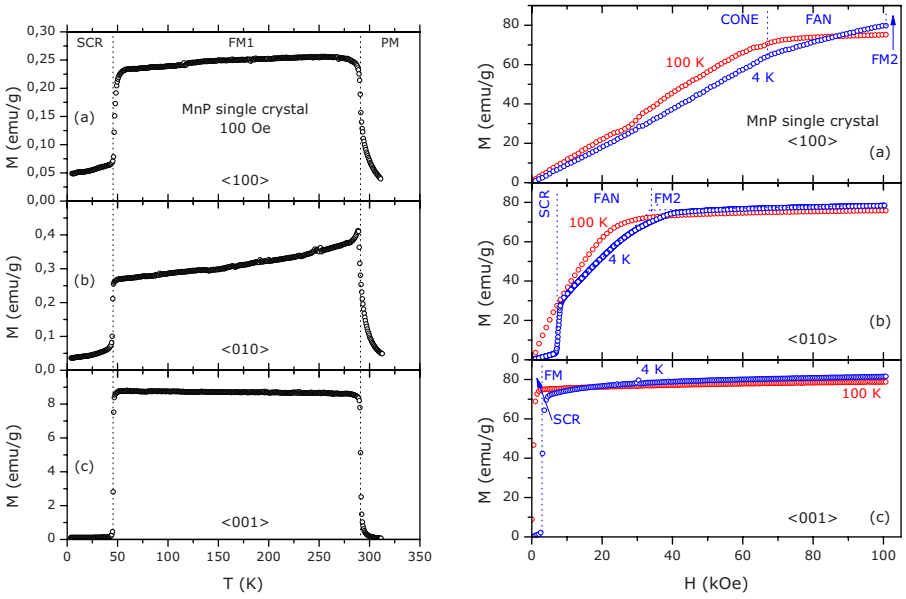

FIG. 2. (Color online) Magnetization as a function of temperature (left panels), and magnetic field (right panels). The magnetic field is applied along the three main crystallographic axes: (a) ⟨100⟩-hard, (b) ⟨010⟩-intermediate, and (c) ⟨001⟩-easy directions. See Sec. II and Fig. 1 for details concerning the labels.

rangement (FM2) along the b axis (second order transition). Between 47 K and the Lifshitz point (LP) at 121 K,[27,30,31] upon increasing the magnetic field, the system has a first order transition from the FM1 phase to the FAN phase and then to the FM2 phase. This line above which the magnetic moments are aligned along the magnetic field (i.e., FM2 phase) is called λ line.[27,30,31] For temperatures above LP it has a second order transition form the FM1 to FM2. To complete the description of this phase diagram, there is a triple point (TP), where the SCR, FAN, and FM1 phases merge. Figure 1(b) illustrates these transitions.

Magnetic field parallel to a axis (⟨100⟩)-hard axis. For low values of magnetic field, decreasing temperature, MnP also becomes ferromagnetic (FM1) at T_C=291 K, with its magnetic moment aligned along the c (easy) axis. Further cooling leads to a first order transition at T_s=47 K, from FM1 to the SCR structure. At low temperatures (<47 K), increasing magnetic field, SCR phase changes to a CONE phase, quite similar to the SCR phase; however, with a component along the a axis. Remember that, in this case, the magnetic field is applied along the ⟨100⟩ axis (a axis). Still increasing the magnetic field, the system changes to a FAN phase, oscillating about the a axis. Then, at high values of magnetic field, the system becomes fully polarized (FM2) along the a axis. This phase diagram is richer than the previous one (⟨010⟩ axis), and from 47 K up to the critical end point (CEP),[27,30,31] upon increasing magnetic field, the system has the same arrangements than before (<47 K); however, the ground state is FM1. Between CEP and LP the system changes from FM1 to FAN (first order transition) and then to FM2 (second order transition). For temperatures above LP, MnP has a second order transition, from FM1 to FM2. Details are given in Fig. 1(a).

III. EXPERIMENTAL DETAILS

Powders of manganese and phosphorus were sealed in an evacuated quartz double tube. The mixture was heated slowly (~40 °C/day) and kept 3 days at 900 °C. The reacted powder was melted at 1210 °C and the single crystal was grown by the Bridgman method at 1190 °C from this reaction product. The melting point of MnP is 1140 °C. The single crystal was further purified by the zone refining technique in a horizontal traveling furnace. The surface of the crystal was etched by nitric acid diluted with ethanol. The orientation of the crystal was determined by the x-ray Laue method. It has been confirmed by several neutron diffraction experiments that the mosaic spread of the crystal is quite small (less than 0.1°). Details of the sample preparation can be found in Ref. 33. Magnetization was measured in a vibrating sample magnetometer (VSM) magnetometer at the University of Aveiro, Portugal.

The sample is a cuboid with sides: a=1.50 mm, b=2.07 mm, and c=6.29 mm. The corresponding demagnetization factors (in SI units) are easy to obtain from Ref. 34: N_a=0.506, N_b=0.375, and N_c=0.119. From the results presented in this paper it is possible to estimate the demagnetization field. Let us consider, for instance, the highest demagnetization factor, i.e., that along the a axis. Thus, in this case, for 4 K and 10 T the demagnetization field is only 0.2 T and, consequently, the true magnetic field is 9.8 T.

IV. MAGNETIZATION MEASUREMENTS

As described before, our objective is to understand and describe the influence of the strong magnetocrystalline anisotropy on the magnetocaloric properties of MnP single crystal. We need to know the complete magnetization map, i.e., $M(T,H)$ to obtain the magnetic entropy change ΔS (a usual quantity to measure the magnetocaloric potential of materials), and it is done through the equation

$$\Delta S = \int_{H_i}^{H_f} \left(\frac{\partial M}{\partial T} \right)_H dH. \quad (1)$$

It is important to underline a minor point. The first order transitions present in this material have no hysteresis and

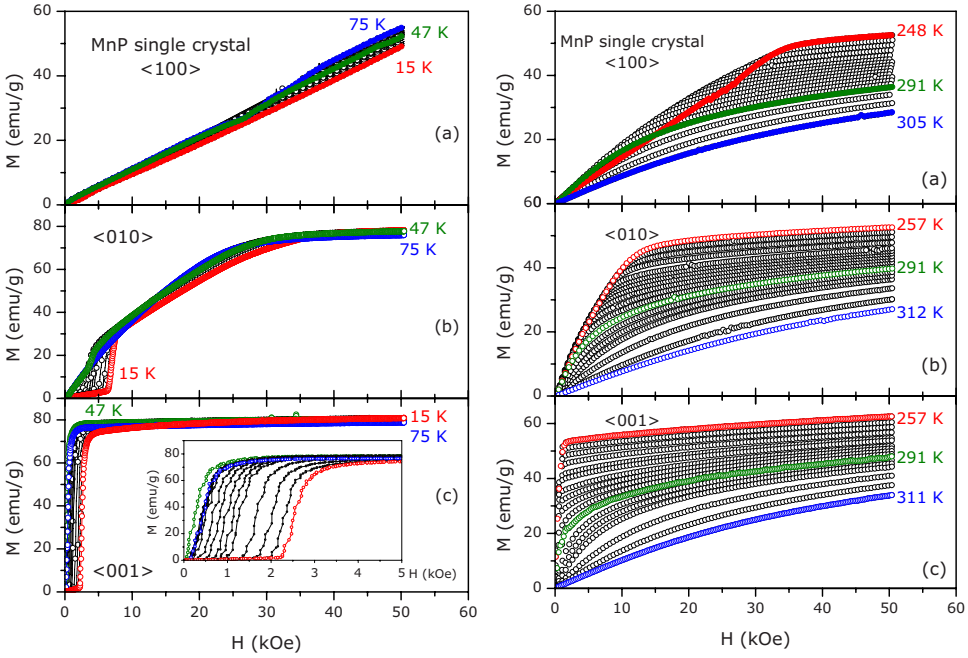

FIG. 3. (Color online) Magnetization as a function of magnetic field, applied along (a) ⟨100⟩, (b) ⟨010⟩, and (c) ⟨001⟩ directions. (left panels) These curves were taken at several temperatures around T_s=47 K, where the ground state changes from FM1 phase to SCR phase. (right panels) These curves were taken at several temperatures around T_c =291 K, where the ground state changes from PM phase to FM1 phase. See colored figures for clearness.

therefore we can consider that the equilibrium dynamics are faster than the measuring time. Thus, the system is in equilibrium and the Maxwell relation is valid.[35] When it is not the case, special care must be addressed.[36,37]

Thus, we first measured the magnetization as a function of temperature, with a low magnetic field (100 Oe), applied along the three main directions of the crystal: ⟨100⟩, ⟨010⟩, and ⟨001⟩. This result is presented in Fig. 2 (left panels) and shows two clear transitions, as described in the phase diagram (Sec. II). The first, at T_C=291 K, occurs from the paramagnetic phase (PM) to the ferromagnetic (FM1) phase, where the Mn moments are aligned along the *c*-easy axis, and the second transition, at T_s=47 K, occurs from the FM1 phase to the SCR phase. A minor point to clarify the labels: FM1 corresponds to the magnetic moment along ⟨001⟩ easy axis, whereas FM2 represents the magnetic moment along the applied field. Since these two cases are the same when $H \| \langle 001 \rangle$, we generally call this ferromagnetic phase as FM [see Fig. 1(c), for instance].

Figure 2 (right panels) is a clear example of the strong magnetocrystalline anisotropy in MnP single crystal and shows the magnetization as a function of magnetic field (up to 100 kOe) at 4 and 100 K, for those three crystallographic axes. We emphasize the agreement with the phase diagram described in Sec. II. The curves at 100 K do not have the phase changes as evident as those at 4 K.

As mentioned before, to obtain the magnetic entropy change we need to measure $M(T,H)$ around the magnetic transition. Thus, we measured those curves around T_s =47 K [Fig. 3 (left panels)] and T_C=291 K [Fig. 3 (right panels)], for those three main crystallographic axes. To clarify and confirm that phase diagram presented in Fig. 1, we show in Fig. 4 the magnetization as a function of temperature for several values of applied magnetic field, obtained by a treatment of those data of Fig. 3.

V. MAGNETIC ENTROPY CHANGE

From those data presented in the previous section and using Eq. (1) it is possible to determine the magnetic entropy change. Below we will discuss the behavior of this quantity when the magnetic field is applied along those three directions. The vertical dotted lines that appear in the figures of this section limit temperature ranges where there is a change in the magnetic arrangement due to the applied field. For instance, SCR→CONE means that the system, under a certain value of applied field, changed its magnetic arrangement from SCR to CONE phases.

A. Low temperature contribution

MCE of $H \| \langle 100 \rangle$: Around T_s=47 K there are five magnetic arrangements, namely, SCR, CONE, FAN, FM1, and FM2 (see Sec. II). Below 47 K we found a positive magnetic entropy change, where the system changes its arrangement from SCR to CONE [see Fig. 5(a)]. From this fact we can conclude that the SCR phase has a smaller magnetic entropy and is therefore more stable than the CONE phase. Around 47 K and for magnetic fields higher than 20 kOe there is a quite narrow range of temperatures where the FAN phase arises (between the CONE and FM1 phases—this behavior is a bit different than that presented in Fig. 1). See Fig. 4(a) for details. Due to the quite narrow temperature range, it is difficult to determine the magnetic arrangement from only magnetic measurements; however, the most probable arrangement, following the phase diagram of Fig. 1, is the FAN phase. We found therefore a deep minimum in the magnetic entropy curve [Fig. 5(a)—top]; in other words, a negative ΔS when the arrangement changes from SCR to FAN. This behavior is no more observed for $\Delta H < 20$ kOe [see Fig. 5(a)—bottom].

MCE of $H \| \langle 010 \rangle$: As described in Sec. II, increasing magnetic field, there are four magnetic arrangements around

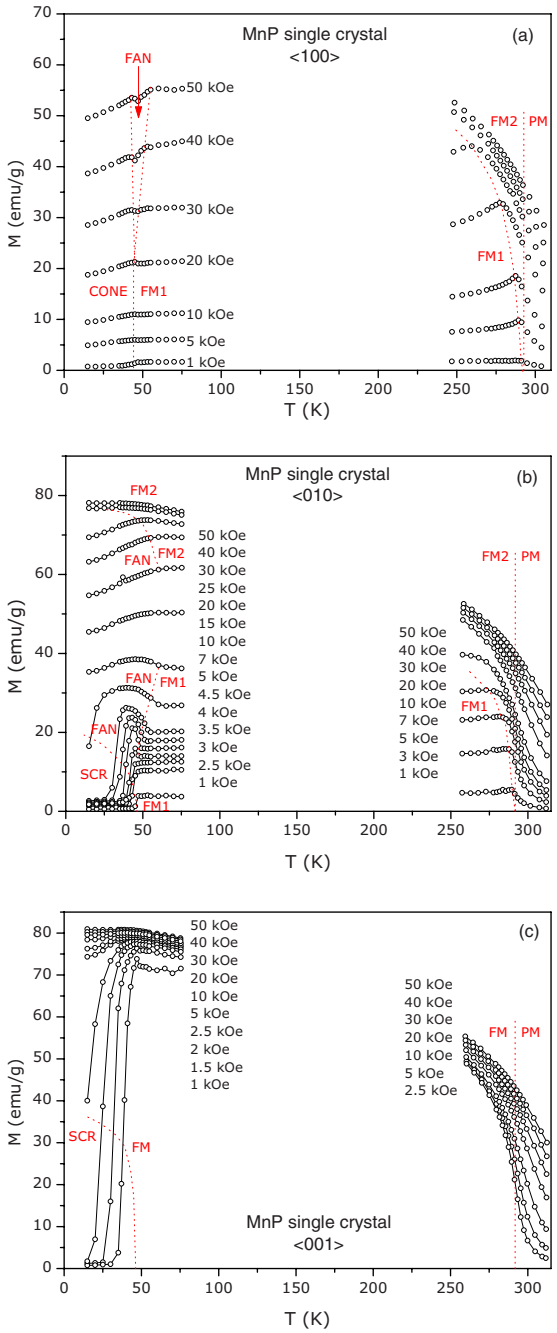

FIG. 4. (Color online) Magnetization as a function of temperature for several values of applied magnetic field along (a) ⟨100⟩, (b) ⟨010⟩, and (c) ⟨001⟩ directions. These curves were determined from Fig. 3. See Sec. II for the meaning of the labels.

T_s=47 K, namely, SCR, FAN, FM1, and FM2. Below 47 K, we found a positive magnetic entropy change when the system changes its arrangement from SCR to FM2 and FAN phases [see Fig. 5(b)]. We conclude from this fact that the SCR phase has a magnetic entropy smaller than the FM2 and FAN phases and, consequently, is more stable. This fact is confirmed by the zero magnetic entropy change for magnetic field changes within the SCR phase [$\Delta H \lesssim 5$ kOe, namely, 5 kOe (blue curve) and 1 kOe (red curve) see Fig. 5(b)—bottom]; i.e., this phase is stable enough that those values of magnetic field are not able to change the entropy of that phase (SCR).

A different scenario arises above 47 K, where the magnetic entropy change is negative. Here, the magnetic entropy of the FM1 phase is bigger than the FM2 and FAN phases; and is, consequently, less stable than the FM2 and FAN arrangements. Figure 5(b)—top clarifies the above discussion, for magnetic field change from zero up to above the λ line. Figure 5(b)—bottom also sketches those words, however, for intermediate values of magnetic field change.

MCE of $H\|\langle 001\rangle$: In a similar fashion as described before, for temperatures below 47 K the magnetic entropy change is positive, indicating that the SCR phase is more stable than the FM phase. We remember that in this case FM=FM1=FM2, since the magnetic moment is aligned along the ⟨001⟩ directions (FM1) and also along the magnetic field (FM2); thus, we generally call this phase as FM. Again, the magnetic field change within the SCR phase is not able to change the entropy of this phase and, consequently, the corresponding magnetic entropy change is zero. Above 47 K, the magnetic entropy change becomes negative, indicating, in this case with only one arrangement above 47 K (FM), the usual behavior of increasing entropy by decreasing magnetic field. Details are sketched in Fig. 5(c).

B. High temperature contribution

MCE of $H\|\langle 100\rangle$: As shown in Fig. 6, the magnetic entropy change above the Curie temperature T_C=291 K, i.e., in the paramagnetic phase, is negative, as expected. Below T_C in a limited temperature range (from FM1 to FM2), the magnetic entropy change is also negative; and shows that the FM1 phase has a bigger magnetic entropy than the FM2 phase. Thus, FM2 is more stable than the FM1 phase.

On the other hand, the magnetic entropy change becomes positive when the magnetic field change is not enough to cross the λ line, i.e., the arrangement does not change and remains within the FM1 phase. It means that magnetic entropy of the FM1 phase under applied magnetic field (below the λ line) is bigger than the magnetic entropy with a lower value of magnetic field (or even a zero magnetic field). Consequently, we conclude that the FM1 phase without magnetic field is more stable than the same phase with applied magnetic field (below the λ line). This conclusion is reasonable, because the strong magnetocrystalline anisotropy tends to align the magnetic moment along ⟨001⟩ direction (FM1), and this situation has a lower entropy than the "perturbed" case where the spins are submitted to a magnetic field (below the λ line) along the ⟨100⟩ direction. Figure 6(a) clarifies this scenario. Note that these positive values agree with the same measurement at low temperatures [see Fig. 5(a)].

MCE of $H\|\langle 010\rangle$: In a similar fashion as before, the magnetic entropy change (a) within the paramagnetic phase and (b) between the FM1 and FM2 phases are both negatives, as expected. In addition, the magnetic entropy change is (almost) zero changing the arrangement within the FM1 phase. It means that applying the magnetic field (below the λ line) along the ⟨010⟩ direction does not change the entropy of the system (different from the ⟨100⟩ case, where the entropy evi-

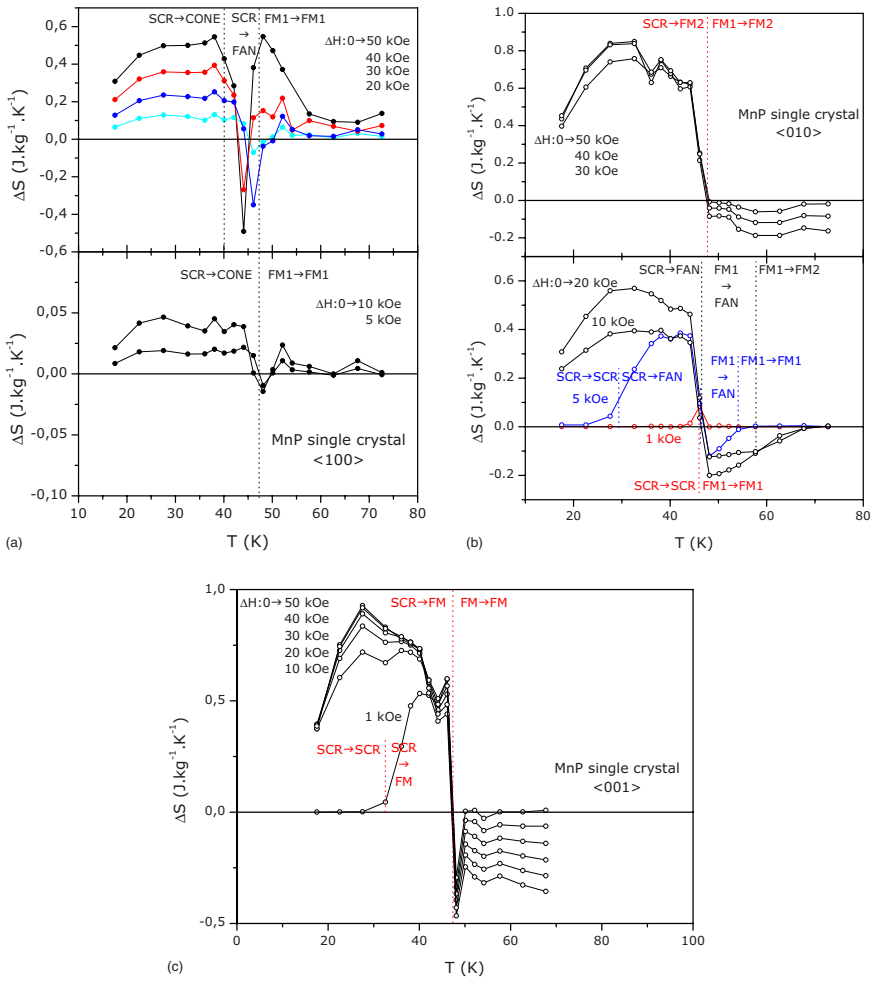

FIG. 5. (Color online) Magnetic entropy change as a function of temperature (around T_s=47 K), when the magnetic field is applied along the (a) ⟨100⟩, (b) ⟨010⟩, and (c) ⟨001⟩ directions. The vertical dotted lines limit temperature ranges where the magnetic arrangement changes due to the applied field. See colored figures for clearness.

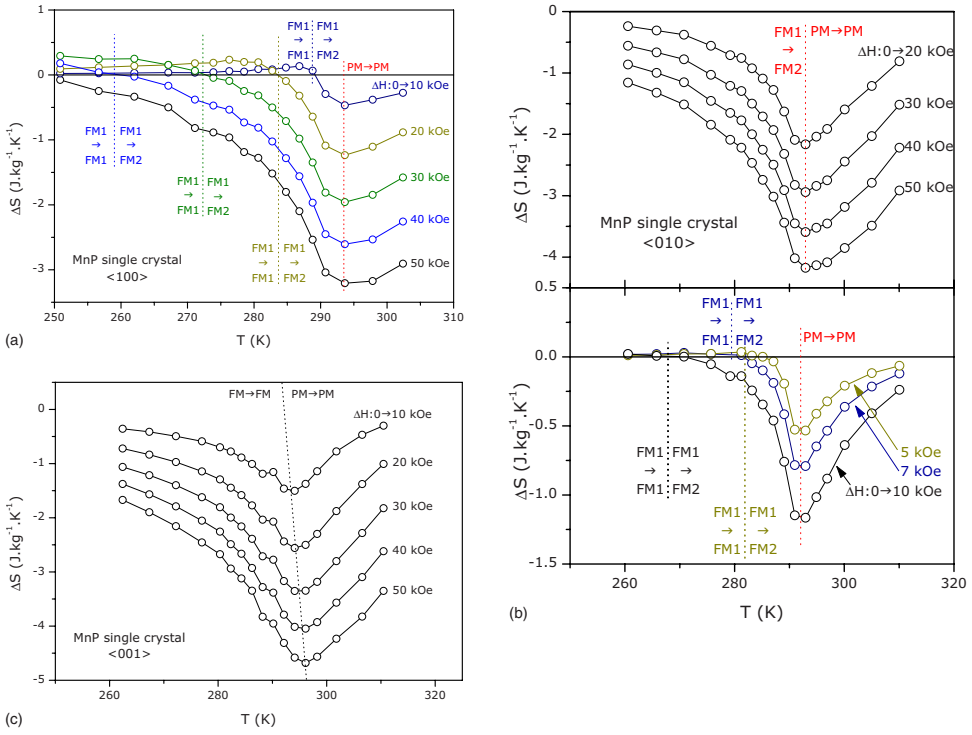

FIG. 6. (Color online) Magnetic entropy change as a function of temperature (around T_C =291 K), when the magnetic field is applied along the (a) ⟨100⟩, (b) ⟨010⟩, and (c) ⟨001⟩ directions. The vertical dotted lines limit temperature ranges where the magnetic arrangement changes due to the applied field. See colored figures for clearness/

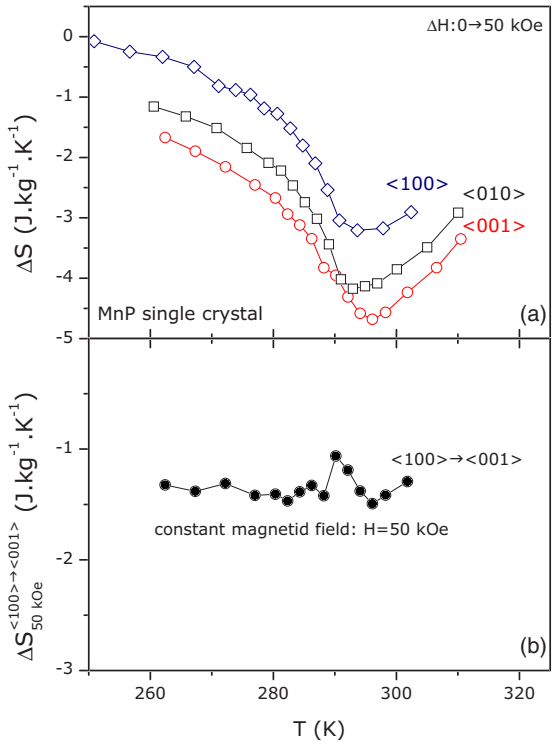

FIG. 7. (Color online) (a) Magnetic entropy change for 50 kOe of magnetic field change applied along the three main crystallographic axes ⟨100⟩, ⟨010⟩, and ⟨001⟩. This difference is therefore due to the strong magnetic anisotropy present in this MnP single crystal. (b) Magnetic entropy change for a fixed magnetic field (50 kOe), just rotating the crystal, from the hard (⟨100⟩) to the easy (⟨001⟩) direction. In other words, it is the magnetic entropy change due to the anisotropy.

dently increases). See Fig. 6(b) for clearness.

MCE of $H\|\langle 001\rangle$: It is the simplest case and has a usual magnetic entropy change curve, without changes in the magnetic arrangement by changing the magnetic field. Figure 6(c) presents these results.

VI. ADVANTAGES OF THE MAGNETOCRYSTALLINE ANISOTROPY FOR MAGNETOCALORIC APPLICATIONS

In this section we analyze the advantages of the magnetic anisotropy for magnetocaloric applications around the Curie temperature (T_C=291 K), which is close to room temperature (RT). It is expected, due to the anisotropy, that the magnetic entropy change measured with the magnetic field applied along the hard direction be smaller than that along the easy direction, and indeed it is [see Fig. 7(a)]. We can note that there is 1.5 J/kg K (at 50 kOe) of entropy change between those curves (around T_C) and this energy can be achieved only rotating the crystal, from the hard to the easy direction under a fixed value of magnetic field. The magnetic entropy change due to this rotation is equal to the difference of entropy change due to the applied field along those hard and easy directions as follows:

$$\Delta S_{50\ \mathrm{kOe}}^{\langle 100\rangle\rightarrow\langle 001\rangle} = \Delta S^{\langle 001\rangle} - \Delta S^{\langle 100\rangle} = S_{50\ \mathrm{kOe}}^{\langle 001\rangle} - S_{0\ \mathrm{kOe}}^{\langle 001\rangle} - (S_{50\ \mathrm{kOe}}^{\langle 100\rangle} - S_{0\ \mathrm{kOe}}^{\langle 100\rangle}) = S_{50\ \mathrm{kOe}}^{\langle 001\rangle} - S_{50\ \mathrm{kOe}}^{\langle 100\rangle}. \quad (2)$$

Considering, of course, that the zero field entropy is isotropic, i.e., $S_{0\ \mathrm{kOe}}^{\langle 001\rangle}=S_{0\ \mathrm{kOe}}^{\langle 001\rangle}=S_{0\ \mathrm{kOe}}$. Figure 7(b) presents therefore $\Delta S_{50\ \mathrm{kOe}}^{\langle 100\rangle\rightarrow\langle 001\rangle}$. We should emphasize the quite flat profile of the magnetic entropy change upon rotating the crystal. In spite of low absolute value of magnetic entropy change, it has a giant relative cooling power[38] due to the huge width at half maximum.

VII. FINAL REMARKS

The present paper has two branched ideas: from one side, we used the magnetic entropy change to understand the rich phase diagram of MnP single crystal, with several magnetic arrangements due to the strong magnetocrystalline anisotropy. We could discuss therefore which magnetic phase is more stable. From the other side, after Refs. 24 and 25, we could generally propose how to take advantage of the anisotropy for magnetocaloric applications: we could obtain a quite flat magnetic entropy change around the Curie temperature of the system (~291 K) at a constant magnetic field, only rotating the crystal. This flat ΔS is an advantage of the anisotropy, since a magnetic refrigerator based on this idea does not need to move permanent magnets, but only rotate a single crystal refrigerant material by 90° under a constant magnetic field.

ACKNOWLEDGMENT

M.S.R. thanks FCT for the project POCI/CTM/61284/2004. The authors thank (i) FCT for the VSM equipment (REEQ/1126/2001) and (ii) Sérgio Pereira for the orientation of the sample. R.M.R. also thanks FCT for the grant (SFRH/BPD/34541/2007).

*marior@ua.pt

[1] E. Warburg, Ann. Phys. **13**, 141 (1881).
[2] M. S. Reis, V. S. Amaral, J. P. Araújo, P. B. Tavares, A. M. Gomes, and I. S. Oliveira, Phys. Rev. B **71**, 144413 (2005).
[3] A. Fujita, S. Fujieda, Y. Hasegawa, and K. Fukamichi, Phys. Rev. B **67**, 104416 (2003).
[4] A. Fujita, S. Fujieda, K. Fukamichi, H. Mitamura, and T. Goto, Phys. Rev. B **65**, 014410 (2001).
[5] V. K. Pecharsky and K. A. Gschneidner, Jr., Phys. Rev. Lett. **78**, 4494 (1997).
[6] W. Choe, V. K. Pecharsky, A. O. Pecharsky, K. A. Gschneidner, V. G. Young, and G. J. Miller, Phys. Rev. Lett. **84**, 4617 (2000).
[7] V. K. Pecharsky, A. P. Holm, K. A. Gschneidner, and R. Rink, Phys. Rev. Lett. **91**, 197204 (2003).

[8] D. Wang, H. Liu, S. Tang, S. Yang, S. Huang, and Y. Du, Phys. Lett. A **297**, 247 (2002).
[9] N. A. de Oliveira, P. J. von Ranke, and A. Troper, Phys. Rev. B **69**, 064421 (2004).
[10] P. J. von Ranke, E. P. Nóbrega, I. G. de Oliveira, A. M. Gomes, and R. S. Sarthour, Phys. Rev. B **63**, 184406 (2001).
[11] A. Gomes, M. Reis, I. Oliveira, A. Guimaraes, and A. Takeuchi, J. Magn. Magn. Mater. **242**, 870 (2002).
[12] D. Morelli, A. Mance, J. Mantese, and A. Micheli, J. Appl. Phys. **79**, 373 (1996).
[13] H. Chen, C. Lin, and D. Dai, J. Magn. Magn. Mater. **257**, 254 (2003).
[14] F. Xia Hu, B. Gen Shen, and J. Rong Sun, Appl. Phys. Lett. **76**, 3460 (2000).
[15] X. Zhou, W. Li, H. Kunkel, and G. Williams, J. Phys.: Condens. Matter **16**, L39 (2004).
[16] O. Tegus, E. Brück, L. Zhang, Dagula, K. Buschow, and F. de-Boer, Physica B **319**, 174 (2002).
[17] D. Rocco, A. Campos, A. Carvalho, L. Caron, P. von Ranke, and N. Oliveira, Appl. Phys. Lett. **90**, 242507 (2007).
[18] A. Campos, D. Rocco, A. Carvalho, L. Caron, A. Coelho, S. Gama, L. Silva, F. Gandra, A. Santos, L. Cardoso, P. J. Von Ranke, and N. A. Oliveira, Nat. Mater. **5**, 802 (2006).
[19] S. Gama, A. A. Coelho, A. de Campos, A. M. Carvalho, F. C. G. Gandra, P. J. von Ranke, and N. A. de Oliveira, Phys. Rev. Lett. **93**, 237202 (2004).
[20] P. J. von Ranke, S. Gama, A. A. Coelho, A. Campos, A. M. Carvalho, F. C. G. Gandra, and N. A. de Oliveira, Phys. Rev. B **73**, 014415 (2006).
[21] I. Fakidov and V. Krasovskii, Sov. Phys. JETP **9**, 755 (1959).
[22] M. Mihalik and V. Sechovsky, J. Magn. Magn. Mater. **310**, 1758 (2007).
[23] P. von Ranke, N. Oliveira, V. Sousa, D. Garcia, I. Oliveira, A. Carvalho, and S. Gama, J. Magn. Magn. Mater. **313**, 176 (2007).
[24] P. von Ranke, N. Oliveira, C. Mello, D. Garcia, V. Sousa, V. Souza, A. Caldas, and I. Oliveira, J. Alloys Compd. **440**, 46 (2007).
[25] M. Zou, Y. Mudryk, V. K. Pecharsky, K. A. Gschneidner, D. L. Schlagel, and T. A. Lograsso, Phys. Rev. B **75**, 024418 (2007).
[26] P. J. von Ranke, N. A. de Oliveira, D. C. Garcia, V. S. R. de Sousa, V. A. de Souza, A. M. Carvalho, S. Gama, and M. S. Reis, Phys. Rev. B **75**, 184420 (2007).
[27] C. C. Becerra, V. Bindilatti, and N. F. Oliveira, Phys. Rev. B **62**, 8965 (2000).
[28] E. E. Huber and D. H. Ridgley, Phys. Rev. **135**, A1033 (1964).
[29] T. Komatsubara, H. Shinohara, T. Suzuki, and E. Hirahara, J. Appl. Phys. **40**, 1037 (1969).
[30] C. C. Becerra, H. J. Brumatto, and N. F. Oliveira, Phys. Rev. B **54**, 15997 (1996).
[31] Y. Shapira, C. C. Becerra, N. F. Oliveira, and T. S. Chang, Phys. Rev. B **24**, 2780 (1981).
[32] A. Zieba, C. C. Becerra, H. Fjellvag, N. F. Oliveira, and A. Kjekshus, Phys. Rev. B **46**, 3380 (1992).
[33] Y. Todate, K. Yamada, Y. Endoh, and Y. Ishikawa, J. Phys. Soc. Jpn. **56**, 36 (1987).
[34] A. Aharoni, J. Appl. Phys. **83**, 3432 (1998).
[35] J. S. Amaral (private communication).
[36] A. Tishin and Y. Spichkin, *The Magnetocaloric Effect and its Applications* (Institute of Physics, Bristol, 2003).
[37] K. Gschneidner, V. Pecharskyand, and A. Tsokol, Rep. Prog. Phys. **68**, 1479 (2005).
[38] The relative cooling power is defined as the maximum value of the magnetic entropy change curve (i.e., ΔS_{max}) times the width of this curve at half maximum.

Metastability and magnetic memory effect in $Ni_2Mn_{1.4}Sn_{0.6}$

S. Chatterjee, S. Giri, and S. Majumdar*
Department of Solid State Physics, Indian Association for the Cultivation of Science, 2A & B Raja S. C. Mullick Road, Jadavpur, Kolkata 700 032, India

S. K. De
Department of Materials Science, Indian Association for the Cultivation of Science, 2A & B Raja S. C. Mullick Road, Jadavpur, Kolkata 700 032, India

(Received 26 October 2007; revised manuscript received 3 December 2007; published 16 January 2008)

Magnetostructural instability in the ferromagnetic shape memory alloy of composition $Ni_2Mn_{1.4}Sn_{0.6}$ is investigated by transport and magnetic measurements. Large negative magnetoresistance is observed around the martensitic transition temperature (90–210 K). Both magnetization and magnetoresistance data indicate that upon the application of an external magnetic field at a constant temperature, the sample attains a field-induced arrested state which persists even when the field is withdrawn. We observe an intriguing behavior of the arrested state that it can remember the last highest field it has experienced. The field-induced structural transition plays the key role for the observed anomaly and the observed irreversibility can be accounted for by the Landau-type free energy model for the first-order phase transition.

DOI: 10.1103/PhysRevB.77.012404 PACS number(s): 75.80.+q, 64.70.K−, 85.75.Bb

The functional behavior of the shape memory alloys as actuators, magnetomechanical transducers, and switching devices, is related to the structural instability known as martensitic transition (MT). It is defined as a displacive, diffusionless first-order solid to solid phase transition from the high temperature austenite to the low temperature martensite.[1] Ferromagnetic shape memory alloys (FSMAs) combine shape memory effect and the bulk ferromagnetic behavior. MT, being key to the shape memory and some other metallurgic phenomena, has been under extensive research for over a century. The first-order MT in Heusler based alloys, influenced by the disorder, often developed with a region of metastability with austenite and the martensite coexisting together.[2–4] MT is found to be highly sensitive to the external parameters such as stress and magnetic field, and magnetic field-induced strain,[5,6] superelasticity, magnetocaloric effect,[7,8] and giant magnetoresistance[9,10] have been reported for many FSMAs. Materials with general formula $Ni_2Mn_{1+z}X_{1-z}$ (where X is an sp element such as Sn, Sb, In, etc.) are found to be quite useful for possible multifunctional applications.

It is important to understand the effect of magnetic field on the electronic and magnetic behaviors of those FSMAs. This is not only essential for the technological applications but can also provide fundamental insight of the phase separated scenario. In order to address the issue, we have performed detailed study of the magnetotransport and magnetic properties of the alloy $Ni_2Mn_{1.4}Sn_{0.6}$, which has been reported to show ferromagnetic shape memory effect and inverse magnetocaloric effect. The sample orders ferromagnetically below 330 K and on cooling it undergoes MT from the cubic phase to orthorhombic phase around 180 K,[11] with a wide region of phase separation which extends from 90 to 210 K. Our study reveals large magnetoresistance (MR) around MT and unique magnetic behavior which go beyond the previous observations in the case of ferromagnetic shape memory alloys. The resistivity and the magnetization show a striking memory effect with respect to the applied magnetic field (H).

The present investigation was carried out on polycrystalline sample of $Ni_2Mn_{1.4}Sn_{0.6}$ prepared by argon arc melting. The sample was characterized by x-ray powder diffraction (XRD) and energy dispersive x-ray spectroscopy. The resistivity (ρ) of the sample was measured by the usual four point method. MR $\left[=\frac{\rho(H)-\rho(0)}{\rho(0)}\right]$ measurement was carried out using a superconducting magnet system in the transverse geometry ($H\perp$ current). Magnetization (M) was measured using a commercial vibrating sample magnetometer (Cryogenic Ltd., UK).

Figure 1(a) shows ρ versus temperature (T) behavior of the sample measured at $H=0$ and $H=50$ kOe for both heating and cooling cycles. The clear thermal hysteresis around the first-order MT is present for both zero field and 50 kOe runs. However, the MT is shifted to lower T in the presence of H. In the cooling run, the martensite develops between temperatures M_s and M_f, while austenite develops between A_s and A_f during heating. In the H-T phase diagram of the sample [inset of Fig. 1(a)], the white and black shadings, respectively, denote the region of phase coexistence for cooling and heating legs. The average estimated shift of M_s for 50 kOe of magnetic field is about 12 K. This produces large negative MR in the sample. Figure 1(b) shows the plot of MR at 50 kOe versus T for both heating and cooling legs. MR of about −16% is observed in the sample for the heating leg, while on the cooling leg, MR is found to be around −19%. It is clear that the large MR is only observed around the region of phase separation, which is approximately the region of thermal hysteresis. The apparent difference of the magnitude of MR in the heating and cooling is due to the difference in the austenite and martensite fractions in the sample.

In order to get a better look at the MR behavior, we measured ρ as a function of field at different constant T [Fig. 2(a)]. The magnitude of MR is very small at 15 K, where the

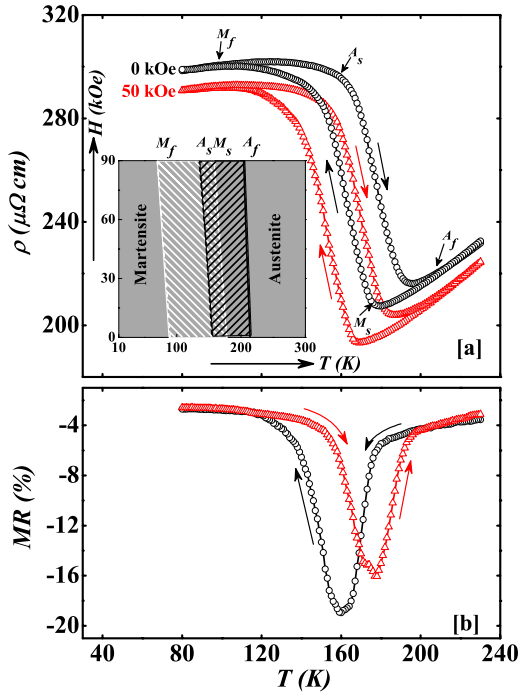

FIG. 1. (Color online) (a) Resistivity as a function of temperature for both heating and cooling cycles (indicated by arrows) at zero and 50 kOe of applied fields for $Ni_2Mn_{1.4}Sn_{0.6}$. The inset shows the *H*-*T* phase diagram of the sample, with shaded area being the region of phase coexistence. (b) Magnetoresistance (MR) as a function of temperature for heating and cooling cycles for 50 kOe of field.

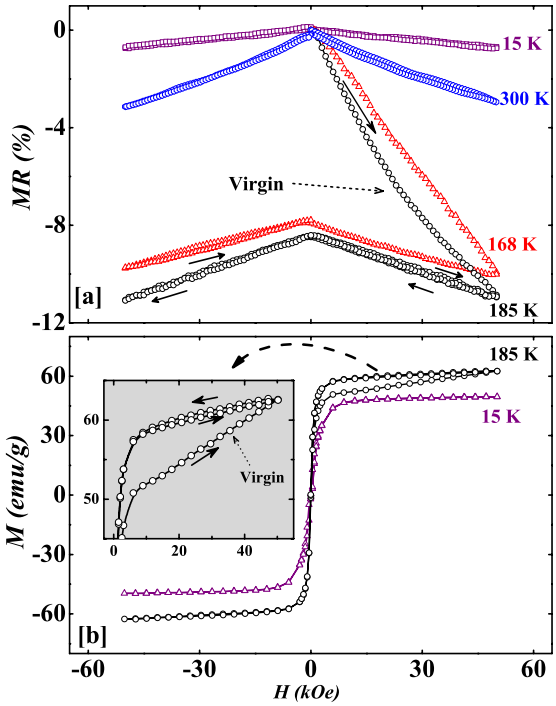

FIG. 2. (Color online) (a) Magnetoresistance and (b) magnetization as a function of field at different constant temperatures. The sample was first zero field cooled to 10 K and then heated back to the respective constant temperatures for MR and *M* measurements. The data were collected for change of the magnetic field in the positive and negative quadrants. The inset in (b) represents the enlarged view of the magnetization data at 185 K.

sample is in the pure martensite. However, larger negative MR is observed in the region of MT, which is in line with the $\rho(T)$ measurements performed at different fields. The interesting observation from the MR versus *H* data is that in the region of metastability, the MR is highly irreversible with respect to the applied magnetic field. The large change in ρ is observed when the field is applied first; however, sample almost retains its low ρ when the field is removed, and it persists for subsequent field cycling. This has been clearly depicted in Fig. 2(a) where five loop field cycling is performed. For example, in the case of 185 K isotherm, the initial application of 50 kOe of field (virgin leg) produces about −11% of MR, while in the subsequent field removal and application (even in the negative *H* quadrant) do not produce much effect on ρ, only a mere 2.5% change is observed. This type of field arrested state is only restricted across the MT and no indication of arrested state is observed above and below the MT [15 and 300 K, respectively, in Fig. 2(a)]. Notably, the MR does not show any signature of saturation until 90 kOe, and the arrested state can be created even at 90 kOe (not shown here).

In a ferromagnetic alloy, it is expected that the MR anomaly has some magnetic origin. To probe it, we measured isothermal *M* as a function of field at different constant temperatures. The initial magnetization leg (virgin leg: 0–50 kOe) at 185 K shows larger slope beyond the point of technical saturation as compared to the return leg. On subsequent field cycling, very similar to the MR behavior, *M* traces the return leg with almost zero coercivity. The virgin loop remains well outside (below) the subsequent field-cycling loops [see inset of Fig. 2(b)]. It appears that by the application of 50 kOe of field, the sample has been arrested to a state with a very soft ferromagnetic character. Similar field-induced arrested state is also reported for Ni-Mn-*X* based alloys.[6,10,15] For the present sample, we find that there is a threshold field of about 1 kOe for the production of this arrested state.

It is tempting to know the character of this field-induced arrested state and what happens to the resistivity if the temperature is varied after this state is achieved. For this purpose, we performed ρ measurement in the following protocol [see Fig. 3(a)]. The sample was first cooled in zero magnetic field from 240 to 80 K (point c to d in Fig. 3) and heated back to 180 K (point e). At this point, 50 kOe of field was applied, and ρ drops down to point f. Immediately, field was removed and the sample was allowed to heat up. ρ followed a completely different path (gh) and eventually joined up with the zero field heating curve at point h. It clearly depicts that the application and subsequent removal of *H* at a certain point inside the thermal hysteresis region produces a state which is different from the zero field state as far as the *T* dependence of resistivity is concerned. However, eventually it approaches the zero field virgin state.

The noteworthy observation is the magnetic memory effect as depicted in Fig. 4. We have seen that the sample goes to a different electronic and magnetic state on application of

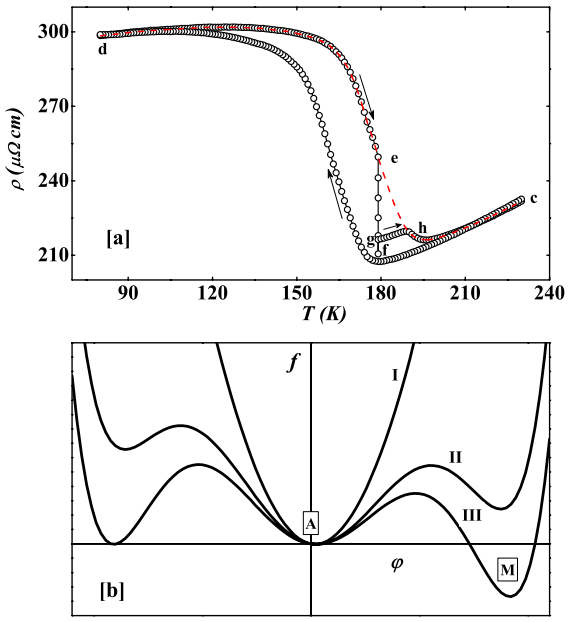

FIG. 3. (Color online) (a) Resistivity as a function of temperature with a protocol discussed in the text. (b) Landau-type free energy diagram (see text) for the first-order phase transition for decreasing temperature (I–III) in presence of field. "A" and "M" denote austenite and martensite minima, respectively. It is to be noted that the free energy profile is asymmetric with respect to the $\varphi=0$ line due to the presence of field.

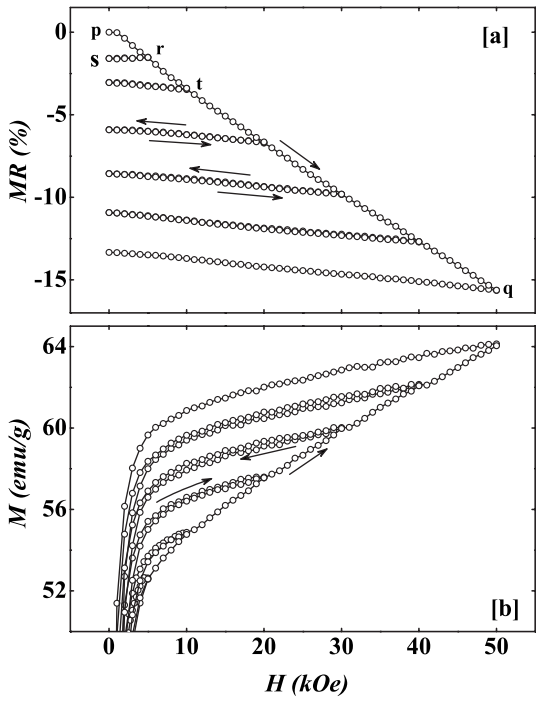

FIG. 4. (a) Magnetoresistance and (b) magnetization as a function of field recorded at 180 K. The measurement was performed by returning the field back to zero from different maximum fields (H_m^i).

a field and the state is retained on removal of the field. The question is whether the nature of the arrested state depends upon H or not. To shed light on it, the sample was first zero field cooled to 10 K and then heated back to 180 K. At 180 K, H was increased from zero to a certain value H_m and then removed gradually. This was repeated for increasing values of H_m (say, $H_m^1, H_m^2, \ldots, H_m^i, \ldots$) starting from 5 to 50 kOe. As expected, once a certain field H_m^i was applied, the sample retained the lower resistivity value even after the field was brought back to zero. In the next cycle, when the field was ramped up to the next higher value of H_m^{i+1}, ρ followed the same ramping down path until the previous applied field H_m^i was reached. Beyond H_m^i, ρ followed the master path, pq. The master path can be obtained if H is ramped up monotonously to its highest value. The minor paths (like sr) intercepted the master path on their respective maximum exposed field values. This clearly shows that the field-induced state remembers the value of the last highest field (H_m^i) it has experienced. This is an example of magnetic memory found in this alloy, where different electronic and magnetic states can be created by varying the value of H_m. It has been depicted in Fig. 4: for example, the field was first ramped up to 5 kOe (point p to r) and then ramped down to zero (r to s). When the field was again ramped up from zero to the next field value of 10 kOe, ρ followed the path s to r until the previous highest experienced field (here 5 kOe) was reached (point r) and after that it followed the master path (pq) to reach the point t corresponding to $H_m=10$ kOe. A similar thing happens for higher and higher values of H_m (even observed for $H_m=90$ kOe). The memory effect is also seen in the M versus H measurement at 180 K as depicted in Fig. 4(b).

Magnetic field-induced arrested state and magnetic memory effect have been observed in systems such as frozen ferrofluids, interacting nanoparticles, and metal-insulator multilayers. However, in all those cases the physics behind it is the spin-glass-like dynamics.[12] We do not see any signature of glassiness in the sample, for example, the ac susceptibility does not show any change in the martensitic transition temperature with frequency. The more probable scenario here is the magnetic field-induced first-order phase transition. The ability of the present sample to remember the field from where it has been backtracked is referred to as *return point memory effect*[13,14] and it can take place as a function of stress or temperature in addition to H. This is connected to the metastability of the system in the vicinity of a disordered induced first-order transition.[13] Recently, x-ray diffraction measurement has confirmed field-induced first-order transition in the Ni-Mn-Sn alloy, where martensite fraction transformed into the austenite by the application of H.[15] When a magnetic field is applied, some martensite fraction transforms into austenite, which has a lower resistivity than martensite, resulting large negative MR. The martensite has lower magnetic moment than austenite, and as a result the effect of the transformation is also visible in M. When the field is removed the system does not recover the martensite fraction. This irreversible nature of the field-induced transition was found in XRD measurement by Koyama *et al.*[15]

Phenomenologically, Landau type of free energy expression can been used to describe the first order MT,[16,17] where free energy and the order parameter (φ) are related as $f(\varphi) = a_2\varphi^2 - a_4\varphi^4 + a_6\varphi^6 - \gamma\varphi$ where a_i's are the parameters for the particular material, and γ is a term proportional to the

externally applied field. For T-dependent transition, $a_2 \sim a_2^0(T-T_0)$, and the free energy curves for different T are plotted in Fig. 3(b). Across the region of transition, the martensite and the austenite coexist in different free energy minima separated by an energy barrier. Thermal irreversibility in various physical quantities arises due to the fact that one of the states becomes metastable (supercooled or superheated state) and the system remains trapped there even when T crosses the critical point.

A similar situation can arise when the transition takes place as a function of H rather than T. Since field favors the formation of austenite, application of H is equivalent to the increase of temperature. H changes the free energy pattern as well and allows redistribution of the relative fraction of product and parent phases. Suppose the system is in a particular state at temperature T_0 and field H_0, where both phases are coexisting with austenite and martensite fractions being, respectively, x_A and $x_M=1-x_A$. This state can be represented by curve (III) of the free energy plot shown in Fig. 3(b). As we increase H isothermally, the free energy curve will change to curve (II). Here, the martensitic minimum lifts up to higher value and the barrier $[\sigma=\sigma(T,H)]$ between the parent and product phases decreases, allowing the formation of austenite. The phase fractions become $x_A'=x_A+\delta x_A$, $x_M'=(1-x_A-\delta x_A)$. The fraction, δx_A, transformed from martensite to austenite, depends upon the change in H. When the field is brought back to H_0, the free energy curve returns back to its previous field pattern (from curve II to curve III). However, the $\sigma(T,H)$ does not allow the martensite to regain its transformed fraction, and we get a state with arrested (metastable) austenite fraction, δx_A. This state will bear the memory of the highest field, H_m, it has been exposed to by virtue of the amount of δx_A it contains. The arrested state remains arrested until the barrier height is changed through the change in T or H. If T is kept constant, and H is increased from H_0, nothing will happen until the last highest exposed field is crossed. Further increase of H (beyond H_m), however, produces more amount of austenite and the system attains a different x_A, x_M ratio through further reduction of the free energy barrier. It is to be noted that different field-induced arrested states can be created by any arbitrary applied field. This is in contrast with the arrested states in Gd_5Ge_4 and Mn-site doped manganites,[18] where field-induced transitions take place only at certain values of H.

In conclusion, the sample $Ni_2Mn_{1.4}Sn_{0.6}$ shows reasonably large magnetoresistance around the region of first-order martensitic transition. MR is highly irreversible with respect to the applied magnetic field. A nice magnetic memory effect is observed, as the sample remembers the last highest field that it was exposed to. This can be exploited for important device related applications in the future.

*sspsm2@iacs.res.in

[1] G. Guenin, Phase Transitions **14**, 165 (1989).
[2] S. Kartha, J. A. Krumhansl, J. P. Sethna, and L. K. Wickham, Phys. Rev. B **52**, 803 (1995).
[3] S. B. Roy and P. Chaddah, Phase Transitions **77**, 767 (2004).
[4] S. Chatterjee, S. Giri, S. Majumdar, A. K. Deb, S. K. De, and V. Hardy, J. Phys.: Condens. Matter **19**, 346213 (2007).
[5] A. Sozinov, A. A. Likhachev, N. Lanska, and K. Ullakko, Appl. Phys. Lett. **80**, 1746 (2002).
[6] R. Kainuma, Y. Imano, Y. Sutou, H. Morito, S. Okaoto, O. Kitakam, K. Oikawa, A. Fujita, T. Kanomata, and K. Ishta, Nature (London) **439**, 957 (2006).
[7] T. Krenke, M. Acet, E. F. Wassermann, X. Moya, L. Mañosa, and A. Planes, Nat. Mater. **4**, 450 (2005).
[8] T. Krenke, E. Duman, M. Acet, E. F. Wassermann, X. Moya, L. Mañosa, A. Planes, E. Suard, and B. Ouladdiaf, Phys. Rev. B **75**, 104414 (2007).
[9] Z. H. Liu, H. Liu, X. X. Zhang, X. K. Zhang, John Q. Xiao, Z. Y. Zhu, X. F. Dai, G. D. Liu, J. L. Chen, and G. H. Wu, Appl. Phys. Lett. **86**, 182507 (2005).
[10] V. K. Sharma, M. K. Chattopadhyay, K. H. B. Shaeb, Anil Chouhan, and S. B. Roy, Appl. Phys. Lett. **89**, 222509 (2006).
[11] Y. Sutou, Y. Imano, N. Koeda, T. Omori, R. Kainuma, K. Ishida, and K. Oikawa, Appl. Phys. Lett. **85**, 4358 (2004).
[12] Y. Sun, M. B. Salamon, K. Garnier, and R. S. Averback, Phys. Rev. Lett. **91**, 167206 (2003).
[13] J. P. Sethna, K. Dahmen, S. Kartha, J. A. Krumhansl, B. W. Roberts, and J. D. Shore, Phys. Rev. Lett. **70**, 3347 (1993).
[14] J. Ortin, J. Appl. Phys. **71**, 1454 (1992).
[15] K. Koyama, K. Watanabe, T. Kanomata, R. Kainuma, K. Oikawa, and K. Ishida, Appl. Phys. Lett. **88**, 132505 (2006).
[16] F. Falk and P. Konopka, J. Phys.: Condens. Matter **2**, 61 (1990).
[17] Y. Huo, Continuum Mech. Thermodyn. **1**, 283 (1989).
[18] V. Hardy, S. Majumdar, S. Crowe, M. R. Lees, D. McK. Paul, L. Hervé, A. Maignan, S. Hébert, C. Martin, C. Yaicle, M. Hervieu, and B. Raveau, Phys. Rev. B **69**, 020407(R) (2004) and references therein.

High-field magnetic phase transitions and spin excitations in magnetoelectric $LiNiPO_4$

Rasmus Toft-Petersen,[1] Jens Jensen,[2] Thomas Bagger Stibius Jensen,[1] Niels Hessel Andersen,[1] Niels Bech Christensen,[1,3] Christof Niedermayer,[3] Michel Kenzelmann,[3] Markos Skoulatos,[4] Manh Duc Le,[4] Kim Lefmann,[2,5] Sonja Rosenlund Hansen,[2] Jiying Li,[6] Jerel L. Zarestky,[6] and David Vaknin[6]

[1]*Materials Research Department, Risø DTU, Technical University of Denmark, DK-4000 Roskilde, Denmark*
[2]*Niels Bohr Institute, Universitetsparken 5, DK-2100 Copenhagen, Denmark*
[3]*Laboratory for Neutron Scattering, ETH Zürich and Paul Scherrer Institute, CH-5232 Villigen, Switzerland*
[4]*Helmholtz Zentrum Berlin for Materials and Energy, Hahn-Meitner-Platz 1, D-14109 Berlin, Germany*
[5]*Nano-Science Center, Niels Bohr Institute, Universitetsparken 5, DK-2100 Copenhagen, Denmark*
[6]*Ames Laboratory and Department of Physics and Astronomy, Iowa State University, Ames, Iowa 50011, USA*

(Dated: January 19, 2011)

The magnetically ordered phases and spin dynamics of magnetoelectric $LiNiPO_4$ have been studied in fields up to 17.3 T along the c axis. Using neutron diffraction, we show that a previously proposed linearly polarized incommensurate (IC) structure exists only for temperatures just below the Néel temperature T_N. The ordered IC structure at the lowest temperatures is shown instead to be an elliptically polarized canted spiral for fields larger than 12 T. The transition between the two IC phases is of second order and takes place about 2 K below T_N. For $\mu_0 H > 16$ T and temperatures below 10 K, the spiral structure is found to lock in to a period of five crystallographic unit cells along the b axis. Based on the neutron diffraction data, combined with detailed magnetization measurements along all three crystallographic axes, we establish the magnetic phase diagrams for fields up to 17.3 T along c and for fields up to 16 T along a and b. The spin excitations in the high-field IC spiral phase have been studied in detail by inelastic neutron scattering. A mean-field analysis shows that the spin Hamiltonian derived previously from the low-temperature spin waves at zero field predicts the transition between the linear and elliptical polarization of the IC structure, and that a generalization of the spin-wave theory, assuming the random-phase-approximation, accounts for the inelastic scattering data obtained in the commensurable uniform phase at fields below 12 T as well as those obtained in the high-field IC spiral phase.

PACS numbers:

I. INTRODUCTION

Materials with coexisting ferroic order parameters – the so-called multiferroics – have received much attention in recent years.[1,2] Some of these multiferroics exhibit a magneto-electric (ME) coupling, where an applied magnetic field induces an electric polarization density and vice versa.[3] In some of these cases the magnetic ordering temperature and the onset temperature of the ME effect are identical and ferroelectricity is generated by the long range magnetic order being perturbed by the magnetic field.[4–7] The *lithium-ortho-phosphates* $LiMPO_4$ (M = Mn, Co, Fe or Ni) are isostructural compounds that all exhibit a strong ME effect in their low-temperature commensurate (C) antiferromagnetic (AFM) phases.[8–10] $LiNiPO_4$ stands out among the lithium-ortho-phosphates by exhibiting incommensurate (IC) magnetism, suggesting the presence of competing magnetic interactions. This expectation was confirmed directly by inelastic neutron scattering in Ref. 11.

The $LiNiPO_4$ compound has orthorhombic symmetry with space group *Pnma* (no. 62) and lattice parameters $a = 10.02$ Å, $b = 5.83$ Å and $c = 4.66$ Å.[12] There are four magnetic Ni^{2+}-ions in each unit cell with spin $S = 1$. At zero magnetic field the system displays long-range AFM order at temperatures below $T_N = 21.7$ K,[13] while short-range IC magnetic order exists in the temperature range $T_N < T < 40$ K.[14] Between T_N and $T_{NC} = 20.8$ K, $LiNiPO_4$ exhibits spontaneous IC magnetic order with ordering wave vector $\mathbf{k}_{ic} = (0, k_{ic}, 0)$.[7,14–16] Below T_{NC}, the AFM structure is commensurate with the lattice in the sense that the magnetic and crystallographic unit cells are identical. In this phase, the ordered moments are almost parallel to the crystallographic c axis with a slight canting along the a axis,[7,13] as shown schematically in Fig. 1. A magnetic field applied along the c axis induces a first order C to IC phase transition at a field strength $\mu_0 H$ varying between 12 and 13.5 T depending on temperature.[7] In Ref. 7, the high-field IC structure at low temperatures, like the zero-field IC structure observed between T_N and T_{NC}, was suggested to be linearly polarized, but it was also pointed out that the data did not exclude an elliptical polarization. The matter was left unresolved, since no direct evidence for a spiral structure was observed.

The low-temperature C–IC phase transition is the first out of the five magnetic-field induced transitions observed by Khrustalyov *et al.*[17] as peaks in the differential magnetic susceptibility dM/dH derived from magnetization measurements in pulse magnetic fields extending up to 27 T along the c axis. A second transition at $\mu_0 H \approx 16$ T gives rise to a much smaller peak in dM/dH than the C–IC transition.

In this paper, we present neutron-diffraction studies as

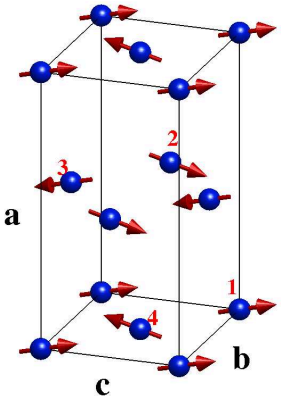

FIG. 1: (Color online) The zero-field commensurate magnetic structure of $LiNiPO_4$ observed below T_{NC}. The magnetic unit cell is shifted $(-0.25, -0.25, 0)$ with respect to the structural unit cell. The magnetic ion positions are numbered $1-4$ (after Ref. 7).

a function of temperature and magnetic fields up to 17.3 T clarifying the structures of the IC magnetic phases of $LiNiPO_4$. The high field, low-temperature IC magnetic structure is shown to be a canted, elliptical spiral with the spin-components rotating in the crystallographic ac plane. This structure undergoes a temperature-driven transition to a canted, linearly polarized structure, where all moments are nearly parallel or antiparallel to the c axis. At fields larger than 16 T and temperatures below 10 K, the low-temperature IC spiral conforms to a commensurate quintupling of the crystallographic unit cell along the b axis corresponding to an ordering wave vector $(0, \frac{1}{5}, 0)$. To assist the neutron diffraction determination of the phase boundaries for fields along c, we have performed detailed magnetization measurements up to 16 T. The combined data are used to present the full $(\mu_0 H, T)$-phase diagram for fields up to 17.3 T. Magnetization measurements for fields up to 16 T along the a and b axes have been used to establish the corresponding $(\mu_0 H, T)$-phase diagrams.

Furthermore, we have studied the low-temperature spin excitation spectrum in the spiral IC phase as well as field and temperature dependent properties of the spin excitations in the commensurate low-temperature phase by inelastic neutron scattering. The data are analyzed within the random-phase approximation (RPA) in terms of the spin Hamiltonian established in Ref. 11. The mean-field (MF) predictions derived from the same spin Hamiltonian are compared with the experimental results for the zero-field susceptibilities, the phase diagram and the magnetic structures.

The paper is organized as follows: In the next section, an account for the irreducible representations of the magnetic structures in $LiNiPO_4$ is given. This is succeeded by a description of the experimental details in Sec. III, and a presentation of neutron diffraction data from experiments at RITA-II (III A) and FLEX/V2 (III B) spectrometers. In Sec. III C, the bulk magnetization data are presented along with complete $(\mu_0 H, T)$ phase diagrams for fields along all three crystallographic directions. The structural part of the paper is followed by a description of the MF model and the RPA in Sec. IV A. In Sec. IV B, we present experimental results for the spin-wave excitations in the high-field IC spiral phase obtained at RITA-II. These results are compared with the predictions of the RPA model. Concluding remarks are given in Sec. V.

II. MAGNETIC STRUCTURES IN $LiNiPO_4$

The four magnetic ions in $LiNiPO_4$ are situated at $\mathbf{r}_1 = (0.275, 0.25, 0.98)$, $\mathbf{r}_2 = (0.775, 0.25, 0.52)$, $\mathbf{r}_3 = (0.725, 0.75, 0.02)$ and $\mathbf{r}_4 = (0.225, 0.75, 0.48)$ in the orthorhombic unit cell (see Fig. 1). A thorough analysis of the irreducible representations[18] of the magnetic structures in $LiNiPO_4$ has been performed in Ref. 15. In the uniform case, i.e. when the magnetic and the crystallographic unit cells are identical, any magnetic structure is described by a linear combination of the twelve basis structures presented in Fig. 2. This basis is divided into four symmetry classes (A, C, G, and F) for each Cartesian component of the moments. In the IC phases, where the ordering wave vector is $\mathbf{k}_{ic} = (0, k_{ic}, 0)$, the same basis applies except that it includes a phase factor $\beta = e^{i\pi k_{ic}}$ due to the modulation of the moments. The Fourier transforms of the spin components may be divided into the four symmetry classes $A_\alpha = (+, -, -\beta, +\beta)$, $G_\alpha = (+, -, +\beta, -\beta)$, $C_\alpha = (+, +, -\beta, -\beta)$ and $F_\alpha = (+, +, +\beta, +\beta)$, where the brackets show the relative phase factors of the α component of the spins on the sites $(\mathbf{r}_1, \mathbf{r}_2, \mathbf{r}_3, \mathbf{r}_4)$ in one unit cell. α is equal to x, y, or z, where these axes are along, respectively, the a, b, and c axes of the lattice.

These basis structures span the space of possible IC magnetic structures in $LiNiPO_4$, when the ordering wave vector $\mathbf{k}_{ic}$ is along the b axis. The symmetry operations of the space group $Pnma$ that leave $\mathbf{k}_{ic}$ invariant (excluding lattice translations), constitute the little group

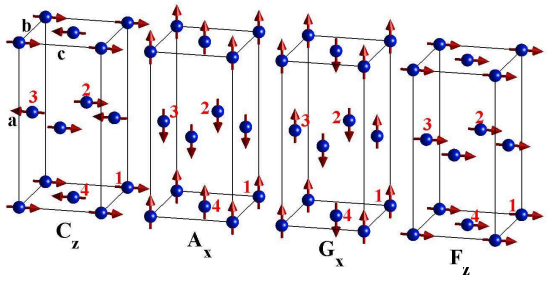

FIG. 2: (Color online) Four of the twelve commensurate irreducible basis structures related to the three AFM symmetry classes (A, G and C) and the ferromagnetic class (F). Only one of the three possible polarizations (x, y, z) is shown for each one of the four different classes.

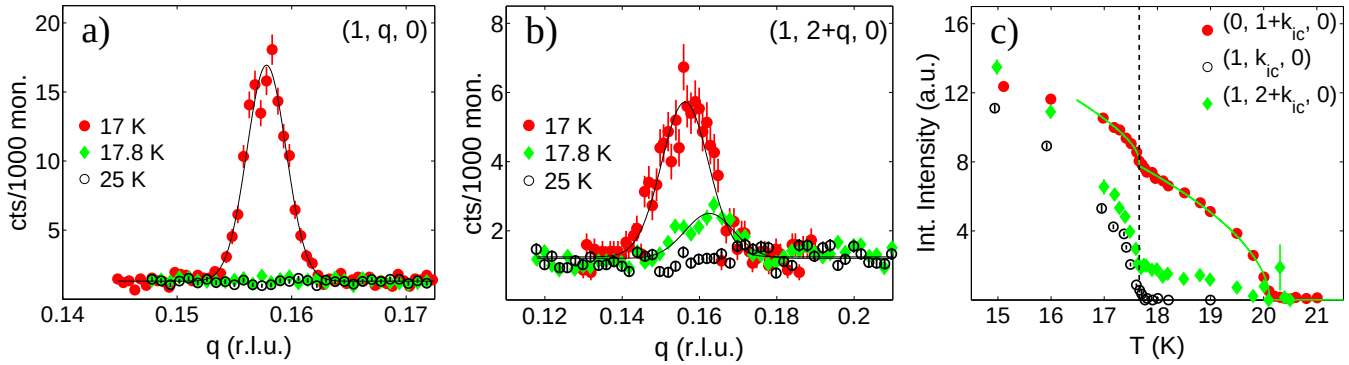

FIG. 3: (Color online) a)-b) Neutron-diffraction scans through the $(1, k_{\rm ic}, 0)$ and the $(1, 2 + k_{\rm ic}, 0)$ peaks at 14.7 T applied along the c axis at temperatures close to the transition at 17.7 K. The two peaks reflect, respectively, the A_z (neglecting A_y as discussed in the text) and the weighted sum of the A_z and A_x components of the spiral structure. The A_z component disappears above 17.7 K while the A_x component persists. c) Integrated intensities of $(0, 1+k_{\rm ic}, 0)$, $(1, k_{\rm ic}, 0)$ and $(1, 2+k_{\rm ic}, 0)$ as functions of temperature at 14.7 T applied along the c axis. The integrated intensity from the $(1, k_{\rm ic}, 0)$ and the $(1, 2+k_{\rm ic}, 0)$ peaks have been multiplied by a factor of 140 and 170, respectively. The onset of an additional order parameter below 17.7 K is evident.

$G_{\mathbf{k}_{\rm ic}} = \{1, 2'_y, m'_{xy}, m'_{yz}\}$. There are four one-dimensional irreducible representations, $\Gamma_1 - \Gamma_4$, of this little group. The twelve IC basis structures are divided into corresponding subsets according to how they transform under the symmetries of $G_{\mathbf{k}_{\rm ic}}$. These subsets are

$$\begin{array}{ll} \Gamma_1: \{A_x, G_y, C_z\} & \Gamma_2: \{G_x, A_y, F_z\} \\ \Gamma_3: \{C_x, F_y, A_z\} & \Gamma_4: \{F_x, C_y, G_z\}. \end{array} \quad (1)$$

If a magnetic IC structure is found to involve a component from one of the irreducible representations (for instance C_z), it is more or less inevitable that it also involves the two other components (A_x and G_y).

III. EXPERIMENTAL DETAILS

Two high-quality single crystals measuring $5 \times 5 \times 9$ mm^3 (0.4 g) and $2 \times 2 \times 3$ mm^3 (0.02 g), respectively, were used in the experiments. Both elastic and inelastic neutron scattering experiments were performed on the RITA-II triple-axis spectrometer at the Paul Scherrer Institute (SINQ, PSI) using the larger crystal oriented on an aluminum sample holder with the c axis vertical in a 14.9 T Oxford cryomagnet. No collimation was used. For inelastic scattering, varying incoming neutron energy was used with fixed neutron momentum transfer $\mathbf{Q}$ and fixed final neutron energy of 5 meV. A Be-filter was placed before the analyzer to remove higher order neutrons. RITA-II has a seven blade pyrolytic graphite (PG) analyzer providing high q-resolution, when measuring the dispersion along $(0, q, 0)$. When measuring the dispersions along $(q, 1, 0)$ and $(q, 1 + k_{\rm ic}, 0)$, the intensity from only the three central blades was collected. The diffraction studies were performed with 4.04 Å (5 meV) neutrons using only the central blade. On the V2/FLEX triple-axis spectrometer at Helmholtz Zentrum Berlin neutron diffraction was performed for magnetic fields up to $\mu_0 H = 17.3$ T. The smaller crystal was placed with the c axis vertical in an aluminum sample holder clamping it between two Dysprosium booster pieces, which add 2.5 T to the field provided by a 14.8 T Oxford cryomagnet. We used 4.04 Å neutrons, a flat PG analyzer and 60′ collimation between monochromator and sample, sample and analyzer as well as between the analyzer and the detector. A CRYOGENIC cryogen free measurement system (CFMS) at Risø DTU was used to perform vibrating sample magnetization (VSM) measurements. Magnetic fields $0 \leq \mu_0 H \leq 16$ T were applied along all three principal axes for temperatures $2 < T < 300$ K. Susceptibilities are measured at $\mu_0 H = 1$ T, which lies within the linear regime of magnetization vs. field.

A. The transition between IC structures with different polarizations

The previously determined high-field IC structure with ordering wave vector $(0, k_{\rm ic}, 0)$ had basically C_z symmetry with a small A_x canting plus small uniform F_z and G_x components induced by the field.[7,15] It was argued that the IC structure was this canted structure with the moments polarized linearly nearly along z, but that it could also be a spiral with spins rotating in the ac-plane. To examine if this is the case, we have used the RITA-II spectrometer to measure the temperature dependence of three magnetic IC peaks $(0, 1 + k_{\rm ic}, 0)$, $(1, k_{\rm ic}, 0)$ and $(1, 2 + k_{\rm ic}, 0)$ at 14.7 T.

The sensitivity of neutron scattering to magnetic structures is a consequence of a scattering cross-section which, for a collinear structural component, is proportional to $|F_R(\mathbf{Q})|^2 |P(\mathbf{Q})|^2$, where the structure ($F$) and polarization ($P$) factors are given by

$$F_R(\mathbf{Q}) = \sum_d \mathbf{m}_d^R e^{i\mathbf{Q}\cdot\mathbf{r}_d}, \quad \mathbf{P}(\mathbf{Q}) = \hat{\mathbf{Q}} \times (\hat{\mathbf{e}} \times \hat{\mathbf{Q}}). \quad (2)$$

	F_C^2	F_A^2	F_G^2	F_F^2	P_x^2	P_y^2	P_z^2
$(0, 1+k_{\rm ic}, 0)$	16	0	0	0	1	0	1
$(1, k_{\rm ic}, 0)$	0	15.6	0.4	0	0.09	0.91	1
$(1, 2+k_{\rm ic}, 0)$	0	15.6	0.4	0	0.93	0.07	1

TABLE I: Squared structure (F) and polarization (P) factors for the three IC peaks used to establish the spiral structure in terms of the irreducible representations. The structure factors are normalized to unit spin lengths of the components. We have used $k_{\rm ic} = 0.18$ rlu, but note that small changes of $k_{\rm ic}$ have no effect on our conclusions.

Here $\mathbf{m}_d^R$ is the magnetic moment of the ion at site $d = 1, \ldots, 4$ in the symmetry class R, $\hat{\mathbf{Q}}$ is the unit vector along the neutron momentum transfer and $\hat{\mathbf{e}}$ is the unit vector along $\mathbf{m}_d^R$. For each of the three peaks, Table I lists $|F_R(\mathbf{Q})|^2$ (normalized to unit magnetic moment) and $|P(\mathbf{Q})|^2$ for $R = C$, A, G, F and all spin directions $\hat{\mathbf{e}}$ parallel to x, y or z. The numbers represent the sensitivity of each peak to the different basis structure components.

As presented in Fig. 3 a), the extension of the neutron diffraction experiments has now shown that there is intensity in the $(1, k_{\rm ic}, 0)$ reflection. This reflection derives mainly from an A_y or an A_z component according to Table I. The intensity disappears below and not at $T_{\rm N} \approx 20.8$ K indicating the presence of a second magnetic phase transition at about 17.7 K. Referring to Eq. (1) it is seen that the order parameter between 17.7 K and $T_{\rm N}$ belongs to the irreducible Γ_1 representation, whereas the new order parameter appearing below 17.7 K has the symmetry of the Γ_2 or the Γ_3 representation depending on whether the $(1, k_{\rm ic}, 0)$ peak is due to, respectively, an A_y or an A_z component. The temperature dependence of the strong peak intensity at $(0, 1 + k_{\rm ic}, 0)$ is depicted in Fig. 3 c), and Table I shows that the two components C_z and C_x are weighted equally and are the only ones appearing in this scan. The abrupt increase shown by the $(0, 1+k_{\rm ic}, 0)$ peak intensity at 17.7 K for decreasing temperatures allows a clear choice between the two possibilities for the new order parameter. A Γ_3 order parameter, which contains a C_x component, contributes directly to the $(0, 1 + k_{\rm ic}, 0)$ peak, whereas the possibility of a Γ_2 order parameter can be dismissed since it has no direct effect on this scan. The behavior of the $(1, 2 + k_{\rm ic}, 0)$ intensity as a function of temperature shown in Fig. 3 b) and c) is consistent with this result. This peak intensity reflects the A_x and A_z components, and for increasing temperatures it shows a rapid drop at 17.7 K indicating a vanishing A_z component. The intensity, which remains above 17.7 K, is due to the A_x component being nonzero up to $T_{\rm N}$. Table I shows that both the $(1, k_{\rm ic}, 0)$ and the $(1, 2+k_{\rm ic}, 0)$ peak may contain contributions from the possible G components. However, since none of the peaks which are dominated by the G components have been seen, they may safely be neglected here, where their contributions are weighted with an intensity factor of 1/40 compared with the A components.

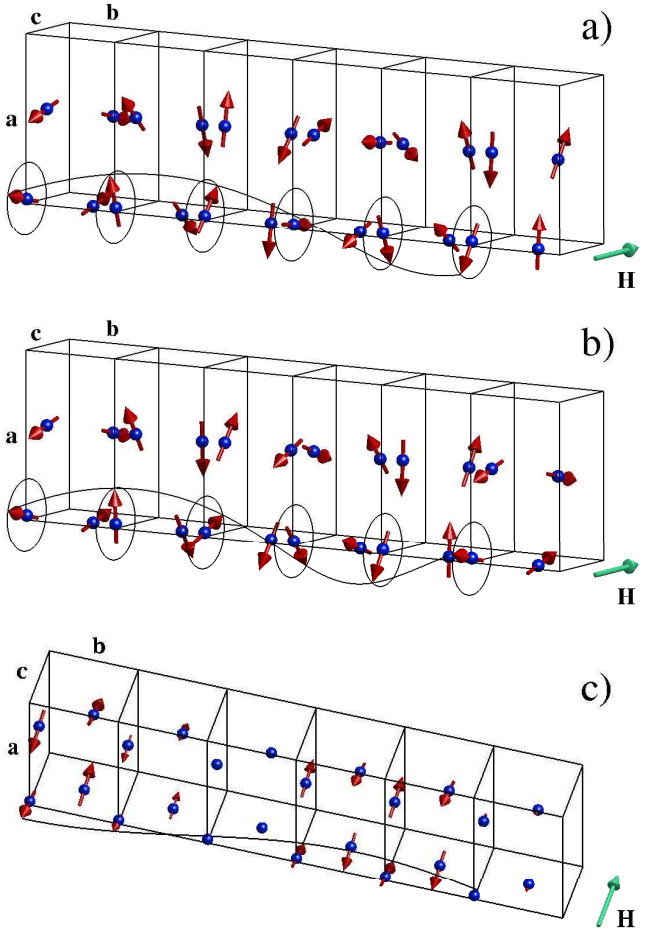

FIG. 4: (Color online) a) Magnetic IC spiral at 2 K and $\mu_0 H = 13$ T applied along c. The circles around the lower left ion marks the rotation plane of the spins and the black line marks the spiral itself. b) Lock-in commensurable spiral $\mu_0 H > 16$ T and $T < 10$ K. The 1/5 modulation is evident by comparing the 1st and the 6th unit cell. c) Linearly polarized IC structure; the line marks the sinusoidal modulation. In the phase diagram for fields along c, shown in Fig. 9, the three structures are denoted as $\rm IC_{ac}$, 1/5-C and $\rm IC_c$, respectively.

Generally, a helical/cycloidal ordering is energetically more favorable than a linearly polarized square wave of fully polarized spins in the $T = 0$ limit, as long as the anisotropy within the plan of the ordered moments is weak. In the present case the system may approach a circular polarization of the moments by either combining the C_z component with a C_x or with a C_y component. The unique identification above, that the new order parameter below 17.7 K belongs to the Γ_3 representation, shows that the system chooses the first one of the two possibilities. This choice is consistent with the fact that the anisotropy parameters derived from the spin-wave analysis [see Eq. (5) below] identifies the *ac* plane to be the easy one. Experimentally, it is difficult to measure

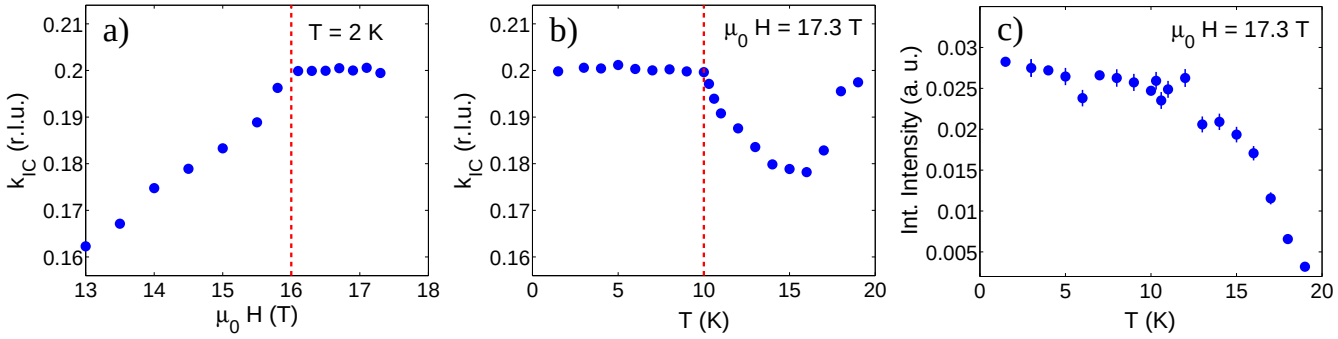

FIG. 5: (Color online) The IC modulation $k_{\rm ic}$ as a function of field at 2 K (a) and as a function of temperature at 17.3 T applied along the c axis (b). The statistical errors are smaller than the markers. c) The temperature dependence of the sum of integrated intensities from the symmetry related peaks $(0, 1 \pm k_{\rm ic}, 0)$ measured at 17.3 T applied along the c axis.

the C_y component directly but the analysis above, where the irreducible representations, or symmetry arguments, are utilized in the interpretation of the experiments indicates that Γ_4, and thereby the C_y component, has to be zero. This result is also valid at the lower temperatures not included in Fig. 3, since the $(1, k_{\rm ic}, 0)$ peak indicating a non-zero Γ_3 component is observed all the way down to 2 K.

We conclude that the system shows two continuous phase transitions at decreasing temperatures in the presence of a c-axis field larger than 13.5 T. The ordered state just below $T_{\rm N}$ is described by an IC order parameter belonging to the irreducible representation Γ_1, with the dominating component C_z being slightly mixed with A_x. At about 17.7 K there is a new second-order phase transition, where the additional order parameter belongs to the Γ_3 representation and may be described as being the C_x component slightly mixed with the A_z component. This interpretation of the observations shown in Fig. 3 is in full agreement with the predictions of the MF-calculations presented below. The phase boundary between the linearly and elliptically polarized IC phases has been determined up to a field of 17.3 T. The two IC structures are illustrated in Fig. 4 a) and c), and the observed phase boundaries are shown in the phase diagram in Fig. 9.

B. The high field IC–C transition

At the V2/FLEX triple axis spectrometer we measured the IC modulation $k_{\rm ic}$ for fields along c in the range 13 T $< \mu_0 H <$ 17.3 T and for temperatures up to $T_{\rm N}$. To obtain an accurate value of $k_{\rm ic}$, both symmetry related peaks $(0, 1 \pm k_{\rm ic}, 0)$ were measured – optimizing the sample rotation and the scattering angle thoroughly – and obtaining $k_{\rm ic}$ as the average modulation of the two peaks. The modulation as a function of magnetic field at 2 K and as a function of temperature at 17.3 T is shown in Fig. 5. It is seen that the modulation stabilizes at $k_{\rm ic} = \frac{1}{5}$ at 2 K for $\mu_0 H > 16$ T marking a magnetic quintupling of the unit cell. At 17.3 T, the quintupling persists up to 10 K. The average measured value of the modulation in this phase is $k_{\rm ic} = 0.200(1)$. The accuracy of the determined value of $k_{\rm ic}$ is comparable to the obtainable instrumental precision. In addition, $k_{\rm ic}$ was measured as a function of field at 5 K and as a function of temperature at 16.8 T.

The $(1, k_{\rm ic}, 0)$ peak reflecting the A_z component is still observed above 16 T at 2 K (not shown), which indicates that the magnetic structure stays as an elliptical spiral at the transition from the IC phase to the high-field commensurate phase. The lock-in transition identified here explains the $\mu_0 H \simeq 16$ T transition observed by Khrustalyov *et al.*,[17] and the weakness of the signal they observed at this transition is consistent with that the lock-in only causes minor modifications of the magnetic structure. The commensurate magnetic spiral structure is shown in Fig. 4(b). The phase boundary between the IC spiral phase and the high-field commensurate spiral phase is included in the phase diagram shown in Fig. 9.

C. Phase boundaries determined from bulk magnetization measurements

Figure 6 shows the magnetization at 5 K as a function of applied field along all three crystallographic axes. The magnetization is almost linear along the a and b axes. Along the c axis the magnetic susceptibility is much smaller until the system enters the IC canted spiral phase at 12.2 T, where there is a fivefold increase of the magnetization. The transition is first order and hysteretic. We define the C–IC phase boundary in field scans as the field at which the differential magnetization dM/dH, measured for increasing fields, exhibits a maximum.

The IC–C phase boundary for fields applied along the c axis was determined by performing a series of VSM measurements at constant field while varying temperature and vice versa. Figure 7 shows the magnetization as a function of temperature at $\mu_0 H = 12.5$ T. Below $T_{\rm N}$ when the system is in the canted linearly polarized IC phase, the magnetization is gradually decreasing with

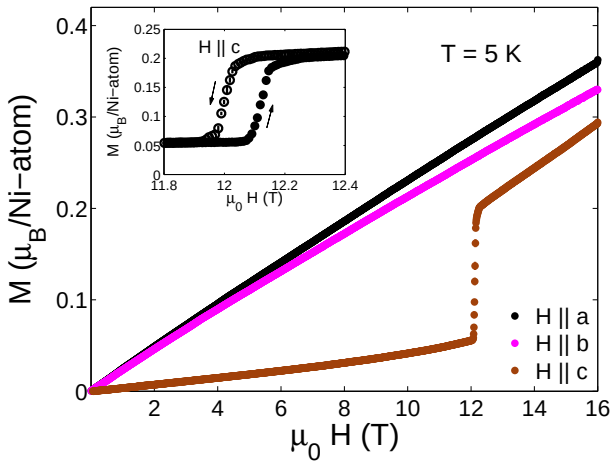

FIG. 6: (Color online) Magnetic field dependence of the magnetization measured along all three crystallographic axes at 5 K and for increasing fields. The inset zooms in on the hysteric C–IC transition observed for fields along c.

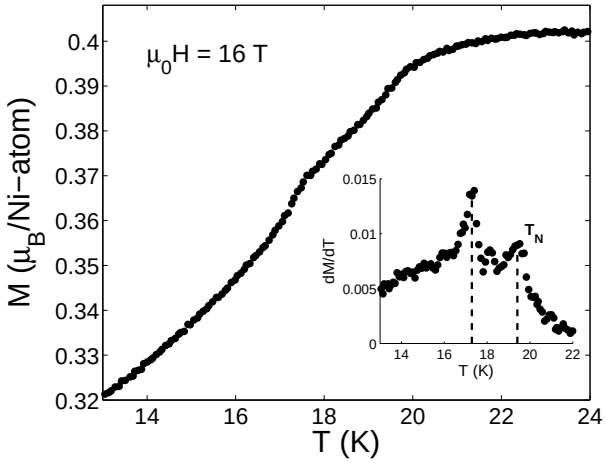

FIG. 8: Magnetization measured while cooling at a field of $\mu_0 H = 16$ T applied along the c axis. Two kinks are evident. The inset shows the derivative, where two transitions are marked by dashed lines.

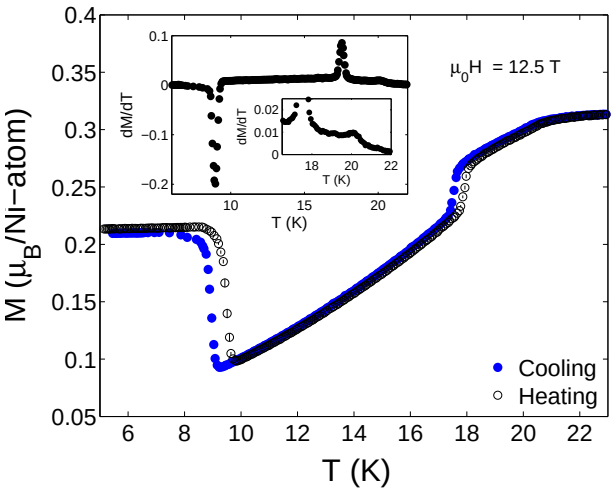

FIG. 7: (Color online) The temperature dependence of the magnetization at 12.5 T applied along the c axis.. The insets show the differential magnetization upon cooling with an additional focus on the kink at $T_{\rm N}$.

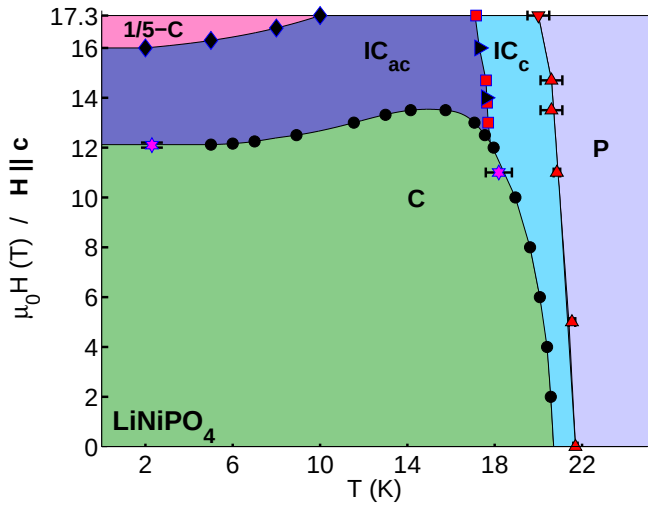

FIG. 9: (Color online) $(\mu_0 H, T)$ phase diagram of $LiNiPO_4$ for magnetic fields applied along the c axis. The black circles mark the C–IC phase boundary as found using magnetization data, supported by neutron diffraction data taken from Ref. 7 (stars). The diamonds mark the lock-in phase boundaries found using V2/FLEX data. The squares mark the boundary of the IC spiral phase found at RITA-II (below 15 T) and V2/FLEX (above 15 T), while the two right-pointing triangles indicate the phase boundary detected by VSM measurements. The ordering temperatures of the linearly polarized IC phase are taken from Ref. 7 (up-pointing triangles) and are supported by a measurement from V2/FLEX (down-pointing triangle). The errors on the VSM measurements are much smaller than the markers, while the error bars on the neutron-diffraction measurements are comparable to the marker size if not explicitly given. IC_c denotes the IC structure linearly polarized mainly along c, while IC_{ac} denotes the IC spiral in the ac-plane. C denotes the commensurate AFM phase and 1/5-C denotes the commensurate lock-in spiral phase.

decreasing temperatures. This is followed by a sudden drop in magnetization when entering the C phase at 17 K. At 9 K the magnetization increases rapidly upon entry into canted spiral phase. The first-order nature of the transitions in and out of the C phase is evident from the significant hysteresis. We define the phase boundaries in temperature scans to be the points of maximal or minimal differential magnetization upon cooling.

The transition from the structure with linearly polarized moments to the canted IC spiral can be seen directly in the VSM measurements. Figure 8 shows the temperature dependence of the magnetization at $\mu_0 H = 16$ T, measured upon cooling, in which two distinct kinks are evident: One at the ordering temperature $T_{\rm N}$, where IC

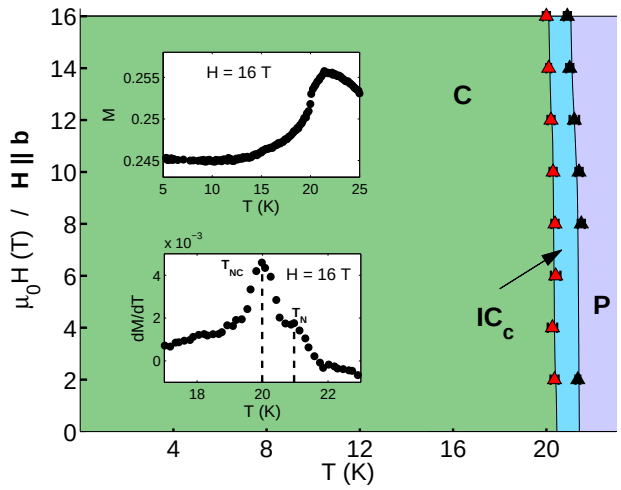

FIG. 10: (Color online) $(\mu_0 H, T)$ phase diagram determined from bulk magnetization measurements for fields applied along the b axis. The insets shows the magnetization and the differential magnetization at 16 T, where the transitions at $T_{\rm N}$ and $T_{\rm NC}$ are marked. $\rm IC_c$ denotes the IC structure linearly polarized mainly along c.

magnetic order sets in, and one at $T = 17.3$ K, where the spins start to develop a C_x component. The differential magnetization shows two distinct peaks, indicating the two second order phase transitions from the paramagnetic phase to the linear IC structure ($T_{\rm N}$) and from the linear to the spiral IC structure. Combining our neutron diffraction and magnetization measurements with neutron diffraction results from Ref. 7, we present a complete phase diagram of $LiNiPO_4$ for c-axis fields $\mu_0 H < 17.3$ T in Fig. 9.

The phase diagrams for fields along the a and b axes have also been determined. The field leads to minor decreases in $T_{\rm N}$ and $T_{\rm NC}$, but no other phase transitions than the paramagnetic–IC and the IC–C transitions were detected. Figure 10 shows the phase diagram obtained from magnetization measurements, when the field is applied along the b axis. The inset shows, that there is a small kink in the differential magnetization at $T_{\rm N}$ followed by a large peak at $T_{\rm NC}$, where the system becomes commensurate. The phase diagram for fields applied along the a axis is identical within errors to that for fields along b.

IV. MODEL CALCULATIONS

A. The mean-field model and the RPA

The Ni ions in $LiNiPO_4$ constitute an $S = 1$ system, where the orbital perturbation gives rise to a slight increase of the effective g-factor and an effective anisotropy field acting on the spins. According to experiments the saturated ordered moment is about 2.2 μ_B/Ni-ion in the limit of zero temperature,[7] and the Hamiltonian is assumed to be

$$\mathcal{H} = \frac{1}{2}\sum_{ij} J(ij)\mathbf{S}_i\cdot\mathbf{S}_j + \mathcal{H}_{\rm DM} + \sum_{\alpha,i} D_\alpha S_{\alpha i}^2 - g\mu_B\sum_i \mathbf{H}\cdot\mathbf{S}_i \tag{3}$$

with $g = 2.2$. The possible occurrence of anisotropic exchange terms is considered to be dominantly due to the Dzyaloshinsky–Moriya (DM) mechanism. Assuming only nearest neighbors to contribute, the DM interaction allowed by symmetry is[11,15]

$$\mathcal{H}_{\rm DM} = D_{14}\sum_{ij\in \rm n.n.} [S_z(1i)S_x(4j) - S_x(1i)S_z(4j) + S_z(3i)S_x(2j) - S_x(3i)S_z(2j)]\,, \tag{4}$$

where, e.g., $S_z(1i)$ only contributes to the sum if the ith site belongs to sublattice 1. The exchange constants and the single-ion anisotropy constants, D_x and D_y, were all deduced from the low-temperature spin waves in Ref. 11. We have repeated the spin-wave analysis using the more general RPA method presented in Ref. 19. The actual procedure used here is the same as used in the RPA analyses of the magnetic excitations in the two systems HoF_3 and PrNiSn,[20,21] which belong to the same space group as $LiNiPO_4$. The MF/RPA theory is obtained to zero order in the high-density $1/z$ expansion, and the corrections appearing in the first order of $1/z$ are discussed in Ref. 22 for the case of HoF_3. The energies and scattering intensities of the spin waves in $LiNiPO_4$, and the exchange constants derived here, agree with the results determined previously when applying the linear spin-wave theory,[11] except that the values of the anisotropy constants are slightly modified into (in units of meV):

$$D_x = 0.413, \quad D_y = 1.423, \quad D_{14} = \pm 0.32 \tag{5}$$

($D_z = 0$). This shows that the c axis is the preferred direction for the spins, and that the b axis is the hardest. The DM anisotropy has no effect on the spin waves to leading order,[11,15] and D_{14} is not determined from the spin waves but from the experimental value of $|\theta| = 7.8° \pm 2.6°$,[7] where θ is the canting angle the ordered moments are making with the c axis in the zero field and temperature limit. The canting may just as well be reproduced, if the DM term is replaced by the single-ion anisotropy term $\pm B_2^1(S_zS_x + S_xS_z)/2$ with $B_2^1 \approx 2.5$ meV. However, we find that this large single-ion anisotropy has unfavorable effects on the spin-wave energies, and that the amplitudes of the higher harmonics of the moments in the IC phase become much larger than observed. Although the DM anisotropy derived here is surprisingly large (about one third of the corresponding exchange interaction), it is likely that this is the dominating interaction determining the canting. The canting angle has a definite sign, depending on the sublattice considered, but this is difficult to detect experimentally, and the sign of D_{14} is left unspecified.

The susceptibility components have been calculated within the MF approximation and are compared with

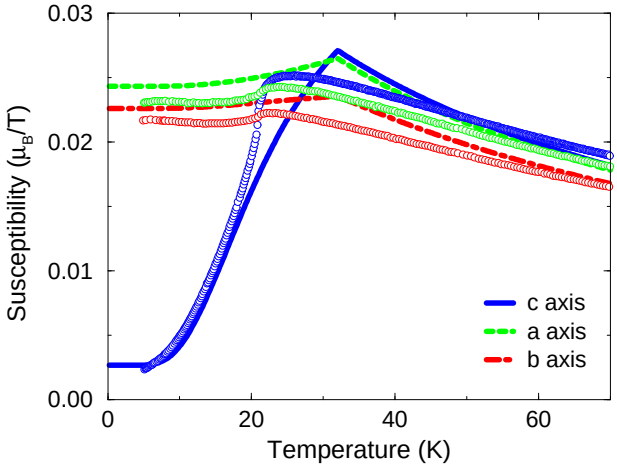

FIG. 11: (Color online) The calculated susceptibility components (solid lines), divided by μ_0, are compared with the experimental results obtained from our magnetization measurements after being corrected for a trace of paramagnetic impurities. The experimental results are consistent with those obtained by Kharchenko *et al.*[23]

our experimental results in Fig. 11. In order to get these results we have introduced one more exchange constant in the model in addition to the five constants given in Table I in Ref. 11. The exchange coupling J_b^c between an ion at $\mathbf{r}_i$ and its four diagonal neighbors belonging to the same sublattice, at $\mathbf{r}_i \pm \mathbf{b} \pm \mathbf{c}$, is assumed to be ferromagnetic with the value -0.23 meV. This has been done without changing $J(\mathbf{q})$ along the directions of $\mathbf{q}$ where the spin waves have been measured, by replacing J_b and J_c with, respectively, $J_b' = J_b - 2J_b^c = 1.13$ meV and $J_c' = J_c - 2J_b^c = 0.41$ meV. The transition temperature predicted by the MF model is about 32 K, i.e. 10 K above the experimental one. The exchange parameters determined from the spin waves in the zero temperature limit are close to be the true ones, and in terms of these exchange parameters the MF estimate of $T_{\rm N}$ is expected to be of the order of 10-30% higher than the true ordering temperature. Hence, it is plausible that most of the discrepancies in Fig. 11 are due to the MF approximation. Outside the critical regime the MF-model accounts reasonably well for the experimental results, which means that the values for $J_F(\mathbf{0})$ and the anisotropy constants D_x and D_y derived from the spin waves are trustworthy.

The RPA theory reproduces all the linear spin-wave theory results derived in Ref. 11 in the zero field and temperature limit. The present numerical method is straightforwardly generalized to account for the different complications – the canting of the spins due to D_{14} and the introduction of non-zero values of temperature and fields. In Fig. 12 is shown a comparison between theory and experiments when applying a field at 2 K, whereas Fig. 13 focuses on the temperature effects at zero field. Except that the MF/RPA theory may not be trusted close to $T_{\rm N}$, the comparisons shown in the two figures are quite satisfactory.

The exchange parameters at zero wave vector are derived to be (in meV) $J_F(\mathbf{0}) = 7.08$, $J_C(\mathbf{0}) = -3.64$, $J_A(\mathbf{0}) = 5.56$, and $J_G(\mathbf{0}) = -0.36$ for the four different symmetry configurations. These numbers show that the C configuration is the most favorable one, whereas the exchange interaction strongly opposes the A and F configurations. This is the situation at zero wave vector, but this is not changed much in the IC phase ($k_{\rm ic}$ is small). The c axis is the easy axis, and accordingly the ordered phase just below $T_{\rm N}$ is dominantly determined by the C_z configuration. That it is A_x rather than G_y which is accompanying the C_z component, is not explained alone by the circumstance that the y (b) axis is the hard axis, but is due to the relatively large DM anisotropy favoring A_x. It is worth to point out that any first-order DM interaction between a y component of a spin and a z or x component of a neighboring spin cancels by symmetry.[15] This means that the G_y component may only be coupled with the (C_z, A_x) components due to orbital modifications of the exchange integrals that are of second-order in the spin-orbit coupling. Furthermore, the possible couplings between G_y and the two other IC components are forced to vanish by symmetry in the limit of $k_{\rm ic} \to 0$.

The energy minimum in the spin wave dispersion along $(0, K, 0)$ is very shallow (see Figs. 12 and 13) showing that the difference between $J_C(\mathbf{k}_{\rm ic})$ and $J_C(\mathbf{0})$ is minute. The extra lock-in energy gained by the system at zero wave vector, where the lengths of the moments are no longer varying, is able to compensate for this energy difference already 1 K below $T_{\rm N}$, by which temperature $T_{\rm NC}$ the IC phase is being replaced by the corresponding uniform C phase. In the zero temperature limit, the MF model predicts the first order IC–C transition to occur at about the same c axis field, $\mu_0 H \approx 13$ T, as observed, and also that the structure in the IC phase is elliptically polarized by combining components from two one-dimensional irreducible representations, (C_z, A_x) and, 90° out-of-phase

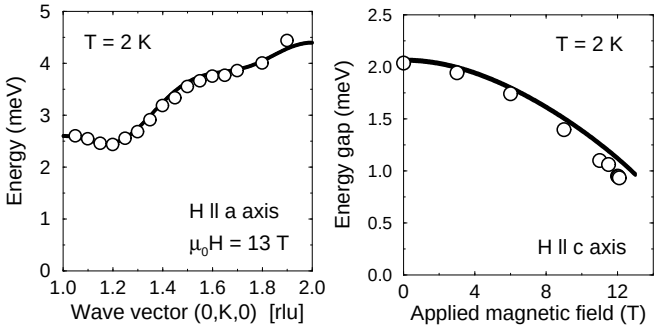

FIG. 12: Spin waves at 2 K. The left figure shows the calculated dispersion relation along $(0, K, 0)$ at a field of 13 T applied along the a direction compared with the experimental results. The spin-wave energy gap at $(0, 1, 0)$ as a function of a field applied along the c axis is compared with experiments performed by Strauss *et al.*[24] in the right figure.

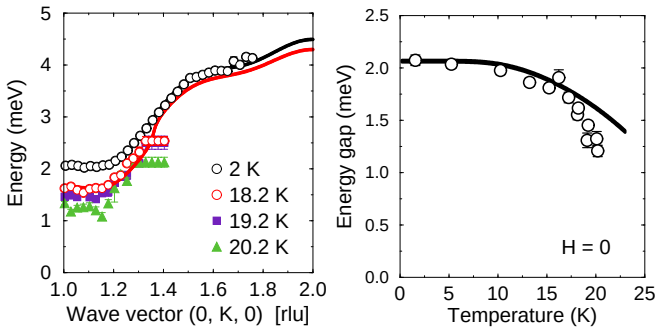

FIG. 13: (Color online) Spin waves at zero field. The figure to the left shows the RPA dispersion relation along $(0, K, 0)$ as a function of temperature in comparison with experimental results. To the right is shown a comparison between observations and calculations of the spin-wave energy gap at $(0, 1, 0)$ as a function of temperature.

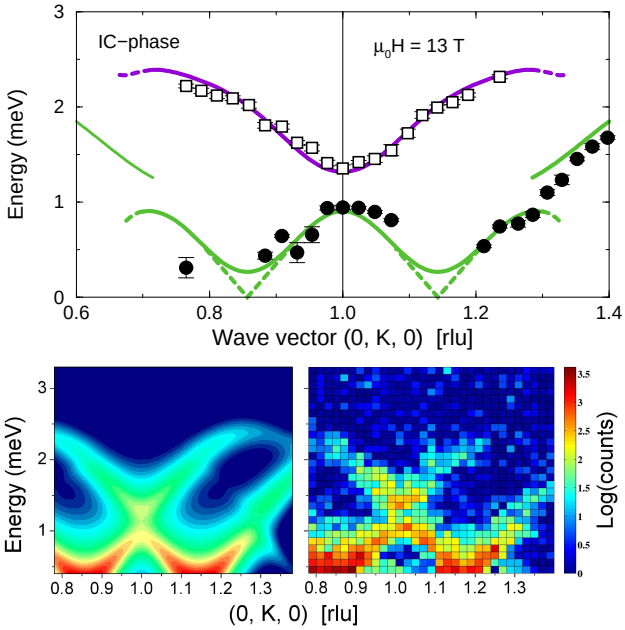

FIG. 14: (Color online) The low energy spin-wave dispersions measured along $(0, K, 0)$ in the IC-phase at 2 K and in a 13 T field applied along the c axis. The circles and squares in the upper figure show the experimental results. The solid lines are the predictions of the RPA in the case of $k_{\rm ic} = 1/7$, whereas the dashed straight lines indicate the Goldstone modes expected for an incommensurate structure. The two figures below are the corresponding logarithmic contour plots of the scattering intensities along $(0, K, 0)$. The experimental results are shown to the right to be compared with the calculated results shown in the left figure.

and with a slightly smaller amplitude, (C_x, A_z). In this way the IC structure is able to maintain a nearly constant length of the ordered moments by a slight cost in anisotropy energy (notice that the anisotropy within the ac plane is rather weak), which makes it competitive with the C structure. When the temperature is increased, at a constant c-axis field, the anisotropy within the ac plane implies that the (C_x, A_z) moment decreases faster than the main component, and the MF-model predicts that it vanishes 2-3 K below $T_{\rm N}$ in agreement with the experimental phase diagram. There have been some preliminary investigations of the higher harmonics in the IC phase,[24] and the intensity due to the third harmonic of the C_z component is observed to be about 10^{-3} times the peak intensity due to the first harmonic in the zero temperature limit. Once again this is in qualitative agreement with the results derived from the MF model. At least, the possibility that the linearly polarized structure should be the stable one at zero temperature can be excluded, since the observed intensity ratio is much smaller than the value of $\sim$1/9 expected for a linearly polarized squared-up structure.

The energies involved in the gradual changes of $k_{\rm ic}$ and in the lock-in transition to the commensurate 1/5-phase are too small to be modeled by the present MF calculations. However, the model does predict the presence of two additional transitions, one at a c-axis field of about 18 T and another one at about 20 T in the zero temperature limit. We anticipate that these two transitions are just those observed by Khrustalyov *et al.*[17] at 20 and 21 T (numbered 4 and 5 in their Fig. 1). If this is true, the model calculations show that the one at 20 T is due to a continuous but very rapid change of the higher harmonics (the most pronounced changes are shown by the zeroth and second harmonics of the C_z and C_x components), whereas the second transition is due to smaller but abrupt modifications of all the higher harmonics.

B. Spin dynamics in the high-field IC spiral phase

The spin waves have been studied experimentally in the high-field IC spiral phase. The incommensurable ordering implies that the excitation spectrum should contain a Goldstone mode reflecting that an overall phase shift of the spiral does not cost any energy. To investigate this phenomenon we have performed a number of inelastic neutron scattering experiments around the magnetic Bragg peak at low energies (above $\sim$0.4 meV). These results are compared with the RPA predictions derived from the MF-model in Figs. 14 and 15.

The numerical RPA method discussed above is straightforwardly generalized to the case, where the magnetic unit cells contains any integer multiple of 4 spins.[19] The numerical method presupposes a commensurable ordered structure, but the results may still be valid for describing an incommensurate system, if the commensurable period assumed in the calculations is sufficiently long. The most significant effect of the assumption of commensurability is that the excitations are going to exhibit a non-zero energy gap at the ordering wave vector instead of the soft-mode behavior expected in the incommensurable case. In the calculations shown in the two

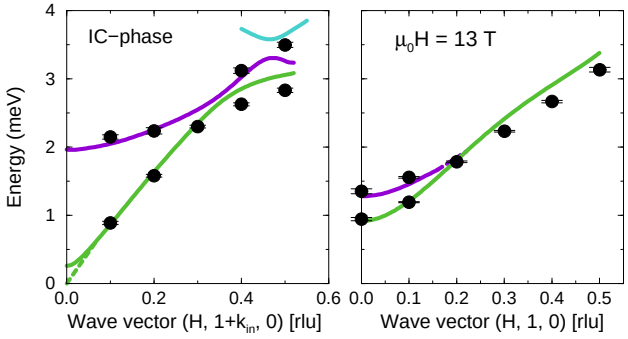

FIG. 15: (Color online) Spin-wave dispersions in the IC-phase at 2 K and 13 T along $(H, 1+k_{\rm ic}, 0)$ and $(H, 1, 0)$. The symbols are the same as used in Fig. 14.

figures, 14 and 15, we have assumed an ordered magnetic structure with a period of 7 crystallographic unit cells along the b axis, which in the model leads to an energy gap of about 0.25 meV at the ordering wave vector. Outside the close neighborhood of the magnetic Bragg points at $(0, 1 \pm k_{\rm ic}, 0)$, the assumption of commensurability is unimportant and the RPA predictions are found to be in nearly complete agreement with the experimental results, both with respect to the energies and the scattering intensities of the magnetic excitations. The most important energy gap induced by the IC ordering is the one at $(0, 1, 0)$, but also the presence of the smaller, higher-order one calculated at about $(0, 1 \pm 0.3, 0)$ has been verified by a direct observation of a two-peak scattering structure in a constant q scan at $(0, 1.3, 0)$.

We have made attempts to look for inelastic scattering peaks also outside the (q, ω) regime covered by Figs. 14 and 15 with no success. This is, once more, consistent with the RPA calculations, since they indicate that the magnetic peaks become very weak, in practice invisible, at the higher energies.

V. CONCLUSIONS

We have used neutron diffraction to identify two new magnetic phases in $LiNiPO_4$, induced by the application of magnetic fields larger than 12 T along the c axis. In the process, we have clarified the magnetic phase diagram for fields up to 17.3 T along c, and, from magnetization measurements, the phase diagrams for fields up to 16 T along a and b. For fields along c, the IC modulation vector $(0, k_{\rm ic}, 0)$ was shown to stabilize at a commensurate value $(0, \frac{1}{5}, 0)$ for fields larger than 16 T below 10 K. We presented an irreducible-representation analysis of our neutron-diffraction data, which is consistent with a temperature-driven continuous phase transition from a low-temperature, elliptically polarized, canted IC spiral to a high-temperature, linearly polarized, canted IC structure. This phase transition was also resolved in our bulk magnetization data, and the transition temperatures derived from magnetization and neutron-diffraction data were found to agree within experimental error.

The MF model presented here is determined from the analysis in Ref. 11 of the spin waves observed at 2 K and zero field. The excellent account of the spin waves obtained under these conditions has here been extended so to comprise the spin waves observed at non-zero values of temperatures and fields in the uniformly ordered C-phase. In the IC-phase at low temperatures and high fields, we have observed well-defined magnetic excitations at energies below 3-4 meV, which carry substantial intensity only for wave vectors in the vicinity of the incommensurate ordering vectors. All of these observations are in firm agreement with the RPA predictions. In spite of the limited validity of the MF approach close to a second-order phase transition, the present MF model predicts a phase diagram in good agreement with our observations. Most importantly, the MF-predictions have been a valuable guidance in the determination of the magnetic structures in the different phases. In spite of its success, the MF model also shows some failures. The calculated and observed intensity ratios between different components and harmonics are found to differ in a number of cases. Some of these discrepancies might be due to the MF approximation itself, but there are systematic features indicating that the model needs to be improved, i.e. that the anisotropic modifications of the exchange interactions, appearing in the second order of the spin-orbit coupling, may be of some importance. This conclusion is substantiated by the large value of the leading-order DM interaction derived in the present analysis.

Acknowledgments

Work was supported by the Danish Agency for Science, Technology and Innovation under DANSCATT and by the Swiss NSF via contract PP002-102831. The manuscript has been authored, in whole or in part, under Contract No. DE-AC02-07CH11358 with the U.S. Department of Energy. Neutron experiments were performed at the SINQ neutron spallation source at the Paul Scherrer Institute, Switzerland, and at the Berlin Neutron Scattering Center (BENSC) at the Helmholtz Zentrum Berlin, Germany.

[1] S. W. Cheong and M. Mostovoy, Nature Materials **6**, 13 (2007).
[2] M. Fiebig, J. Phys. D: Appl. Phys. **38**, R123 (2005).
[3] W. Eerenstein, N. D. Mathur and J. F. Scott, Nature **442**, 759-765 (2006).
[4] T. Kimura, T. Goto, H. Shintani, K. Ishizaka, T. Arima

and Y. Tokura, Nature **426**, 55 (2003).
[5] G. Lawes, A. B. Harris, T. Kimura, N. Rogado, R. J. Cava, A. Aharony, O. Entin-Wohlman, T. Yildirim, M. Kenzelmann, C. Broholm and A. P. Ramirez, Phys. Rev. Lett. **95**, 087205 (2005).
[6] M. Kenzelmann, A. B. Harris, S. Jonas, C. Broholm, J. Schefer, S. B. Kim, C. L. Zhang, S.-W. Cheong, O. P. Vajk and J. W. Lynn, Phys. Rev. Lett. **95**, 087206 (2005).
[7] T. B. S. Jensen, N. B. Christensen, M. Kenzelmann, H. M. Rønnow, C. Niedermayer, N. H. Andersen, K. Lefmann, J. Schefer, M. v. Zimmermann, J. Li, J. L. Zarestky, and D. Vaknin, Phys. Rev. B **79**, 092412 (2009).
[8] M. Mercier, Ph.D. thesis, Université de Grenoble (1969).
[9] I. Kornev, M. Bichurin, J.-P. Rivera, S. Gentil, H. Schmid, A. G. M. Jansen and P. Wyder, Phys. Rev. B **62**, 12247 (2000).
[10] I. E. Chupis, Low Temp. Phys. **26**, 419 (2000).
[11] T. B. S. Jensen, N. B. Christensen, M. Kenzelmann, H. M. Rønnow, C. Niedermayer, N. H. Andersen, K. Lefmann, M. Jiménez-Ruiz, F. Demmel, J. Li, J. L. Zarestky, and D. Vaknin, Phys. Rev. B **79**, 092413 (2009).
[12] I. Abrahams and K. S. Easson, Acta. Cryst. **C49**, 925 (1993).
[13] R. P. Santoro, D. J. Segal and R. E. Newnham, J. Phys. Chem. Solids. **27**, 1192 (1966).
[14] D. Vaknin, J. L. Zarestky, J.-P. Rivera, and H. Schmid, Phys. Rev. Lett. **92**, 207201 (2004).
[15] T. B. S. Jensen, Ph.D. thesis, Risø National Laboratory (2007).
[16] The two transition temperatures $T_{\rm N}$ and $T_{\rm NC}$ were named, respectively, $T_{\rm IC}$ and T_N in some of the previous publications on $LiNiPO_4$. Here we prefer to refer to the temperature at which long-range order first appears as $T_{\rm N}$.
[17] V. M. Khrustalyov, V. N. Savitsky and N. F. Kharchenko, Czech. J. Phys. **54**, Suppl. D, 27 (2004).
[18] Rossat-Mignod, J. Methods of experimental physics (Academic Press Inc, 1987) Vol. 23, part C, chapter 19.
[19] J. Jensen and A. R. Mackintosh, *Rare Earth Magnetism: Structures and Excitations* (Clarendon Press, Oxford, 1991); http://www.nbi.ku.dk/page40667.htm
[20] M. J. M. Leask, M. R. Wells, R. C. C. Ward, S. M. Hayden, and J. Jensen, J. Phys.: Condens. Matter **6**, 505 (1994).
[21] K. A. McEwen, J. Jensen, E. D. Beirne, J. P. Allen, K. Habicht, D. T. Adroja, R. I. Bewley, and D. Fort, Phys. Rev. B **73**, 014402 (2006).
[22] J. Jensen, Phys. Rev. B **49**, 11833 (1994).
[23] Yu. N. Kharchenko, N. F. Kharcheno, M. Baran and R. Szymczak, Low Temp. Phys. **29**, 579 (2003).
[24] A. B. Strauss, M. H. Madsen, E. Brok, J. V. Pedersen, and P. Krogstrup (unpublished NBI report).